MAX-PLANCK-INSTITUT FÜR PHYSIK
WERNER-HEISENBERG-INSTITUT

MPI-PhE/94-04
January 1994

The Physics Results of the UA2 Experiment at the CERN $p\bar{p}$ Collider [*]

Karl Jakobs

Max-Planck-Institut für Physik
Föhringer Ring 6
80805 München, Germany

---

[*] to appear in International Journal of Modern Physics A

80805 München · Föhringer Ring 6

Max-Planck-Institut für Physik, München.

The Physics Results of the UA2 Experiment at the CERN $p\bar{p}$ Collider *

Karl Jakobs

Max-Planck-Institut für Physik
Föhringer Ring 6
80805 München, Germany

ABSTRACT

The UA2 experiment at the CERN $p\bar{p}$ Collider has terminated its physics programme at the end of 1990. The large data sample collected in the second experimental phase from 1988 to 1990 at $\sqrt{s} = 630$ GeV allowed for detailed tests of many aspects of the Standard Model of particle physics. Precise measurements of electroweak parameters have been performed, predictions of perturbative Quantum Chromodynamics have been tested, and a new mass range has been explored for the existence of new particles. In the present article the final results of the UA2 experiment are summarized and compared to the Standard Model predictions.

---

[*] to appear in International Journal of Modern Physics A

1. Introduction

Proton antiproton collider physics has played a major role in experimental particle physics since the startup of the CERN $p\bar{p}$ Collider programme in 1981. With the centre of mass energy of 630 GeV, access to a new energy regime was opened up allowing for the study of parton parton interactions at the energy scale of ~100 GeV. The discovery of the intermediate vector bosons W and Z in the years 1982 and 1983,[1] by the two large experiments UA1 and UA2, was an excellent confirmation of the predictions of the electroweak theory of Glashow, Salam and Weinberg.[2] Not only was the electroweak theory established, but also the other building block of the so called 'Standard Model' of particle physics, Quantum Chromodynamics (QCD),[3] was impressively confirmed. Even before the W and Z particles were discovered, jets with high transverse momentum, resulting from hard parton parton scattering, were observed with unexpected clarity.[4] Already in the early days the gross features of the events could be described by leading order QCD calculations.

In the first experimental phase from 1981 to 1985 each of the two experiments collected data corresponding to an integrated luminosity in the order of 0.9 pb^{-1}. About 250 W and 30 Z candidate events could be recorded in the electron decay channels by each experiment. Even though enough to establish the existence of the particles, they did not, however, allow for detailed tests of the theoretical predictions.

Motivated by the success of the collider, CERN undertook an important upgrade programme of the $p\bar{p}$ complex in the years 1985 to 1987, where the machine luminosity was increased by an order of magnitude. In parallel also the experiments were upgraded in order to improve the detector performance and to adapt the detectors to cope with the higher expected event rate. In the second experimental phase from 1988 to 1990, the UA2 experiment accumulated data corresponding to an integrated luminosity of 13.0 pb^{-1} in three major running periods. After nearly ten years of operation the UA2 experimental programme stopped at the end of 1990.

In the present report the main physics results of the UA2 experiment, based on these data, are presented. This includes a detailed discussion of the measurement of electroweak parameters with the focus on the measurements of the mass and the width of the W, on the study of various W decay modes, and on the direct search for the top quark. In addition, the experimental data are confronted to the theoretical predictions of perturbative Quantum Chromodynamics for a variety of hard scattering processes, including jet production, direct photon production and the production of W and Z bosons. Finally, they have also been used to explore the unknown and to look for physics beyond the Standard Model. Searches for supersymmetric particles, additional heavy vector bosons, quark compositeness and for leptoquarks are presented.

In the meantime the centre of $p\bar{p}$ collider physics has moved to the United States. Since 1987 the TEV I Collider at Fermilab is successfully running at a centre of mass energy of 1.8 TeV, and the CDF experiment has collected data in parallel to the UA2 experiment at CERN. For several years there was a fruitful competition between the CDF and the UA2 experiments, where the advantage of the Fermilab Collider of having a higher centre of mass energy was partially compensated for by the higher luminosity delivered by the CERN Collider. Today two experiments, CDF and D0, are continuing their physics programme at Fermilab with good prospects for significantly improving the existing measurements over the forthcoming years, and perhaps for discovering new phenomena. Whenever relevant, the UA2 results presented here are compared to the results obtained at the Fermilab Collider.

Before describing the large body of experimental data in Sect. 4, 5 and 6 of this report, the main features of the Standard Model are briefly recalled in Sect. 2. In particular, those predictions which can be tested in $p\bar{p}$ collisions are discussed. Experimental aspects, which are relevant for the data analysis, are briefly presented in Sect. 3.

2. Theoretical Framework

The fundamental interactions between the elementary particles are described by the Standard Model, which comprises the electroweak theory of Glashow, Salam and Weinberg and Quantum Chromodynamics. Whereas the latter describes the strong interactions between coloured quarks and gluons, the first one provides a unified description of the weak and the electromagnetic interactions. The Standard Model leads to distinct predictions, which can be tested experimentally. In the following those predictions relevant for $p\bar{p}$ physics are briefly discussed. For details the reader is referred to the extensive descriptions existing in the literature.[5]

2.1. Parameters of the Electroweak Theory

The electroweak theory is a field theory based on the gauge group $SU(2)$ of weak isospin and $U(1)$ of hypercharge, with gauge bosons W^i_μ, $i = 1,2,3$ and B_μ and gauge couplings g and g' for the two gauge groups respectively. The fundamental fermionic constituents of matter are placed in left-handed $SU(2)$ doublets,

$$\chi^i_l = \begin{pmatrix} \nu_i \\ l_i \end{pmatrix}_L \qquad \textit{and} \quad \chi^i_q = \begin{pmatrix} u_i \\ d'_i \end{pmatrix}_L , \tag{1}$$

and right-handed singlets $\Psi^i_l = (l_i)_R$ and $\Psi^i_q = (u_i)_R, (d_i)_R$, where i denotes the family generation index. The 'down-type' quarks d'_i are related via the Cabibbo-Kobayashi-Maskawa matrix[6] to the mass eigenstates d_i. The Lagrangian contains via the covariant derivative the interactions between the gauge fields and the fermions. If the gauge fields W^1_μ and W^2_μ are combined into the fields $W^\pm_\mu = \frac{1}{\sqrt{2}}\{W^1_\mu \mp iW^2_\mu\}$, terms can be identified, which describe the coupling of a lepton neutrino current to a charged vector field, corresponding to the experimentally observable weak charged currents. Since the theory is bound to contain the electromagnetic interaction, the linear combination of W^3_μ and B_μ which does couple to a $\nu - \nu$ current is associated to a field Z_μ, which is orthogonal to the photon field A_μ. For this purpose the weak mixing angle θ_W is introduced leading to the following representations for the physical bosons:

$$\begin{aligned} W_\mu^\pm &= \frac{1}{\sqrt{2}}\{W_\mu^1 \mp iW_\mu^2\} \\ Z_\mu &= \cos\theta_W\ W_\mu^3 - \sin\theta_W\ B_\mu \\ A_\mu &= \sin\theta_W\ W_\mu^3 + \cos\theta_W\ B_\mu. \end{aligned} \tag{2}$$

From the requirement that the photon couples with strength equal to the electric charge e to the left- and right-handed charged fermions, the following relations can be derived:

$$\begin{aligned} e &= g\ \sin\theta_W \quad \textit{and} \\ e &= g'\ \cos\theta_W. \end{aligned} \tag{3}$$

Using these relations, all couplings can be expressed in terms of the parameters e and $\sin\theta_W$. The Lagrangian contains three different interaction terms corresponding to the weak charged current, the weak neutral current, and the electromagnetic current.

For the generation of masses the mechanism of spontaneous symmetry breaking is used, which together with local gauge invariance leads to massive vector fields.[7] In the minimal version, a single complex scalar doublet field $\Phi(x)$, the Higgs field, is coupled to the gauge fields. The self interaction $V(\Phi) = \mu^2\Phi^\dagger\Phi + \lambda(\Phi^\dagger\Phi)^2$ is chosen in such a way that it has a non-vanishing vacuum expectation value $v = \sqrt{-\mu^2/\lambda}$. The manifold of points at which $V(\Phi)$ is minimized is invariant under $SU(2)$ transformations. By choosing a particular direction in the $SU(2)$ space, three out of the four field components of the complex field $\Phi(x)$ are removed from the physical spectrum by the Higgs mechanism and become the longitudinal modes of the $W^\pm$ and Z bosons. The fourth neutral field is related to a neutral scalar particle H and appears with a mass term $m_H = \sqrt{-2\mu^2}$ in the Lagrangian. In addition, mass terms for the vector bosons W and Z of the form

$$m_W = \frac{1}{2}vg \qquad \textit{and} \qquad m_Z = \frac{1}{2}\frac{vg}{\cos\theta_W} \tag{4}$$

appear. The relation $m_W/m_Z = \cos\theta_W$ is a prediction of the Standard Model. At tree level in perturbation theory this relation is also true if the Higgs sector is built up of more than one Higgs doublet. In this case, two more charged and two more neutral Higgs scalar particles appear for each additional doublet. In addition, Yukawa couplings to fermions are introduced to generate mass terms of the form $m_{f_i} = c_{f_i}\frac{v}{2}$ with parameters c_{f_i} for each charged fermion f_i.

Given the relations defined above, the fundamental parameters introduced in the theory, $g,\ g', \lambda,\ \mu,\ \textit{and}\ c_{f_i}$, can be replaced by the parameters

$$e,\ m_W,\ m_Z,\ m_H,\ \textit{and}\ m_{f_i},$$

which can be directly measured in suitable experiments.

2.2. *Properties of the W and Z Bosons*

2.2.1. *The Boson Masses*

From the requirement of consistency of the electroweak theory at energies well below the W mass with the Fermi theory of weak interactions[8] a prediction for the W mass can be deduced:

$$m_W^2 = \frac{A^2}{\sin^2\theta_W}. \tag{5}$$

The parameter A is related to the fine structure constant α and to the Fermi constant G_F by the relation $A = \sqrt{\frac{\pi\alpha}{\sqrt{2}G_F}}$. From the measured values of α and G_F it can be computed to be A = 37.2810 ± 0.0003 GeV.[9] This tree level prediction for the mass is modified by higher order corrections in the renormalizable electroweak theory. Choosing a renormalization scheme such that $\sin^2\theta_W$ is defined to all orders by the relation[10]

$$\sin^2\theta_W = 1 - \frac{m_W^2}{m_Z^2}, \tag{6}$$

the Standard Model predictions for the boson masses take the form

$$\begin{aligned} m_W^2 &= \frac{A^2}{\sin^2\theta_W(1-\Delta r)}, \\ m_Z^2 &= \frac{A^2}{\sin^2\theta_W\cos^2\theta_W(1-\Delta r)}. \end{aligned} \tag{7}$$

The variable Δr represents the radiative corrections to $\mathcal{O}(\alpha)$ arising from loops in the gauge boson propagators. They include contributions from Higgs, gauge boson, and fermion loops. The value of Δr is found to depend logarithmically on the Higgs mass ($\sim \ln(\frac{m_H}{m_Z})^2$) and quadratically on the top quark mass ($\sim \frac{m_t^2}{m_W^2}$). Such a strong dependence is typical whenever there is a fermion doublet with a large mass splitting between the two members.[11]

The dependence of Δr on the unkown top quark mass m_t is shown in Fig. 1. It should be noted that also higher order electroweak terms, $\mathcal{O}(\alpha^2)$, and additional QCD corrections, related to large top quark masses, have been calculated.[12] Both electroweak and QCD higher order effects give a small positive shift to Δr and thus diminish slightly the slope of the first order dependence (see Fig. 1).

2.2.2. *The Boson Decays*

By construction of the electroweak Lagrangian, the W and Z bosons decay into fermion pairs. The partial widths for decays into massless fermion antifermion pairs, including first order strong and electroweak radiative corrections are given by:[5]

$$\begin{aligned} \Gamma_{W\to f\bar{f}'} &= F_{QCD}\,\frac{G_F\,m_W^3}{6\pi\,\sqrt{2}}\,\left|V_{f\bar{f}'}\right|^2\,(1+\delta_f^W), \\ \Gamma_{Z\to f\bar{f}} &= F_{QCD}\,\frac{G_F\,m_Z^3}{24\pi\,\sqrt{2}}\,\left[1+(1-4\,|Q_f|\sin^2\theta_W)^2\right]\,(1+\delta_f^Z). \end{aligned} \tag{8}$$

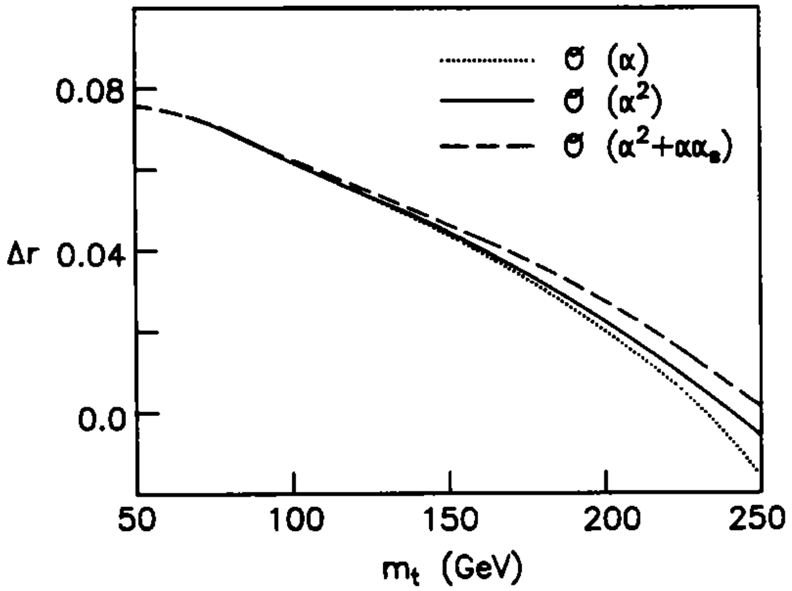

Figure 1. *Radiative corrections* Δr *as a function of the top quark mass* m_t.

The factor F_{QCD} is a colour factor which includes QCD corrections. It takes the values $F_{QCD} = 1.0$ for lepton pairs and $F_{QCD} = 3\ (1 + \alpha_s/\pi + ...)$ for quark pairs, with α_s being the strong coupling constant. In the case of W decays into quarks the factor $|V_{q\bar{q}'}|^2$ is the relevant Cabibbo-Kobayashi-Maskawa matrix[6] element. For leptonic decays it takes the value 1. The terms δ_f^W and δ_f^Z represent the electroweak radiative corrections, which have been calculated and are found to be small.[13,14] Neglecting these corrections, one obtains for the electronic partial widths:

$$\begin{aligned}\Gamma_{W\rightarrow e\nu} &= 225.7\ \left(\frac{M_W}{80.2\ GeV}\right)^3 \quad MeV, \\ \Gamma_{Z\rightarrow ee} &= 83.5\ \left(\frac{M_Z}{91.18\ GeV}\right)^3 \quad MeV. \qquad (9)\end{aligned}$$

Despite the existing lower bounds on the top quark mass, derived in hadron collider experiments assuming the Standard Model value for the semileptonic branching ratio $t \longrightarrow be\nu$, $W \longrightarrow t\bar{b}$ decays could still be allowed, if for example top decays via a charged Higgs boson H^+ exist (see Sect. 6.2. and Ref.[15]). In this case, quark mass corrections cannot be neglected and an additional phase space factor $S_{q\bar{q}'} < 1$ needs to be taken into account.[16] Also the QCD corrections of order α_s are modified with respect to the massless case.[17]

The total widths Γ_W and Γ_Z are given by the sum of the rates for the individual final states. Due to the mass dependent phase space and correction factors, the total widths also depend on the top quark mass. In the case of the W, the width varies between

$$\begin{aligned} \Gamma_W &= 2.49\, GeV \qquad for \quad m_t = 45 \;\; GeV \quad and \\ \Gamma_W &= 2.08\, GeV \qquad for \quad m_t > m_W - m_b. \end{aligned} \tag{10}$$

Since any additional decay channels, beyond the ones considered in the Standard Model, will lead to an increase of the decay width, a precise measurement of Γ_W gives information on the presence of new physics in the mass range of the vector bosons.

From the formulae given above, branching ratios $B_{W \to e\nu} = \Gamma_{W \to e\nu}/\Gamma_W$ and $B_{Z \to ee} = \Gamma_{Z \to ee}/\Gamma_Z$ for the electronic decay modes of 10.8% and 3.4%, respectively, can be deduced in the case of $m_t > m_W - m_b$. About 70% of the vectors bosons are expected to decay into $q\bar{q}$ pairs.

2.3. Quantum Chromodynamics

Quantum Chromodynamics is the quantum field theory of the strong interaction based on the gauge group $SU(3)$.[3] The fundamental constituents, the quarks, appear in $SU(3)$ triplets, according to the three components of colour. The interaction is mediated by eight gauge bosons G^a_μ, $(a = 1, 2, ..., 8)$, the gluons. In the Lagrangian only one basic coupling, the gauge coupling g_s appears, which describes the flavour independent coupling of quarks to gluons.

The calculation of physical quantities in perturbation theory up to any fixed order requires renormalization in order to remove ultraviolet divergences. A renormalization scale μ has to be introduced, at which the subtractions of the divergences are performed. In general, the scale dependence is absorbed in a 'renormalized coupling' $\alpha_s(\mu) = g_s^2(\mu)/4\pi$. If the perturbative calculation of any physical quantity is performed up to a given fixed order, the result will depend on the choice made for the parameter μ. This dependence disappears only if all orders are included in the perturbative calculation. Mathematically, this is expressed in the so called renormalization group equation, from which the functional dependence of α_s on μ can be deduced. To leading order of perturbation theory the relation

$$\alpha_s(\mu) = \frac{\alpha_s(\mu_0)}{1 \; + \; b \; \alpha_s(\mu_0) \ln \left(\frac{\mu}{\mu_0}\right)^2}, \qquad with \qquad b = \frac{33 - 2n_f}{12\pi} \tag{11}$$

is obtained, where b is the first coefficient of the QCD β-function,[3] n_f is the number of quarks with mass less than the energy scale μ and $\alpha_s(\mu_0)$ is introduced as an integration constant. Thus perturbative QCD only makes predictions about the variations of the coupling constant with the scale μ but does not predict its absolute value. The latter has to be obtained from experiments. It is more conventional to introduce a dimensional parameter Λ instead of $\alpha_s(\mu_0)$ via the relation $\ln\left(\frac{\mu_0}{\Lambda}\right) = 1/b \; \alpha_s(\mu_0)$, so that Eq. (11) is transformed into

$$\alpha_s(\mu) = \frac{12\pi}{(33 - 2n_f) \ln \left(\frac{\mu}{\Lambda}\right)^2}. \tag{12}$$

For $\mu \to \infty$ the value of the coupling α_s goes to zero. This behaviour, called 'asymptotic freedom', allows strong interaction processes at high energies to be calculated in perturbation theory.

The definition of Λ can also be extended to next to leading order in perturbation theory. In this case $\alpha_s(\mu)$ is extracted by taking into account two loop corrections in the propagator. One way to define α_s at second order is:[9]

$$\alpha_s(\mu) = \frac{12\pi}{(33 - 2n_f)\ln\left(\frac{\mu}{\Lambda}\right)} \cdot \left[1 - \frac{6(153 - 19n_f)}{(33 - 2n_f)^2} \frac{\ln\left(\ln(\mu^2/\Lambda^2)\right)}{\ln(\mu^2/\Lambda^2)}\right] . \tag{13}$$

Since the number n_f is changing when flavour thresholds are crossed, Λ must also change discretely through flavour thresholds so that $\alpha_s(\mu)$ is a continuous function. Furthermore, the renormalization procedure is not unique and different schemes can be defined.[18] Thus, for the definition of Λ the specification of the renormalization scheme and of the number of active quark flavours is needed.

2.4. QCD Predictions for $p\bar{p}$ Collisions

The high energy interactions of hadrons are described by the QCD improved parton model. The hard scattering process between two hadrons is the result of the interaction between the quarks and gluons which are the constituents of the incoming hadrons. These hadrons provide broad band beams of partons which possess varying fractions x_i of the momenta of their parent hadrons. The cross section for a hard scattering process initiated by two hadrons can be written as

$$\sigma = \sum_{i,j} \int dx_1 dx_2 \; f_i(x_1, \mu) \; f_j(x_2, \mu) \; \hat{\sigma}_{ij}(x_1, x_2, \alpha_s(\mu)). \tag{14}$$

The functions $f_i(x, \mu)$ are the quark and gluon distributions, defined at the scale μ. The short distance cross section for the scattering of partons of type i and j is denoted by $\hat{\sigma}_{ij}$. Since the coupling is small at high energy, this cross section can be calculated as a perturbative series in the running coupling α_s. The n-th order approximation is given by

$$\hat{\sigma} = c_0 \; \alpha_s^k \; [(1 + \sum_{j=1}^{n} c_j \alpha_s^j], \tag{15}$$

with coefficients c_j. In the leading order approximation (n=0), the short distance cross section is identical to the parton scattering cross section of the naive quark parton model. As discussed above, the scale μ is an arbitrary parameter, which in general is however chosen to be of the order of the energy characterizing the parton parton interaction, like, for example, the mass of the vector bosons or the transverse momenta of outgoing jets. The more orders are included in the perturbative expansion, the weaker the dependence on μ.

Those partons which do not take part in the hard scattering process will produce what is generally called the 'underlying event'. Finally, it should be stressed that

Eq. (14) does not describe the bulk of the events which occur at a hadron collider. It can only be used to describe the most interesting classes of events which involve a hard interaction. Most events result from elastic and soft inelastic interactions generally called 'minimum bias' events. In the following a few specific examples of hard scattering processes are discussed.

2.4.1. Jet Production

Two-jet events result when an incoming parton from one hadron scatters off an incoming parton from the other hadron to produce two high transverse monentum partons which are observed as jets. All parton processes which contribute in lowest order to the cross section are shown in Fig. 2. Expressions for the leading order matrix elements are known and are given in Table 1 for the various subprocesses[19] as a function of the Mandelstam variables s, t and u under the assumption of massless partons. In order to illustrate the relative importance of the subprocesses, also the numerical values of $|M^2|$ at $\Theta^* = 90°$ are shown, where Θ^* is the scattering angle in the two-jet centre of mass system. Terms involving gluons in the initial state are dominant, whenever the gluon density in the incident hadrons is comparable to that of the quarks.

Table 1. Matrix elements for parton scattering

subprocess	$\|M\|^2$	$\theta^* = \pi/2$
$qq' \to qq'$	$\frac{4}{9}\frac{s^2+u^2}{t^2}$	2.22
$qq \to qq$	$\frac{4}{9}\left(\frac{s^2+u^2}{t^2} + \frac{s^2+t^2}{u^2}\right) - \frac{8}{27}\frac{s^2}{ut}$	3.26
$q\bar{q} \to q'\bar{q}'$	$\frac{4}{9}\frac{t^2+u^2}{s^2}$	0.22
$q\bar{q} \to q\bar{q}$	$\frac{4}{9}\left(\frac{s^2+u^2}{t^2} + \frac{t^2+u^2}{s^2}\right) - \frac{8}{27}\frac{u^2}{st}$	2.59
$q\bar{q} \to gg$	$\frac{32}{27}\frac{u^2+t^2}{ut} - \frac{8}{3}\frac{u^2+t^2}{s^2}$	1.04
$gg \to q\bar{q}$	$\frac{1}{6}\frac{u^2+t^2}{ut} - \frac{3}{8}\frac{u^2+t^2}{s^2}$	0.15
$qg \to qg$	$-\frac{4}{9}\frac{u^2+s^2}{us} + \frac{u^2+s^2}{t^2}$	6.11
$gg \to gg$	$\frac{9}{2}\left(3 - \frac{ut}{s^2} - \frac{us}{t^2} - \frac{st}{u^2}\right)$	30.38

Recently the evaluation of the full next to leading order matrix elements has been completed.[20] Unlike in lowest order, where a direct correspondence between a jet cross section and the parton cross section can be made, a prescription is needed to derive jet cross sections in next to leading order. When such prescriptions are applied, the next to leading order cross sections show substantially smaller sensitivities to variations of the renormalization scale than at lowest order.[21]

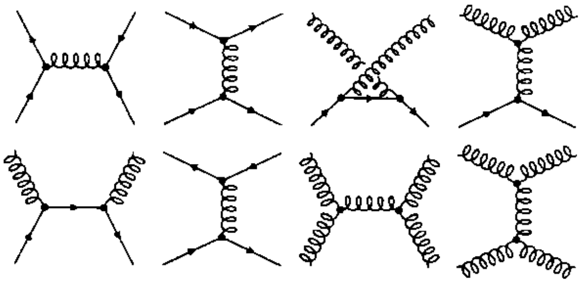

Figure 2. *First order diagrams for hard parton scattering.*

2.4.2. W and Z Production

To leading order the production of the intermediate vector bosons W and Z is described by the Drell-Yan mechanism,[22] where a quark from the first incoming hadron annihilates with an antiquark from the second hadron. The Born level subprocess cross sections are given by

$$\begin{aligned} \hat{\sigma}_{q\bar{q}'\to W} &= \frac{\pi}{3}\sqrt{2}G_F M_W^2\,|V_{qq'}|^2\,\delta(\hat{s}-M_W^2) \qquad \textit{and} \\ \hat{\sigma}_{q\bar{q}\to Z} &= \frac{\pi}{3}\sqrt{2}G_F M_Z^2(v_q^2+a_q^2)\,\delta(\hat{s}-M_Z^2), \qquad (16) \end{aligned}$$

where $V_{qq'}$ is the relevant Cabibbo-Kobayashi-Maskawa matrix element and v_q and a_q denote the vector and axial-vector coupling strengths. The $\mathcal{O}(\alpha_s)$ (see Fig. 3 for the relevant diagrams) and $\mathcal{O}(\alpha_s^2)$ corrections to the W and Z cross sections have recently been calculated in the $\overline{MS}$ renormalization scheme.[23] The results of the calculations, which have been obtained using the structure function parametrization of Ref.[24] with $\alpha_s(M_W) = 0.117$, are summarized in Table 2. The $\mathcal{O}(\alpha_s)$ corrections lead to an increase of ~27% and the $\mathcal{O}(\alpha_s^2)$ corrections give an additional increase of the cross section by ~7%. These corrections are often parametrized in terms of total K-factors, defined at each perturbative order [i] as the ratio of the cross section computed to that order normalized to the Born level cross section:

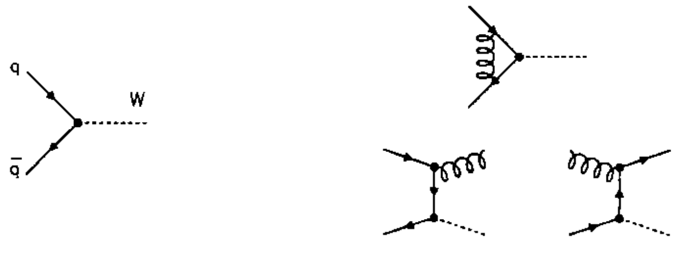

(a) (b)

Figure 3. *(a) Born level and (b) $\mathcal{O}(\alpha_s)$ diagrams for W production.*

Table 2. Total cross sections for W and Z production at $\sqrt{s} = 630$ GeV (from Ref.[23]).

	σ_W (nb)	σ_Z (nb)
Born level	5.03	1.54
$\mathcal{O}(\alpha_s)$	6.41	1.96
$\mathcal{O}(\alpha_s^2)$	6.72	2.06

$$K_{tot}^{[i]} = \frac{\sigma^{[i]}}{\sigma^{[0]}}.$$

The largest uncertainties in these cross section calculations arise from uncertainties in the structure functions. Using different parametrizations, they have been estimated to be in the order of ±10%.[23]

The dependence of the cross sections on the renormalization scale μ is shown in Fig. 4. These results demonstrate that the dependence of the cross section on the renormalization scale μ is reduced as higher order terms are included in the calculation.

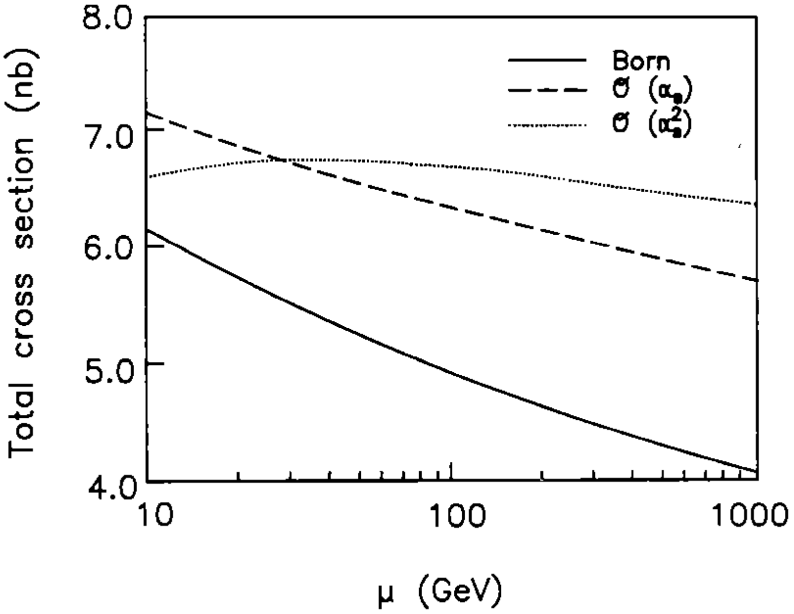

Figure 4. *Renormalization scale dependence of the total W cross section (from Ref.*[23]*).*

2.4.3. Transverse Momentum of the W and Z Bosons

As a consequence of the small intrinsic transverse momenta of the initial state partons in the hadrons, most of the vector bosons (V=W,Z) are produced with relatively small transverse momenta. However, higher order QCD processes can lead to the production of bosons with large transverse momenta, with the leading order contributions resulting from the processes $q\overline{q} \rightarrow Vg$ and $qg \rightarrow Vq$ (see Fig. 3b). For large transverse momenta ($P_T^V \gtrsim 20\text{GeV}$) the cross section $d\sigma/dP_T$ can be computed using perturbative QCD. The calculations have been performed including the complete $\mathcal{O}(\alpha_s^2)$ contributions.[25,26] At small transverse momenta the perturbative calculations diverge due to infrared singularities. As the transverse momentum becomes smaller, the emission of multiple soft gluons becomes important. The generic expression for the cross section is

$$\frac{1}{\sigma}\frac{d\sigma}{dP_T^2} = c_1 \frac{\alpha_s(P_T^2)}{P_T^2} \ln(\frac{M_V^2}{P_T^2}) + c_2 \frac{\alpha_S^2(P_T^2)}{P_T^2} \ln^3(\frac{M_V^2}{P_T^2}) + ..., \qquad (17)$$

with coefficients c_i in the order of 1 (Ref.[27]). The higher order terms become important when $\alpha_s(P_T^2)\ln^2(\frac{M_V^2}{P_T^2}) \sim 1$ which corresponds to P_T values below ~10 GeV. The large logarithms can be resummed to all orders in perturbation theory, leading to QCD predictions of order α_s (Ref.[28]) and order α_s^2 (Ref.[29]). Details about the resummation techniques and a discussion of the remaining theoretical uncertainties can be found in the literature.[30]

3. Experimental Aspects

3.1. The UA2 Detector

After five years of successful operation during 1981 to 1985, the CERN proton antiproton complex was substantially upgraded.[31] A new separate antiproton collector (ACOL) was added to the existing antiproton accumulator and modifications to the Super-Proton-Synchroton (SPS) were made to allow for a six-bunch operation. This enabled the $p\bar{p}$ Collider to run at a luminosity of about $3 - 4 \cdot 10^{30} cm^{-2} sec^{-1}$, an increase by a factor of 10 compared to the previous performance. In order to exploit the physics potential offered by the collider, the UA2 detector[32] was also upgraded during the period 1985 to 1987. The detection capabilities were improved in two aspects:

- the calorimeter coverage was extended to small angles to improve the measurement of missing transverse momentum by the addition of new endcap calorimeters to the existing central calorimeter;
- the central detector was completely rebuilt in order to improve the electron identification, especially at low transverse momenta.

In addition, a completely new three-level trigger and data acquisition system was developed[33] in order to cope with the expected high data rate. The UA2 detector did place emphasis on the detection and measurement of electrons, photons, jets and missing transverse momentum, whereas no muon detection system was available. As in the earlier phase, particle detection was achieved without using magnetic fields. Charged particle tracking was performed in the central detector covering the pseudorapidity range $|\eta| < 1.6$. Energy measurements were performed in the calorimeters covering the range $|\eta| < 3.0$.

A longitudinal view of a quadrant of the upgraded UA2 detector is shown in Fig. 5. In the following the main features of the detector are briefly summarized. Details of the construction and performance of the various detector elements can be found in Ref.[33] and in the references given below.

3.1.1. Calorimetry

The central calorimeter[34] of the original UA2 detector was retained with minor modifications. It covers the full azimuthal range, $0° < \phi < 360°$, and polar angles $40° < \Theta < 140°$. Each of the 240 electromagnetic and hadronic cells subtends $10°$ in Θ and $15°$ in ϕ. The electromagnetic part is a multi-layer sandwich of lead and scintillator, 17 radiation lengths thick, while the hadronic part, consisting of two compartments, is an iron-scintillator sandwich, with a thickness of 4.5 absorption lengths, including the electromagnetic compartment. In order to increase the radial space available for the new central detector, the thickness of the edge cell electromagnetic compartments was reduced. These edge cells cover the polar angles $40° < \Theta < 50°$ and $130° < \Theta < 140°$.

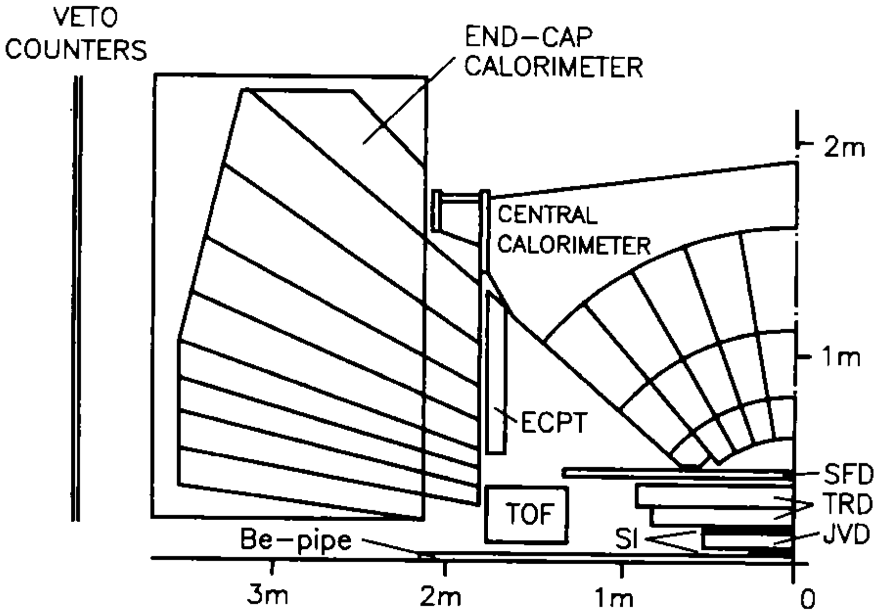

Figure 5. *Schematic longitudinal view of the UA2 detector showing one quadrant.*

The forward calorimeters (end caps) cover the pseudorapidity region $1 < |\eta| < 3$. Each end cap consists of 12 modules and each module is segmented into 16 cells. In a given module the two cells closest to the beam axis ($2.5 \leq |\eta| \leq 3.0$ and $2.2 \leq |\eta| \leq 2.5$) cover 30° in azimuth. The other cells have a constant segmentation of $\Delta\phi = 15°$, $\Delta\eta = 0.2$. All the cells in the pseudorapidity interval $1.0 \leq |\eta| \leq 2.5$ have one electromagnetic and one hadronic compartment. The electromagnetic compartment is a multi-layer sandwich of lead and scintillator, with a total thickness varying from 17.1 to 24.4 radiation lengths, depending on the polar angle. The hadronic compartment is a multi-layer sandwich of iron and scintillator corresponding to ~ 6.5 absorption lengths, including the electromagnetic compartment. Each compartment is read out via two wavelength shifting plates placed on opposite sides of each cell, introducing a dead space between adjacent cells of 7 mm for the electromagnetic compartments and of 13 mm for the hadronic ones. To minimise the effect of these dead spaces each module is rotated by 50 mrad around its symmetry axis normal to the beam.

3.1.2. Central Detector

The layout of the central detector is included in Fig. 5. It consists of:

- two layers of silicon pad detectors,[35] one located outside the beryllium beam pipe at a radius of 3.5 cm, the second one at a radius of 14.5 cm. These counters are used for tracking and ionization measurements;

- a cylindrical drift chamber with jet geometry (Jet Vertex Detector),[36] located between the two silicon layers. Its purpose is to confirm with a good resolution in ϕ the presence of a track close to the interaction point;

- a transition radiation detector[37] consisting of two sets of radiators and proportional chambers, filled with a $Xe-CH_4$ mixture. Its purpose is to provide additional power in the electron identification;

- a scintillating fibre detector,[38] which consists of approximately 60000 fibres arranged on 24 cylindrical layers, forming 8 stereo triplets. The first six, used for tracking, are followed by a 1.5 radiation lengths thick lead converter and by two additional triplets, which are used to localise the early development of electromagnetic showers initiated in the lead converter ('preshower detector').

The central detector is complemented in the end cap regions by a system of proportional tubes,[39] which provides both tracking and preshower information. A time of flight system,[40] covering the range $2.7 < |\eta| < 4.5$, provides a trigger signal for inelastic $p\bar{p}$ collisions and information on the position of the event vertex along the beam line.

3.2. Detector Calibration

For a precise measurement of the masses of the intermediate vector bosons a precise knowledge of the absolute energy scale of the calorimeters is essential. In a non-magnetic detector such as UA2, this scale can only be derived from test beam calibrations. The calorimeter response has thus been extensively studied in test beams of electrons, pions, and muons during the period of 1986 to 1990. Approximately $25 \cdot 10^6$ events have been collected during these measurements. Initially, between 1986 and 1987, all cells of the calorimeters were exposed to test beams to provide the absolute calibration. The energy scale has then been tracked using periodic ^{60}Co source and light pulser calibrations. Each year a portion of the calorimeter has been recalibrated in the test beam to verify this procedure, leading to an estimated uncertainty of ±1% on the absolute energy scale of the electromagnetic calorimeter and of ±2% on the scale of the hadronic calorimeter.[41]

Careful studies were performed on a small number of representative cells in order to parametrize the energy response to electrons as a function of the incident particle direction and impact point. The observed variations, on the order of ±10%, have been accurately modeled by a parametrization of the test beam data.

3.3. Particle Identification

In this section the identification of electrons, neutrinos and jets in the UA2 detector is briefly described. They will provide the basic signatures for all physics processes considered later.

3.3.1. Cluster Reconstruction in the Calorimeters

The starting point for the reconstruction of electrons and jets are clusters of deposited energy in the calorimeters. At the trigger level and in the subsequent analysis, clusters are formed by joining all cells with an energy greater than 400 MeV sharing a common side. Clusters with a small lateral size and a small energy leakage into the hadronic compartment, consistent with that from a single isolated electron as measured in test beams, are marked as electromagnetic clusters and are subsequently examined as potential electron candidates.

Due to the non-compensation of the calorimeter, the response to hadronic showers depends on the energy fraction carried by photons. An average correction factor, determined from pion test beam data, is defined for each compartment. These weight factors are used to multiply the observed energies in the hadronic showers in order to compensate for the difference from electron showers. The weights applied to the electromagnetic cells are 1.18 in the central calorimeter and 1.20 in the end-caps. In addition, a factor of 1.06 is applied to the second hadronic compartment in the central calorimeter to account for energy leaking through the back of the calorimeter.

3.3.2. Electron Identification

For the identification of electrons, the calorimeter cluster information is combined with the information from the tracking and preshower detectors. To this purpose the detector can be divided into three regions: central (non-edge) ($|\eta| < 0.8$), central (edge) ($0.8 < |\eta| < 1.0$), and forward ($1.0 < |\eta| < 1.6$).

The various steps applied for the electron identification are described briefly in the following. The efficiencies for each cut are listed in Table 3. Details, along with the methods for evaluating these efficiencies, are given in Ref.[42].

An electron candidate must fulfill the following requirements:

- an electromagnetic cluster must exist with a transverse energy E_T exceeding a given threshold;
- a track must be reconstructed in the tracking detectors, originating from a reconstructed vertex and pointing to the electromagnetic calorimeter cluster;
- a preshower cluster must exist with a charge well above that deposited by a minimum ionizing particle, which can be associated to the reconstructed track within the detector resolution;
- the lateral and longitudinal profiles of the electromagnetic shower in the calorimeter are required to be consistent with those expected for a single isolated electron incident along the track direction, as determined from extensive test beam measurements.

The detected energy is summed over a small number of calorimeter cells, typically two or three, which are determined according to the measured electron direction and impact point. Direction and impact point dependent energy corrections (see Sect. 3.2.) are then applied to determine the electron energy.

Table 3. Efficiencies for the standard UA2 electron selection in the various detector regions

	Central region		Forward region
	non-edge	edge	
Calorimeter (cluster level)	$91.7 \pm 0.7\%$	$91.8 \pm 1.6\%$	$95.9 \pm 0.8\%$
Shower profile (χ^2)	$93.8 \pm 0.8\%$	$91.6 \pm 2.3\%$	$94.6 \pm 1.5\%$
Track-Preshower	$77.2 \pm 1.7\%$	$77.2 \pm 1.7\%$	$94.7 \pm 1.8\%$
Total	$66.4 \pm 2.0\%$	$64.9 \pm 3.3\%$	$85.9 \pm 1.7\%$

3.3.3. Neutrino Identification

The presence of neutrinos can be deduced by measuring the transverse momentum imbalance in the event. The missing transverse momentum, $\not{p}_T$, is attributed to an undetected neutrino. Experimentally it can be approximated by summing the deposited transverse energies in all calorimeter cells

$$\vec{\not{p}}_T = -\sum_i E_T^i \vec{n}_i , \tag{18}$$

where $\vec{n}_i$ is the unit vector in the transverse plane pointing from the event vertex to the centre of the cell i with transverse energy E_T^i.

The quality of the $\not{p}_T$ measurement has been studied using minimum bias and two-jet events, in which high energy neutrino emission is not expected. Experimentally it has been found that the $\not{p}_T$ distribution can be described by

$$\frac{d\,n}{d\not{p}_T{}^2} \sim \frac{1}{\Delta^2}\, e^{-(\not{p}_T/\Delta)^2} . \tag{19}$$

The resolution parameter Δ has been found to depend on the total deposited transverse energy $\sum E_T$ in the event:[43]

$$\Delta = 0.8 \left(\sum E_T\right)^{0.4} . \tag{20}$$

Examples of the $\not{p}_T{}^2$ distributions for two representative $\sum E_T$ intervals are shown in Fig. 6. Due to the good hermeticity of the UA2 calorimeter, there is no evidence for non-Gaussian tails, thus allowing for a straightforward and unambiguous neutrino identification by requiring $\not{p}_T \gtrsim 4\Delta$.

3.3.4. Jet Reconstruction

Due to the fragmentation of partons into the experimentally observable hadrons, jet reconstruction is not unique and requires a prescription for which hadrons to include. The reconstruction is even more ambiguous since processes like final state gluon radiation or the fragmentation of the spectator partons ('underlying event')

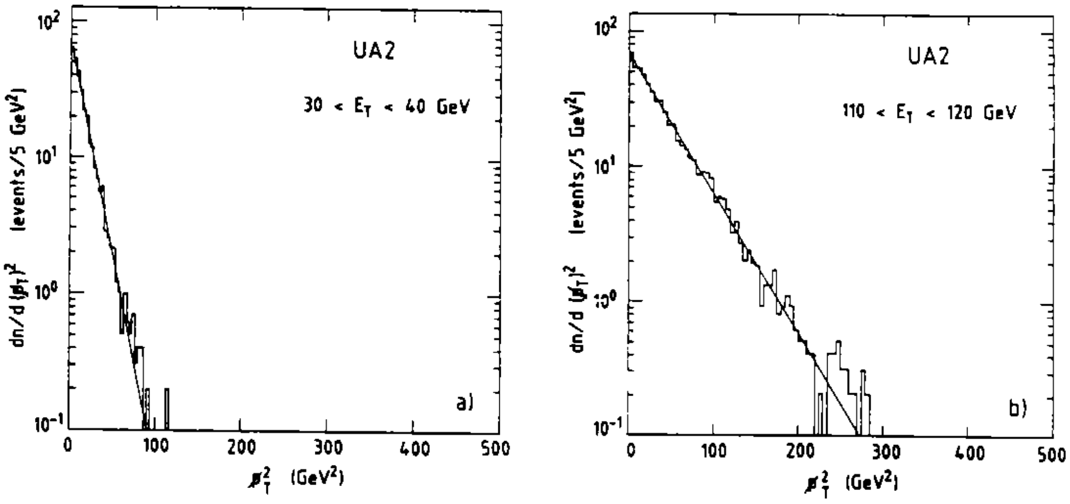

Figure 6. *The distributions of* $\not{p}_T{}^2$ *for two representative* $\sum E_T$ *intervals.*

are present in the same event. The studies over the past years have shown that there is no unique prescription to define jets. Jet algorithms must be adapted to the specific physics processes under study.

There are basically two different algorithms which have been used in the UA2 experiment, the cluster and the cone algorithm.

Cluster algorithm: Jets are identified with the reconstructed energy clusters defined in Sect. 3.3.1. The jet energy is assumed to be the cluster energy and its direction is defined by the event vertex and the energy weighted cluster centre. Usually only clusters whose transverse energy exceeds a given threshold are retained. The basic advantage of this jet algorithm is the good angular separation between neighbouring jets. However, the energy threshold of 400 MeV on the cell energies implies that a significant fraction of the parton energy is not included in the reconstructed jet energy. Instead, only the energy in the core of the jet is accounted for.

Cone algorithm: The reconstructed calorimeter clusters are considered to represent the core of the jet, with the jet axis as defined above. The jet energy is then computed as the sum of the energies of all calorimeter cells whose centres are contained in a cone around this axis. All cells satisfying the condition $\sqrt{\Delta\phi^2 + \Delta\eta^2} < R_{cone}$, where $\Delta\phi$ (in rad) is the azimuthal and $\Delta\eta$ is the pseudorapidity separation between the centre of the calorimeter cell and the jet axis, are included in the energy sum. Values for R_{cone} are typically chosen to be in the range from 0.5 to 1.0. There exist basically two variants of this algorithm. If the cones of two original clusters overlap, the smaller cluster can either be merged together with the larger one with the jet axis redefined or the energy in the overlap region can be shared in the ratio of the original cluster energies.

3.4. The Selection of W and Z Events

Since the W and Z events play a major role in many of the physics analyses described later, their selection is briefly described here. The events are selected from the total data sample collected by the UA2 experiment in the years between 1988 and 1990 corresponding to an integrated luminosity of $13.0 \pm 0.7\ pb^{-1}$.

In order to select a clean sample of $W \rightarrow e\nu$ decays, the events are required to contain an electron passing the standard identification criteria in addition to the following kinematical cuts:

$$\begin{aligned} P_T^e &> 20\ GeV, \qquad\qquad P_T^\nu > 20\ GeV \quad and \\ m_T &> 40\ GeV, \end{aligned}$$

where P_T^e and P_T^ν are the transverse momenta of the electron and the neutrino and m_T is the transverse mass of the electron neutrino system, defined as

$$m_T = \sqrt{2P_T^e P_T^\nu(1 - \cos\Delta\varphi)}, \tag{21}$$

where $\Delta\varphi$ is the azimuthal separation between the measured electron and neutrino directions. These selection criteria are passed by 3559 events, of which 2887 have the electron in the central calorimeter. The transverse mass spectra are shown in Fig. 7 for both the central (solid line) and forward (dashed line) electron samples. As expected from kinematics, the distribution for electrons in the central calorimeter shows a prominent 'Jacobian peak', while electrons in the acceptance region of the forward calorimeters produce a flatter distribution. These samples are expected to contain a contribution of $3.8 \pm 0.1\%$ ($3.3 \pm 0.3\%$) of events resulting from the process $W \rightarrow \tau\nu$ followed by the decay $\tau \rightarrow e\nu\bar{\nu}$ in the central (forward) region. In addition, a small contribution of $0.5 \pm 0.2\%$ of the events is expected to result from misidentified jets from QCD jet production.[44]

For the selection of $Z \rightarrow ee$ events, one of the two electrons is required to pass the standard electron cuts and to have a transverse momentum exceeding 20 GeV. The second one may pass looser cuts on the track-preshower matching[44] and must have a transverse momentum exceeding 15 GeV. The distribution of the invariant mass of the electron pairs (m_{ee}) selected in this way is shown in Fig. 8. In the Z signal region, defined as $76 < m_{ee} < 110$ GeV, 269 events are found, with an expected background from QCD jet production of 3.4 ± 0.3 events.[44] The events outside the signal region can be explained as a superposition of electron pairs from Drell-Yan production via a virtual photon[45] and of background from QCD jet production. One event is observed with an electron pair mass of 278 GeV.

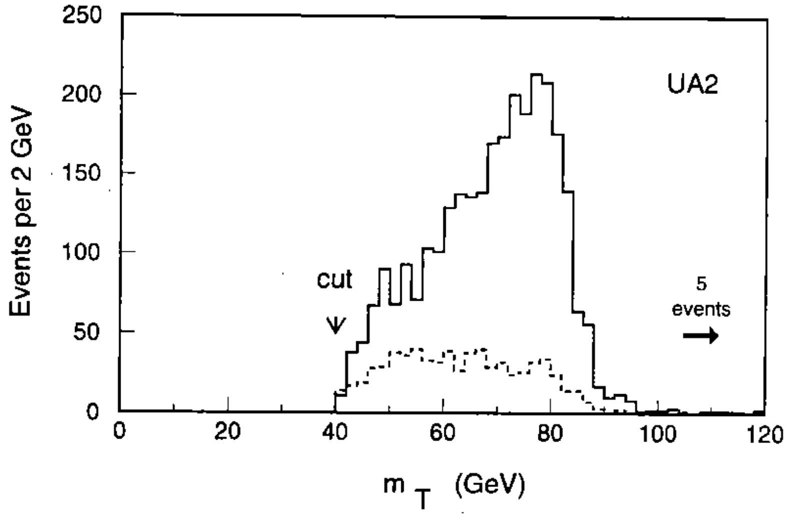

Figure 7. *The transverse mass (m_T) spectra for W candidates in the central (solid line) and forward (dashed line) acceptance regions.*

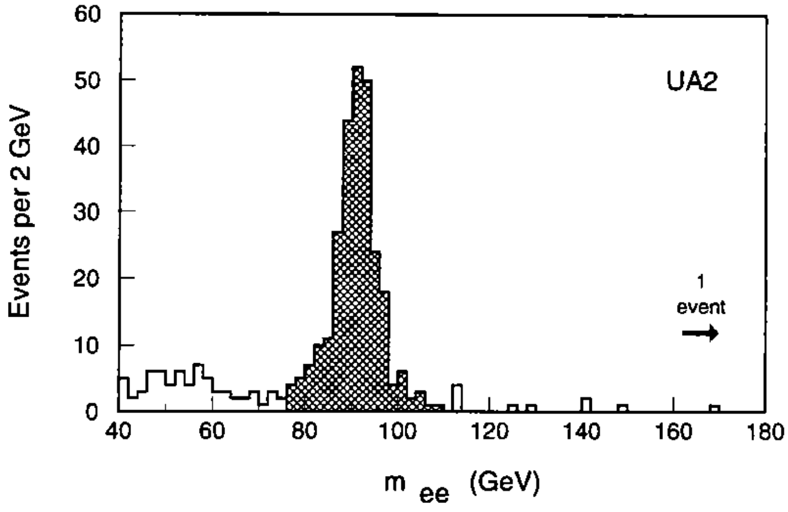

Figure 8. *The invariant mass spectrum of the electron pairs passing final identification cuts. The range of m_{ee} used to select the final Z candidates is indicated by the shaded region.*

4. Measurement of Electroweak Parameters

4.1. The Measurement of the W Mass

The masses of the intermediate vector bosons, m_W and m_Z, are the two fundamental parameters of the Standard Model of electroweak interactions which are directly measurable at the $p\bar{p}$ collider.

Due to the successful operation of the e^+e^- colliders LEP and SLC during the past few years, it has become possible to measure the parameters of the Z boson, in particular the Z mass, with an extremely high precision. However, for the direct measurement of the W mass, it is still necessary to rely on hadron colliders. Unlike in e^+e^- colliders, where the beam energy provides a precise calibration of the mass scale, in hadron colliders the W and Z decay products must be used to reconstruct the boson masses. Since many systematic uncertainties, including the energy scale uncertainty, cancel when the ratio of the W and Z masses is determined, the method followed by the UA2 experiment has been to measure the mass ratio m_W/m_Z as precisely as possible. When this ratio is combined with the measurement of the Z mass from e^+e^- colliders, a precise measurement of the W mass is obtained.

4.1.1. Event Samples

Since for a precise mass determination a high quality electron energy measurement is required, only those events from the W and Z samples defined in Sect. 3.4. are retained for which the electron is reconstructed in a fiducial region of the UA2 central calorimeter, well away from cell edges and cracks.[41] Since the energy reconstruction uncertainties and the relative populations of W and Z events in the various calorimeter regions are different, a restriction to the acceptance of the central calorimeter is necessary to ensure a cancellation of systematic uncertainties.

In the total data sample 2065 $W \to e\nu$ and 95 $Z \to ee$ events have been found with the electrons in the central fiducial region. In order to enlarge the small number of Z events, a second independent Z sample has been defined, where only one electron is required to be in the central fiducial volume. The energy of the second electron was determined by requiring that the total momentum of electrons plus hadrons is balanced in the transverse plane along a direction perpendicular to the bisector defined by the two electron momenta.[41] This results in an independent sample of 156 events. Although the mass resolution for these events is worse compared to the ones of the central Z sample, their mass scale is derived from the energy calibration of the central fiducial region. With the larger number of events they make a significant contribution to the Z mass measurement.

4.1.2. Fitting Procedure

The masses of the W and Z bosons have been determined by using maximum likelihood fitting procedures. The extraction of the Z mass from the measured distribution of the invariant electron pair mass is straightforward and has been performed using an analytic convolution of a relativistic Breit-Wigner with a Gaussian

Table 4. Results of m_W and m_Z fits (statistical errors only).

Sample	Fit Variable	Fitted Mass Value (GeV)
Z (central)	m_{ee}	91.65 ± 0.34
Z (P_T-constrained)	m_{ee}	92.10 ± 0.48
Z (combined)	m_{ee}	91.74 ± 0.28
W	m_T	80.84 ± 0.22
W	P_T^e	80.86 ± 0.29
W	P_T^ν	80.73 ± 0.32

parametrization of the experimental resolution.[46]

For the $W \to e\nu$ decays, the lack of knowledge about the longitudinal momentum of the neutrino forces the use of transverse variables in the fitting procedure. Probability density functions have been obtained numerically for the transverse momenta P_T^e, P_T^ν, and the transverse mass m_T by using a detailed simulation of W production and decay. Important ingredients in this simulation are the rapidity distribution of the W bosons, which is determined from the structure function parametrization, the transverse momentum distribution of the W bosons and the response of the detector to the hadrons in the event. The transverse momentum distribution as well as the response to the recoiling hadrons have been extracted from a detailed study of the $Z \to ee$ events.[46] Unlike in the case of the W, where a neutrino is involved, for Z events the transverse momentum spectrum and the response to hadrons can be measured from the reconstructed electron pair.

The fits to the Z mass spectra are shown in Fig. 9 and the numerical results are listed in Table 4. The analytical likelihood function does not include distortions due to radiative corrections and the underlying event. They have been estimated to lead to a net correction of -60 MeV for the fitted mass values.[46] The results obtained for the two Z samples are in good agreement and their combination gives $m_Z = 91.74 \pm 0.28$ (stat) GeV, after applying this correction.

The results of the W mass fits to the m_T, P_T^e, and P_T^ν spectra are shown in Fig. 10 and the numerical values are listed in Table 4. Since the three variables are not independent, the results cannot be combined to obtain a more precise result. The m_T-fit is used to quote the final result for the W mass, since it is affected by the smaller statistical and systematic (see below) uncertainties.

All fits have been performed by fixing the width of the W and Z to the Standard Model values of 2.1 and 2.5 GeV, respectively. The mass values have been found to be insensitive to these assumptions. If instead the widths are left free in the fit, mass values have been found which differ by less than 20 MeV from the values obtained in the previous fits. For the W and Z widths the values $\Gamma_W = 2.2 \pm 0.4$ (stat) GeV and $\Gamma_Z = 3.2 \pm 0.8$ (stat) GeV have been obtained from the fit.

The most complex aspect of the mass measurements involves the estimation of the systematic errors. A detailed discussion of the various effects can be found in Ref.[46]. A summary of the errors is given in Table 5. The most important contributions to the systematic errors arise from uncertainties in the structure functions, in

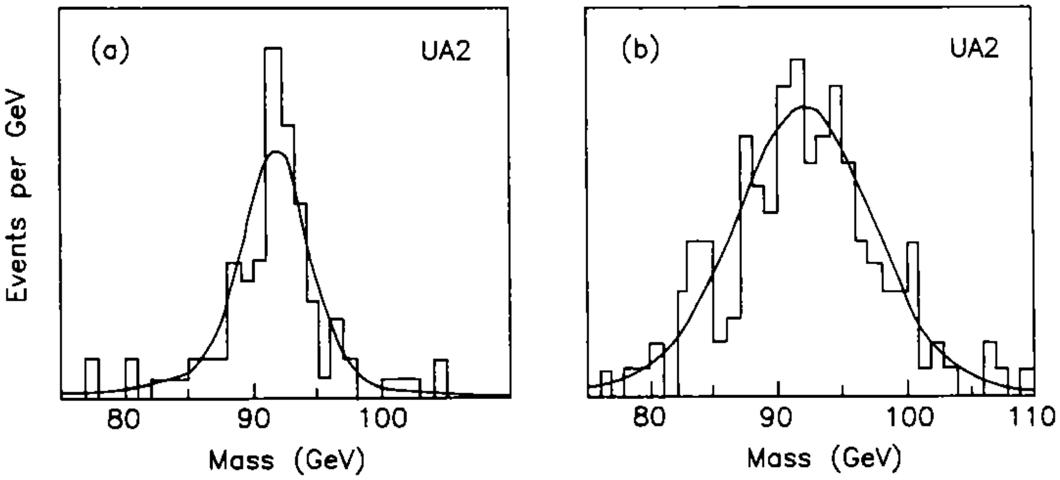

Figure 9. *Fits for m_Z to (a) the central sample and (b) the P_T constrained sample. The curves show the fits, while the histograms show the data.*

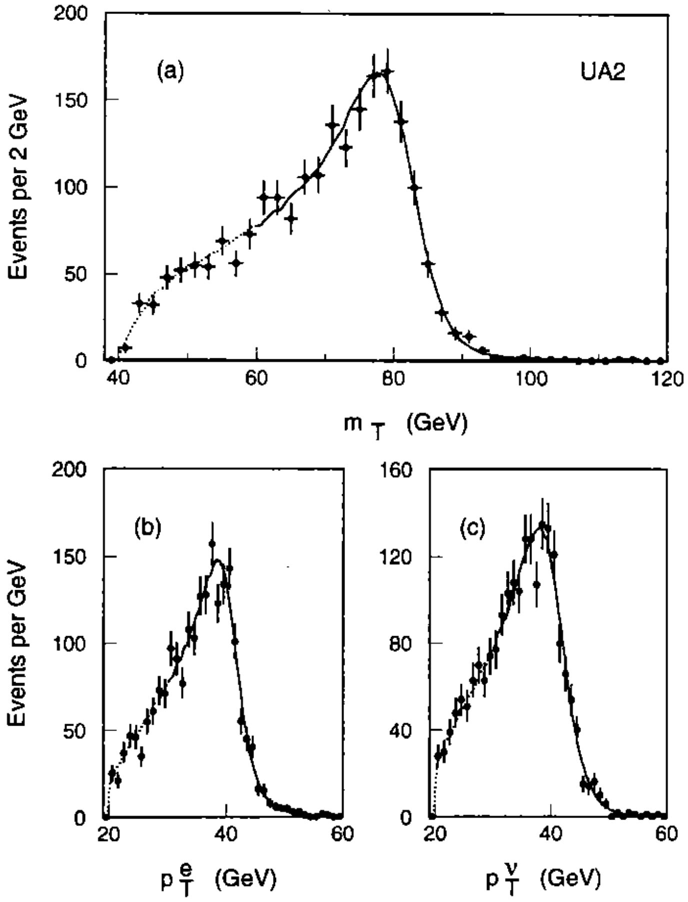

Figure 10. *Fits for m_W for (a) the m_T spectrum, (b) the P_T^e spectrum and (c) the P_T^ν spectrum. The points show the data, while the curves show the fit results with the solid portions indicating the ranges over which the fits are performed.*

the electron energy resolution, in the knowledge of the neutrino energy scale, and finally from uncertainties on the P_T distributions and on the detector response to the recoiling hadrons. In the case of the fits to the transverse momenta P_T^e and P_T^ν for the W mass, there is an additional large contribution arising from the dependence of the electron reconstruction efficiency on the hadronic activity in the hemisphere containing the electron. This effect cancels to first order in the m_T fit.[46]

Table 5. Summary of systematic uncertainties in the measurement of m_W and m_Z (in MeV).

	$\delta m_W\ (m_T)$	$\delta m_W(P_T^e)$	$\delta m_W(P_T^\nu)$	δm_Z cental / P_T const.
structure functions	85	135	105	-
elec. energy resolution	75	100	75	35
neutrino scale	70	-	140	-
P_T^W and P_T^{had}	60	120	90	-
underlying event	30	50	-	50
had. activity in electron hemisphere	25	95	350	-
others	50	75	55	50 / 110
total	160	240	420	80 / 130

4.1.3. Final Results

The final results of the absolute measurement of the W and Z masses from the UA2 experiment are

$$\begin{aligned} m_W &= 80.84 \pm 0.22\ (stat) \pm 0.17\ (syst) \pm 0.81\ (scale) \quad GeV, \\ m_Z &= 91.74 \pm 0.28\ (stat) \pm 0.12\ (syst) \pm 0.92\ (scale) \quad GeV. \end{aligned}$$

The largest errors result from the ±1% uncertainty on the absolute energy scale. These errors cancel in the ratio m_W/m_Z aside from a residual ±80 MeV effect of possible nonlinearities in the calorimeter energy response. The ratio

$$m_W/m_Z \ = \ 0.8813 \ \pm \ 0.0036\,(stat) \ \pm \ 0.0019\,(syst)$$

can be multiplied by the value of m_Z measured at LEP[47], $m_Z = 91.175 \pm 0.021$ GeV, to give a more precise value of the W mass

$$m_W \ = \ 80.35 \ \pm \ 0.33\,(stat) \ \pm \ 0.17\,(syst) \quad GeV.$$

This value is in good agreement with the W mass measured by the CDF experiment, $m_W = 79.91 \pm 0.39$ GeV.[48] If both results are combined the value

$$m_W \ = \ 80.14 \ \pm \ 0.27 \ \ GeV$$

is obtained, where the statistical and systematic errors have been added in quadrature.

4.2. $\sin^2\theta_W$ *and the Top Quark Mass*

The measurement of the ratio of the vector boson masses is equivalent to the measurement of the weak mixing angle $\sin^2\theta_W$. Using the on-shell renormalization scheme,[10] where $\sin^2\theta_W$ is defined to all orders as $\sin^2\theta_W = 1 - (m_W/m_Z)^2$, the collider measurements can be translated into:

$$\begin{aligned} \sin^2\theta_W &= 0.2234 \pm 0.0072 && (UA2), \\ \sin^2\theta_W &= 0.2274 \pm 0.0052 && (UA2+CDF). \end{aligned}$$

As discussed in Sect. 2.2. electroweak radiative corrections modify the Born level predictions for the boson mass values. The dependence of the W mass on the mass of the top quark and the mass of the Higgs in the Standard Model is illustrated in Fig. 11. From the UA2 result it can be concluded that

$$\begin{aligned} m_t &= 160\,^{+50}_{-60}\ GeV && for \quad m_H = 100\ GeV \ \ and \\ m_t &< 250\ \ GeV \qquad (95\%C.L.) && for \quad m_H < 1\ TeV. \end{aligned}$$

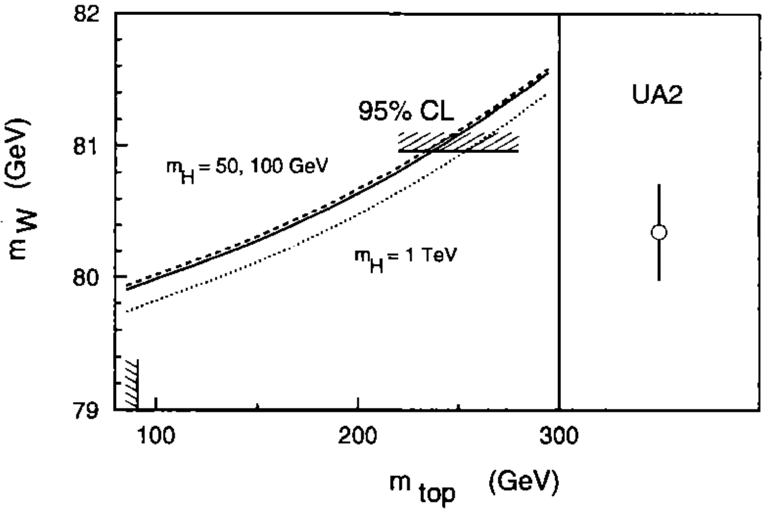

Figure 11. *The final result for m_W is compared with the Standard Model prediction for m_W as a function of m_t and m_H. The dotted, solid and dashed curves correspond to Higgs masses of 50, 100 and 1000 GeV, respectively.*

4.3. *Determination of the W Width*

As discussed in Sect. 2.2., the total width of the W, Γ_W, gives information about the decay modes of the W, regardless whether or not they are observable. For example, it is sensitive to the existence of a top quark lighter than the W, so that the measurement of Γ_W can be used to set a lower limit on the top quark mass. In contrast to direct top searches at hadron colliders,[49,50] no assumptions on the top decay mode need to be made. Direct searches use the semileptonic branching ratio for top decays as expected in the Standard Model, an assumption which could be invalid, for example, if top decays via a charged Higgs boson H^+ were allowed.[15]

As shown in the previous section, the fits to the transverse variables are not very sensitive to the W width. A more precise, albeit indirect measurement can be derived from the measurement of the ratio $R = \sigma_W^e/\sigma_Z^e$ of the W and Z production cross sections, multiplied by the appropriate branching ratios for the electron channels. If this ratio is considered the rather large experimental uncertainties on the individual cross section measurements, resulting from uncertainties on the luminosity or on the reconstruction efficiencies, cancel to a large extent.

From the UA2 W and Z cross section measurements (see Sect. 5.7.), R can be extracted to be

$$R \;=\; 10.4\,^{+0.7}_{-0.6}(stat) \pm 0.3(syst).$$

Theoretically the ratio R can be expressed as

$$R \;=\; \frac{\sigma_W^e}{\sigma_Z^e} \;=\; \frac{\sigma_W}{\sigma_Z}\frac{\Gamma_{W\to e\nu}}{\Gamma_{Z\to ee}}\frac{\Gamma_Z}{\Gamma_W}, \tag{22}$$

where σ_W (σ_Z) represent the total W (Z) production cross sections and $\Gamma_{W\to e\nu}$ $(\Gamma_{Z\to ee})$ are the partial decay widths. The first term on the right hand side of the equation can be computed in QCD calculations to the order $\mathcal{O}(\alpha_s^2)$.[23] Structure function uncertainties, which strongly affect the individual cross section measurements, partially cancel in the ratio. Despite this cancellation, they still remain the source of the dominant theoretical error on R. Due to the different couplings of the W and Z to up- and down-type quarks, the remaining uncertainties arise mainly from uncertainties in the d/u ratio in the parton density functions. Recent data from deep inelastic scattering experiments[51] on the measurement of the structure function ratio F_2^n/F_2^p have been exploited to restrict the range of σ_W/σ_Z, leading to $\sigma_W/\sigma_Z = 3.26 \pm 0.09$.[44] The ratio of the partial widths is sensitive to the boson masses and to $\sin^2\theta_W$, but given the experimental bounds on m_W and m_Z, the effect on R is at the level of ±0.6% only. Assuming the standard gauge couplings of electrons, electron neutrinos and light quarks also the second term of Eq. (22) can be computed reliably. Using the value $\Gamma_Z = 2.487 \pm 0.010$ GeV from LEP,[47] one obtains

$$\Gamma_W = 2.10 \pm\, ^{0.14}_{0.13}\,(stat) \pm 0.08(syst)\;\; GeV.$$

The UA1 and CDF Collaborations have performed similar measurements. Using the R values reported by these experiments together with the same theoretical inputs as used in the UA2 measurement, the results given in Table 6 are obtained. The predictions for Γ_W as a function of the top quark mass m_t are shown in Fig. 12. From the UA2 measurement of the W width a limit of $m_t > 53$ GeV at the 95% confidence level can be extracted. A combination of the results of the UA1, UA2 and CDF experiments leads to $m_t > 55$ GeV at a confidence level of 95%. Recently,

Table 6. Compilation of Γ_W measurements.

Experiment		int. luminosity		Γ_W (GeV)
UA1	Ref.[52]	5.3 pb^{-1}	(1983-1989)	2.19 ± 0.30
UA2	Ref.[44]	13.0 pb^{-1}	(1988-1990)	2.10 ± 0.16
CDF	Ref.[53]	4.4 pb^{-1}	(1988-1989)	2.20 ± 0.16
CDF, prel.	Ref.[54]	18.4 pb^{-1}	(1992-1993)	2.03 ± 0.09
D0, prel.	Ref.[54]	7.4 pb^{-1}	(1992-1993)	2.08 ± 0.25

the CDF and D0 Collaborations have presented new measurements of Γ_W based on large data samples collected during the 1992/93 running period at Fermilab. The preliminary results of these measurements[54] are also included in Table 6. If these values are taken into account, the lower bound for the top quark mass increases to $m_t > 62$ GeV at the 95% confidence level. Apart from these measurements, the best limit on m_t, which does not depend on the top decay modes, comes from the LEP experiments which established a limit of $m_t > 46$ GeV.[55]

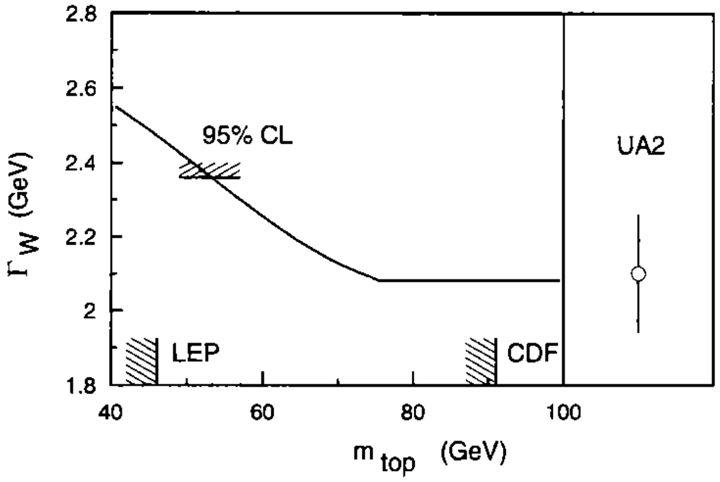

Figure 12. *Comparison of the Γ_W measurement with the Standard Model prediction as a function of the top quark mass.*

4.4. Test of Electron Tau Universality

The gauge structure of the electroweak theory imposes a universal weak coupling strength between the gauge bosons and all generations of leptons and quarks. From measurements of the partial decay width of the Z to charged leptons and to various quark flavours, the LEP experiments have demonstrated the universality of the neutral current coupling with an impressive precision.[56] A direct measurement of the universality of the charged current coupling can be performed in W production at hadron colliders. The UA2 Collaboration has performed a precise measurement of the ratio of branching fractions

$$R_B = \frac{Br(W \to \tau\nu_\tau)}{Br(W \to e\nu_e)},$$

which, if lepton masses relative to the W mass are neglected, is simply the ratio of the squares of the charged current coupling of the tau and electron to the W boson, $(g_\tau^W/g_e^W)^2$.

Since the UA2 detector has no muon detection system, the test of the universality of the W couplings has been restricted to electrons and taus. In the study of $W \to \tau\nu$ decays, the hadronic τ decays have been considered, resulting in events containing a collimated jet with high P_T accompanied by large missing transverse momentum. In contrast to the electrons, taus cannot be identified on an event by event basis and consequently a statistical analysis has been used to determine the contribution of the $W \to \tau\nu$ events in the data. The principal background results from QCD jet production, which, due to its large cross section, makes the analysis challenging in a hadron collider environment. The discrimination between the tau signal events from W decays and the jet background is provided by requiring a leading jet cluster with transverse energy $E_T^1 > 22$ GeV in the central rapidity range ($|\eta| < 2.0$) in conjunction with missing transverse momentum ($\not{P}_T > 25$ GeV). Two-jet configurations have been further suppressed by requiring that there is no jet cluster opposite in azimuth to the leading one with a transverse energy exceeding a threshold E_T^{opp}. For the choice $E_T^{opp} = 2.5$ GeV, $\sim$ 1800 events fulfilling this selection have been found in the total data sample. They represent a mixture of electrons, taus, remaining jet background, and background resulting from beam-halo events. Electrons from W decays have been identified by applying electron identification criteria and have been removed from the sample.[57] In order to determine the exact composition of the remaining sample and to extract the tau fraction, two additional variables have been used, the hadronicity ξ and the profile ρ of the leading jet cluster, which are defined as

$$\xi = \frac{E_{had}}{E_{tot}} \qquad \textit{and} \qquad \rho = \frac{E(1)+E(2)}{E_{tot}},$$

where E_{had} is the cluster energy in the hadronic calorimeter, E_{tot} the total cluster energy, and E(1) and E(2) the energies of the two leading cells in the cluster. Figure 13a shows the ρ distribution for the leading cluster in the data. For comparision, Fig. 13b illustrates the ρ distribution for jets and taus from Monte Carlo generated $W \to \tau\nu_\tau$ events, including a full detector simulation. The comparison of the two distributions indicates the presence of a significant τ signal in the high profile region ($\rho > 0.75$). After background subtraction, 273 ± 23 tau events and 1274 ± 48 electron events have been found in the total data sample with $\rho > 0.75$. After accounting for the relative acceptance between taus and electrons, which has been determined by Monte Carlo simulations to be 0.209 ± 0.005, one obtains the result

$$\frac{g_\tau^W}{g_e^W} = 1.02 \pm 0.04\,(stat.) \pm 0.04\,(syst).$$

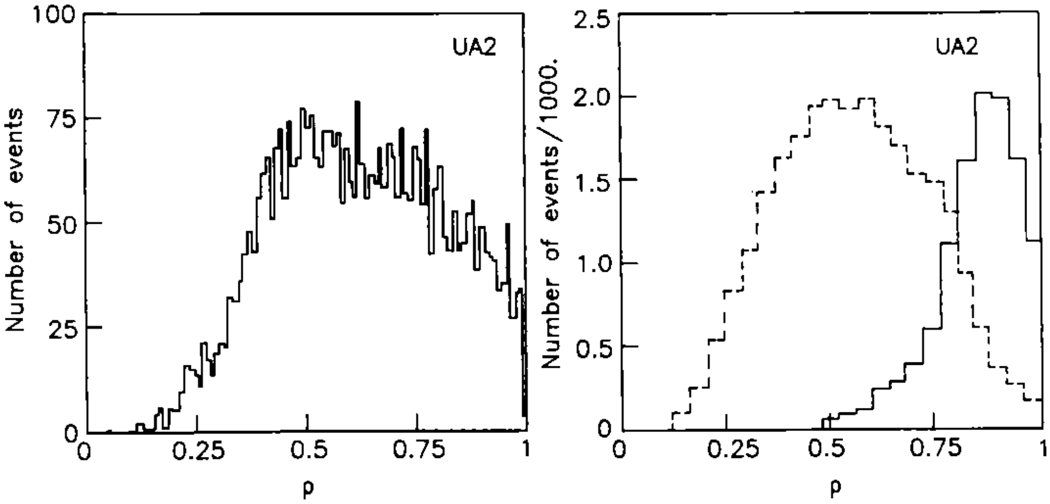

Figure 13. *Cluster profile ρ distribution for the leading cluster in events passing the τ selection criteria. (a) Data, (b) Monte Carlo for $W \to \tau\nu$ events (full line) and jets from two-jet events (dashed line).*

The systematic uncertainties result mainly from uncertainties in the calculation of the detection efficiencies and from uncertainties in the jet and halo background subtraction.

The result is in agreement with the Standard Model prediction of one and also with the measurements of the UA1 and CDF experiments:[58,59]

$$\begin{array}{ll} UA1: & g_\tau^W/g_e^W = 1.01 \pm 0.10 \;\; (stat \oplus syst), \\ CDF: & g_\tau^W/g_e^W = 0.97 \pm 0.07 \;\; (stat \oplus syst). \end{array}$$

4.5. Hadronic Decays of W and Z

Intermediate vector bosons are expected to decay predominatly ($\sim 70\%$) into quark antiquark pairs, which then evolve into jets. The direct observation of such decays represents an important test of the predictions of the electroweak Standard Model. However, despite the relatively high event rate, its experimental confirmation in a hadron collider environment represents a big experimental challenge. The difficulty arises from the need to detect a signal which appears as an excess of only a few percent over a copious background of two-jet events produced by the strong interaction between colliding partons. Essential for an experimental observation are both a large integrated luminosity and a very good two-jet mass resolution.

In the 1989 collider run, where data corresponding to an integrated luminosity of $4.7\,pb^{-1}$ were collected, the UA2 Collaboration has made a special effort to meet the experimental requirements. In order to cope with the high rate of two-jet events, a dedicated trigger was set up to allow for a sampling of two-jet events down to two-jet mass values, m_{jj}, as low as 48 GeV.[60] In order to obtain a more favourable signal to background ratio, the jet identification was restricted to the central calorimeter region. The two-jet mass resolution was optimized in the analysis by applying strict selection criteria:

- jets had to be well contained in the acceptance of the central calorimeter, both laterally ($| \eta_{jet} | < 0.7$) and longitudinally;
- events containing a third jet with a transverse energy greater that 20 GeV were rejected.

In addition, an optimized cone algorithm with an opening angle of $R^2_{cone} = \Delta\eta^2 + \Delta\phi^2 = 0.64$ was used. For this opening angle an optimum in the jet-jet mass resolution was found, which was estimated to be $10.7 \pm 2.4\%$ in the mass range $70 < m_{jj} < 100$ GeV. Remaining $Z \to ee$ events were removed from the sample by requiring that the energy fraction deposited in the electromagnetic calorimeter was below 80% of the jet energy.

To search for the W $\to q\overline{q}$ signal in the observed two jet mass spectrum, a statistical analysis was applied. The mass spectrum in the range between 48 and 300 GeV was originally fitted with several smooth functions, such as, for example, $d\sigma/dm \sim m^{-\alpha}e^{-\beta m}e^{-\gamma m^2}$ with the three fit parameters α, β and γ. All attempts gave rather poor fit qualities, which originated entirely from the mass range $70 < m_{jj} < 100$ GeV. If instead the fit was performed by assuming a superposition of two Gaussian signals $S(m_W, \sigma_m, N)$ on top of a smooth background $B(\alpha, \beta, \gamma)$, a good fit was obtained. The position (m_W), the width (σ_m), and the size of the signal (N) were left free. The only assumptions made on the line shapes were:

- a fixed value for the mass ratio, $m_Z/m_W = 1.13$, and
- a fixed value for the relative contributions to the signal size, $n_W/n_Z = 0.397$ (Ref.[60]).

The best fit to the two-jet mass spectrum, shown together with the data in Fig. 14, gave the results:

$$\begin{aligned} N &= 5618 \pm 1334, \\ m_W &= 79.2 \pm 1.7\ GeV, \qquad\qquad \chi^2/NDF = 114/121, \\ \sigma_m &= 9.9 \pm 2.5\%. \end{aligned}$$

The mass resolution as well as the fitted mass value are found to be in agreement with the expected values from Monte Carlo simulations. From the known W and Z masses and branching ratios, a simulation of this experiment predicts an average significance of 3.6 standard deviations (s.d.) with a spread of 1.4 s.d., which is in agreement with the 4.2 s.d. measured in the actual experiment. Taking the experimental efficiency and the acceptance into account, the signal can be expressed in a cross section $\sigma Br(W, Z \to q\overline{q}) = 9.6 \pm 2.3\ (stat) \pm 1.1\ (syst)$ nb, which can be compared to the theoretical prediction, including $\mathcal{O}(\alpha_s^2)$ corrections,[23] of 5.8 nb.

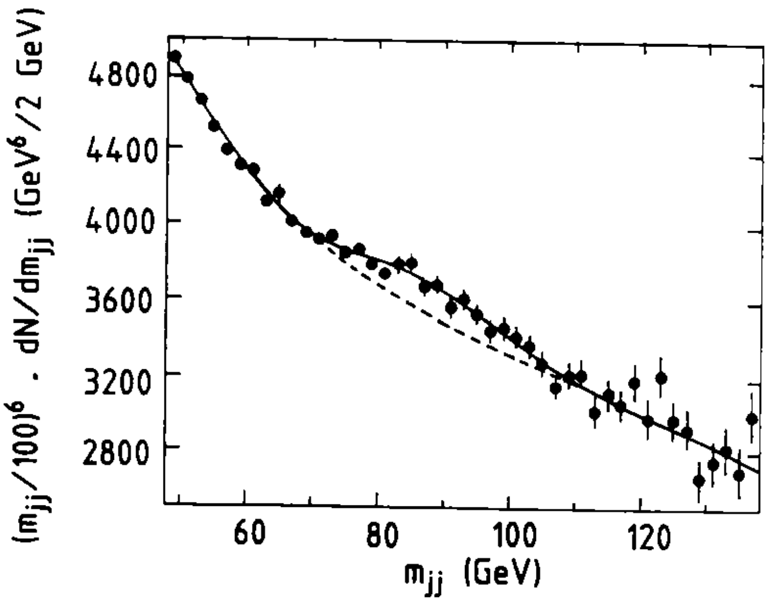

Figure 14. *The two-jet mass spectrum in the region around the expected W,Z signal. The observed event numbers have been weighted by a factor* $(m/100)^6$. *The best fit is overlayed on the data, the dashed line represents the background contribution only.*

A direct comparison of this measurement with the measurements of the W and Z boson cross sections times their electronic branching ratios avoids the theoretical uncertainties on the cross section calculations arising from structure functions and from higher order QCD corrections. The ratio

$$R_{q\bar{q}} = \frac{\sigma_W Br(W \to q\bar{q}) + \sigma_Z Br(Z \to q\bar{q})}{\sigma_W Br(W \to e\nu)\frac{\Gamma_{W\to q\bar{q}}}{\Gamma_{W\to e\nu}} + \sigma_Z Br(Z \to ee)\frac{\Gamma_{Z\to q\bar{q}}}{\Gamma_{Z\to ee}}} \tag{23}$$

is expected to be one in the Standard Model. Combining the ratio of partial widths as calculated in the Standard Model with the experimental cross section measurements results in

$$R_{q\bar{q}} = 1.71 \pm 0.45,$$

which is in reasonable agreement with the Standard Model expectation.

In conclusion, this analysis has provided evidence for the hadronic decay modes of the W and Z bosons. Although agreement with the Standard Model expectation has been found, the experimental uncertainties do not allow for a precise determination of the $W - q\bar{q}$ couplings. This measurement demonstrates both the potential as well as the limitations of jet spectroscopy at hadron colliders.

4.6. Measurement of the $W-\gamma$ Coupling

The self interactions among gauge bosons, as predicted in the Standard Model, are still awaiting direct experimental confirmation. Given the energy of the CERN collider and the integrated luminosity delivered to the UA2 experiment, only the WWγ coupling is expected to lead to sizeable event rates. In the most general ansatz,[61] which assumes Lorentz invariance and imposes P,C and T conservation, in addition to the charge e, two independent parameters, κ and λ, are needed to specify the WWγ coupling. These parameters are related to the magnetic dipole (μ_W) and electric quadrupole (Q_W) moment of the W by the equations

$$\begin{aligned} \mu_W &= \frac{e}{2m_W}(1+\kappa+\lambda), \\ Q_W &= -\frac{e}{m_W^2}(\kappa-\lambda). \end{aligned} \tag{24}$$

In the Standard Model, the values of κ and λ are fixed to be $\kappa = 1$ and $\lambda = 0$. Any deviations from these values would indicate physics beyond the Standard Model, like, for example, compositness of the W bosons.[62]

In order to study the WWγ coupling, the UA2 Collaboration has searched for the process $p\bar{p} \rightarrow W\gamma + \ldots \rightarrow e\nu\gamma + \ldots$. The lowest order contributions to these final states are shown in Fig. 15.

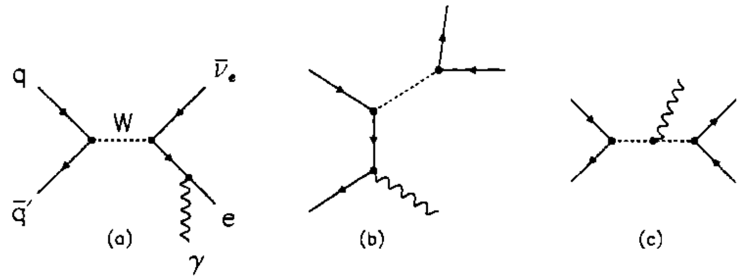

Figure 15. *Lowest order Feynman diagrams for the process* $p\bar{p} \rightarrow e\nu\gamma$.

Among these diagrams only diagram (c) is directly sensitive to the WWγ vertex and provides the dependence of physical observables on κ and λ. If κ or λ take values different from the Standard Model predictions, the cross section for the process $q\bar{q} \rightarrow e\nu\gamma$ increases.[63,64] Thus any significant excess of events measured in this channel will be an indication for physics beyond the Standard Model. In addition, some differential distributions, like, for example, the transverse momentum of the photon (P_T^γ) or the invariant mass of the $W\gamma$-system, depend strongly on κ and λ. They will provide powerful tools for testing anomalous couplings with high sensitivity at future hadron colliders or at LEP200.[65]

The UA2 analysis is based on the total W $\rightarrow e\nu$ event sample, in which additional photon candidates have been searched for. The photons are required to be in the central calorimeter ($|\eta| < 1.0$), separated in space from the electron by at least 15 degrees and to have a transverse momentum above 4.5 GeV. These selection criteria

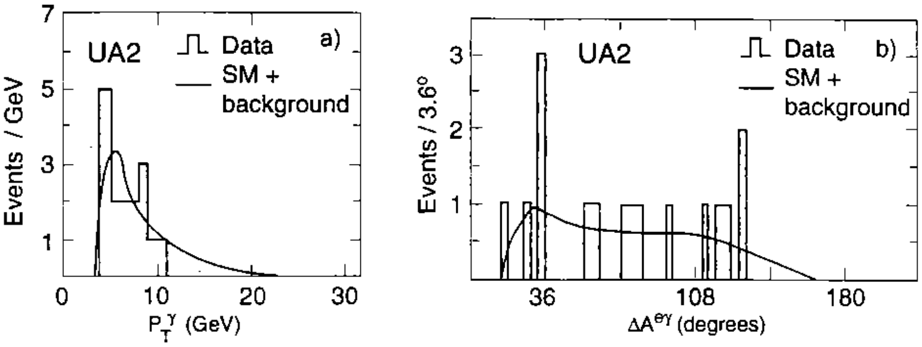

Figure 16. *a) The photon transverse momentum distribution (P_T^γ), b) the space angle between electron and photon ($\Delta A^{e\gamma}$) for the 16 candidate events. Superimposed are the standard model predictions including the estimated background contributions.*

largely suppress the contributions from radiative W decays and initial state photon radiation (diagrams (a) and (b) from Fig. 15). In the total sample, 16 Wγ candidates have been found with an estimated background of 6.8 ± 1.0 events leading to a signal of $9.2^{+5.2}_{-3.2}$ events. The principal background results from the associated production of W's with a jet, where the jet is misidentified as a photon.[66]

The Standard Model prediction has been calculated with the Monte Carlo programs of Ref.[64,67] and has been corrected for acceptance and efficiencies. In total, 11.9 ± 1.1 events are predicted, in good agreement with the experimental observation. Comparisons between the data and the Standard Model prediction for the P_T^γ distribution and for the distribution of the angle between the electron and the photon, ($\Delta A^{e\gamma}$), are shown in Fig. 16. Within the large statistical errors the agreement is good. The dependence of the expected $W\gamma$ event rates on κ and λ are shown in Fig. 17. The theoretical uncertainties are estimated to be of the order of ±9%[66] and are represented by the band defined by the two extreme parabolae. Comparing the UA2 measurement to these predictions, limits of

$$\begin{array}{llllll} -5.3 & < \kappa & < 7.9 & for\ \lambda = 0 & (95\%\ C.L.) & and \\ -4.4 & < \lambda & < 4.4 & for\ \kappa = 1 & (95\%\ C.L.) & \end{array}$$

can be extracted. These limits can still be improved if instead of the event rate the P_T^γ distribution is compared between data and theory using maximum likelihood methods. In this case the limits

$$\begin{array}{llllll} -3.5 & < \kappa & < 5.9 & for\ \lambda = 0 & (95\%\ C.L.) & and \\ -3.6 & < \lambda & < 3.5 & for\ \kappa = 1 & (95\%\ C.L.) & \end{array}$$

are obtained. The 68% and 95% confidence level contours in the $\kappa - \lambda$ plane, as computed using the likelihood method, are shown in Fig. 17c.

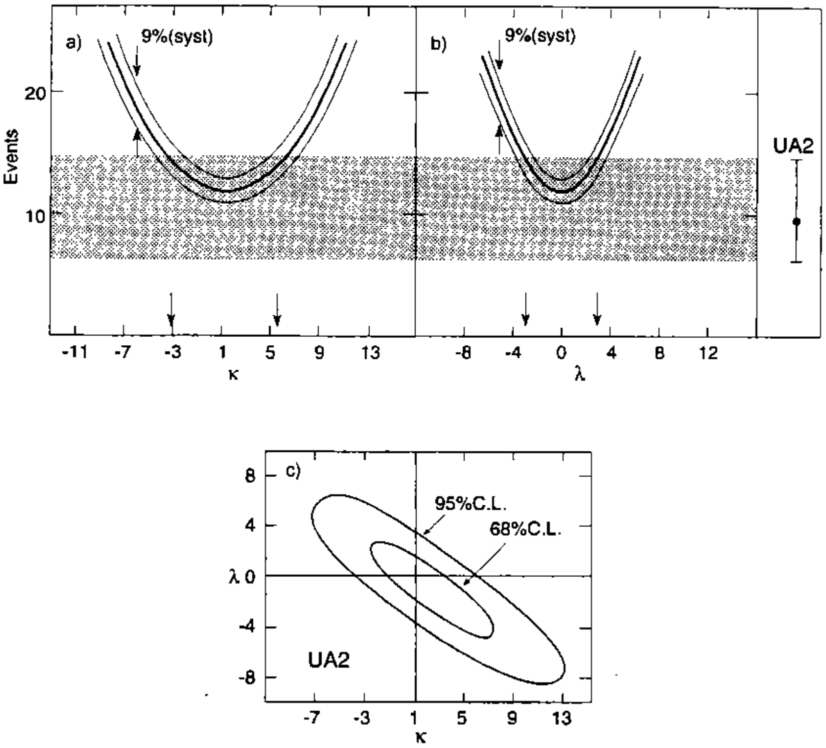

Figure 17. *The Monte Carlo predictions for the number of expected events a) as a function of κ for $\lambda = 0$, and b) as a function of λ for $\kappa = 1$. c) The 68% and 95% confidence level contours in the $\kappa - \lambda$ plane from the maximum likelihood method.*

It should be noted that the limits presented here significantly improve the existing limits on the anomalous W couplings.[68] Furthermore, they do not depend on cutoffs or regularization schemes and are largely model independent.[66] In a similar analysis performed by the CDF Collaboration, based on data corresponding to 4.6 pb^{-1}, comparable limits for κ and λ have been found:[69] $-5.6 < \kappa < 8.0$ for $\lambda = 0$, and $-3.2 < \lambda < 3.1$ for $\kappa = 1$.

4.7. Direct Search for the Top Quark

One of the ingredients of the Standard Model still lacking direct experimental confirmation is the top quark. Up to date there exists only indirect evidence for its existence. The forward backward asymmetry measured in $e^+e^- \rightarrow b\bar{b}$ and the absence of flavour changing neutral currents in bottom quark decays imply the existence of the iso-doublet partner of the b quark.[70,71]

In $p\bar{p}$ collisions two processes contribute to top quark production, the production via a W boson which decays into a $t\bar{b}$ pair and the strong production of $t\bar{t}$ pairs via quark antiquark annihilation or gluon fusion:

$$\begin{aligned} p\bar{p} &\rightarrow W + \ldots \rightarrow t\bar{b} + \ldots, \\ p\bar{p} &\rightarrow t\bar{t}. \end{aligned}$$

The cross section for the first process is well known since it can be deduced from the measured cross section $p\bar{p} \rightarrow W + ... \rightarrow e\nu + ...$, once phase space and colour factors are taken into account. As discussed in Sect. 2.2., higher order QCD processes become important if the mass of the top quark is close to that of the W boson. For example, for $m_W = 80.2$ GeV and $m_t = 65$ GeV, the QCD correction factor takes the value of 1.5.[17] The cross section for the second process has been calculated in next to leading order perturbation theory.[72] The main uncertainties in this calculation arise from uncertainties in the QCD scale parameter Λ and from ambiguities in the choice of the renormalization scale μ. They have been estimated in Ref.[73] to be ± 30%. The calculated production cross sections are shown in Fig. 18 as a function of the top quark mass. The uncertainties for the $t\bar{t}$ part are indicated on the figure.

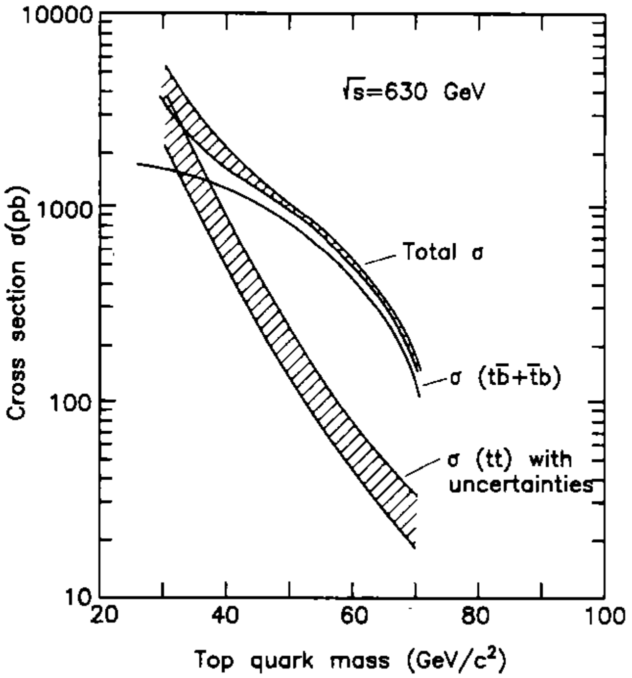

Figure 18. *Cross sections for top quark production in $p\bar{p}$ interactions at $\sqrt{s} = 630$ GeV.*

Decays of the top quark into final states containing only hadronic jets are very difficult to distinguish from the large background resulting from QCD jet production. The search for the top quark therefore needs to be performed using the semileptonic top decay mode

$$t \rightarrow b\ e\ \nu_e,$$

which has a branching ratio of approximately 1/9 in the Standard Model. In this case, the signature of top quark production consists of events containing an electron, a neutrino and one or more hadronic jets in the final state.

The UA2 Collaboration has performed a direct search for the production of the top quark in the data collected in the years 1988 and 1989, corresponding to an integrated luminosity of 7.4 pb^{-1}. To search for top candidates in the UA2 data the following selection criteria have been applied:

- electron identification in the central calorimeter ($|\eta| < 1.0$) with $P_T^e > 12$ GeV;
- missing transverse momentum $\not{P}_T > 15$ GeV;
- at least one jet with $E_T^1 > 10$ GeV in the pseudorapidity range $|\eta| < 2.2$; in order to suppress background from jet production, events with the leading jet opposite in azimuth to the electron candidate ($\Delta\phi_{e-jet\ 1} > 160°$) have been rejected.

These cuts are satisfied by 137 events for which the transverse mass distribution is shown in Fig. 19.

The acceptance for the signal events together with the expected transverse mass distributions have been estimated for both production processes by using the Monte Carlo program of Ref.[74]. For a top quark in the mass range between 30 and 70 GeV, the acceptance has been found to vary from 1.8% to 15.3% for events resulting from $t\bar{b}$-production and from 1.9% to 35.5% for $t\bar{t}$-events. The number of top signal events is expected to vary between 39.2 for $m_t = 30$ GeV and 11.5 for $m_t = 70$ GeV. For top quark masses in this range, most events are expected to have transverse masses of the electron neutrino system in the range between 15 and 50 GeV. Out of the total number of predicted top events, 33.4 and 8.3 for top masses of 30 and 70 GeV, respectively, are expected to have transverse masses in this range.

The total number of 137 observed events as well as the shape of their transverse mass distribution have been found to be consistent with the expected background.[49] This background is mainly composed of events resulting from the associated production of W's and jets, with small contributions from $b\bar{b}$ and $Z \to ee, \tau\tau$ production as well as from QCD jet background.

Limits on the top quark mass have been extracted by comparing the observed m_T distribution with the one expected from background sources alone, and also by including contributions from a top quark with a given mass. In each case, the lowest number of expected signal events consistent with systematic uncertainties has been assumed; i.e., using the lower theoretical estimate of the $t\bar{t}$ cross section, ignoring the QCD corrections in the $t\bar{b}$ case, and using the lowest values consistent with systematic uncertainties for the efficiency and acceptance values. A likelihood fit has been performed with two free parameters giving the fractions of the event sample due to top quark decays and W events. The overall likelihood normalization has been constrained to the total number of 137 observed events. For each value of m_t the fitted signal was found to be consistent with no top production. Figure 19 shows the best fit to the data with no top quark contribution. The sum of the background and of the lowest expected contribution from top quark production with $m_t = 65$

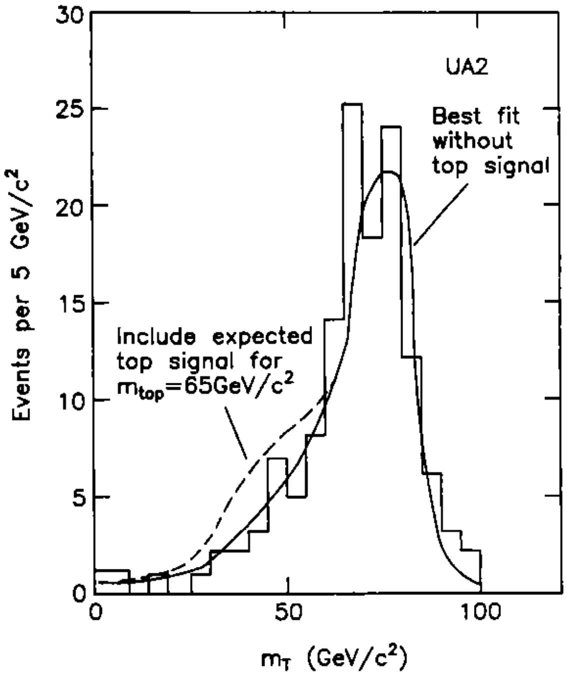

Figure 19. *Best fit (full curve) to the M_T distribution with no top signal. The lowest expected contribution from top (m_t = 65 GeV is added (dashed curve).*

GeV is represented by the dashed line. The fit excludes this hypothesis at the 99% confidence level. With a confidence level of 95% (90%) top quark masses in the range between 30 and 69 (71) GeV can be excluded.

The UA1 and CDF Collaborations have also presented limits on the top quark mass from similar analyses, searching for semileptonic top decays in the lepton (e,μ) + jet channels. They also have reported searches using lepton pairs, resulting

Table 7. Top quark mass limits from direct searches in $p\bar{p}$ experiments.

Experiment		int. luminosity		decay mode	lower top quark mass limit, 95 % C.L.
UA1	Ref.[75]	4.6 pb^{-1}	(1988-1989)	μ + jet	53 GeV
		5.4 pb^{-1}	(1988-1989)	$\mu\mu$ + jet	46 GeV
				combined	60 GeV
UA2	Ref.[49]	7.6 pb^{-1}	(1988-1989)	e + jet	69 GeV
CDF	Ref.[76]	4.1 pb^{-1}	(1988-1989)	e + jet	77 GeV
	Ref.[77]			eμ	72 GeV
	Ref.[50]			ee, eμ, $\mu\mu$, $\oplus$e, μ + jet, incl. b-tagging	91 GeV
CDF prel.	Ref.[78]	25.5 pb^{-1}	(1988-1993)	ee, eμ, $\mu\mu$	113 GeV
D0 prel.	Ref.[79]	7.5 pb^{-1}	(1992-1993)	ee, eμ	99 GeV

from the double semileptonic decay of a produced $t\bar{t}$ pair. In addition, CDF has searched in the lepton + jet events for a low transverse momentum muon as a tag of a bottom quark from $t\bar{t} \rightarrow W^+bW^-\bar{b}$ decays, theirby reducing the dominant background from W + jet production. A compilation of the results obtained by the various experiments is given in Table 7. The most stringent limit is obtained by the CDF experiment from a combination of the dilepton and the lepton + jet searches, resulting in $m_t > 91$ GeV at the 95% confidence level. In the meantime, also this has been superseded by new limits extracted by the CDF and D0 experiments based on their new large data samples collected in the years 1992 and 1993. Preliminary analyses indicate that with a 95% confidence level the top quark is heavier than 113 GeV.

5. Tests of Quantum Chromodynamics

Since its early operation the CERN $p\bar{p}$ Collider has been an excellent facility to study the properties of high transverse momentum processes. Due to the high momentum transfer such processes allow for a comparison to the predictions of perturbative Quantum Chromodynamics (QCD). Already in the early days, the gross features of the parton parton interaction could be well described by leading order QCD calculations. Given the large progress in both the experimental and the theoretical field, more quantitative comparisons become possible with the present collider data. This report focuses on a confrontation of the experimental data of the UA2 experiment with recent theoretical predictions for a variety of different hard scattering processes:

- the production of jets with high transverse momentum, including a study of three- and four-jet events; the study of four-jet events is used to search for a possible contribution from multiparton scattering;
- the direct production of isolated high P_T photons;
- the production of W and Z events; the associated production of W's with jets is used to determine the strong coupling constant α_s.

For the study of jet production, data corresponding to an integrated luminosity of 7.4 pb^{-1} collected in the years 1988 and 1989 have been used. The study of direct photon and W production is based on the complete data set corresponding to an integrated luminosity of 13.0 pb^{-1}.

5.1. Inclusive Jet Production

The fundamental parton parton scattering processes, like, for example, $qq \rightarrow qq$ or $qg \rightarrow qg$, can be studied by measuring the production of large transverse momentum jets. These studies provide a basic test of Quantum Chromodynamics and can be considered as the QCD analog of fundamental scattering processes like $e^+e^- \rightarrow e^+e^-$ in Quantum Electrodynamics.

The UA2 Collaboration has measured the jet inclusive transverse momentum spectrum $d^2\sigma/dP_Td\eta$ and has performed a comparison to leading order QCD calculations. Jets have been reconstructed using the cone algorithm with a radius $R_{cone} = 1.3$ and using the merging option (see Sect. 3.3.). The choice of such a large cone radius aims at reconstructing the original parton energy of two-parton scattering as precisely as possible. On the other hand, any sensitivity to final state gluon radiation is lost, since radiated gluons are merged together with the leading final state partons. The measured inclusive jet cross section $d^2\sigma/dP_Td\eta$ is shown in Fig. 20 as a function of the transverse momentum P_T, separately for five different $|\eta|$-intervals over the range $0 < |\eta| < 2$. The cross sections have been corrected for acceptance and efficiency losses as well as for the detector response to jets, with the aim of reconstructing the original parton transverse momentum. These corrections

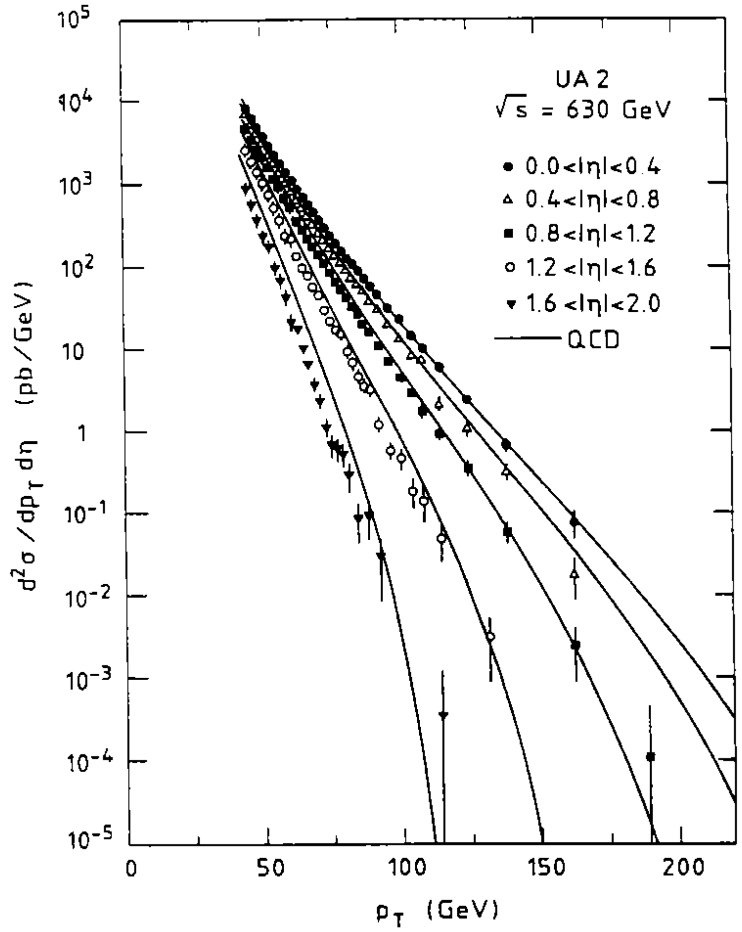

Figure 20. *Inclusive jet cross section* $d^2\sigma/dP_Td\eta$ *in pb/GeV for different bins of pseudorapidity* η. *The systematic scale uncertainty of* $\pm 32\%$ *is not shown. The curves represent an* $\mathcal{O}(\alpha_s^2)$ *QCD calculation with* $\mu = (P_T/2)$.

have been determined using the event generation of Ref.[80] and the fragmentation scheme of Ref.[81] together with a detailed simulation of the calorimeter response. The errors shown represent a combination of the statistical and the P_T dependent systematic uncertainties. On top of these, there is a P_T independent uncertainty of ±32%. The dominant errors result from uncertainties in the calculations of the acceptance corrections (fragmentation, jet algorithm), uncertainties in the underlying event simulation (P_T dependent) and from uncertainties on the absolute jet energy scale of the calorimeter.[82] It is interesting to note that in earlier measurements[83] the dominant experimental error was due to uncertainties on the jet energy scale, which typically introduced an uncertainty of ±35% on the steeply falling P_T spectrum. During the UA2 upgrade programme a large effort has been made to keep calorimeter calibrations under control, so that the scale uncertainty could be reduced to ±11%.

A leading order QCD calculation, $\mathcal{O}(\alpha_s^2)$, is compared to the data in Fig. 20.

This calculation uses the scale $\mu = (P_T/2)$ together with the structure function parametrization of Ref.[84]. For central rapidity values, the agreement with the experimental data is excellent, both in terms of the P_T dependence and of the absolute cross section values. However, it should be stressed that the leading order calculation shows a large sensitivity to the choice of the renormalization scale μ and therefore the agreement of the absolute rates is largely accidental. At increasing values of $|\eta|$ only a marginal agreement is found, with differences of almost a factor of two for $1.6 < |\eta| < 2.0$. Apart from the uncertainty resulting from the definition of the renormalization scale, the largest theoretical uncertainty results from uncertainties in the structure functions. In the rapidity interval $1.6 < |\eta| < 2.0$ they introduce an error in the order of ± 30% on the theoretical predictions.[82] It should be noted that there is no known systematic effect which could explain such a discrepancy. There is no clear explanation yet and the hope is that the ongoing experiments at the Fermilab collider will clarify the situation in the future, possibly by taking into account next to leading order calculations[20] for different rapidity intervals.

Inclusive jet cross sections measurements have also been performed by the UA1 and CDF Collaborations.[85,86] They also find good agreement between the measured cross sections and the QCD predictions, which in the case of CDF already include the next to leading order contributions.

5.2. *Study of the Two-Jet Angular Distribution*

To the extent that jets can be associated with the outgoing partons in the hard scattering process, the angular distribution of two-jet events provides a direct measurement of the angular distribution of parton parton scattering. According to the leading order QCD calculations (see Sect. 2.4.), the most important contributions to the two-jet cross section are due to diagrams with the exchange of a gluon in the t-channel. Characteristic for such a t-channel vector boson exchange is the rapid rise of the cross section with increasing $\cos\theta^*$, where θ^* is the polar scattering angle in the centre of mass system, in analogy to the $1/\sin^4(\theta^*/2)$ behaviour of Rutherford scattering.

The interest in the study of the two-jet angular distribution is twofold: to test the predictions of perturbative QCD with the underlying parton parton scattering picture and to look for possible deviations which would hint to physics beyond the Standard Model, like quark compositeness, technicolor,[87] or to the existence of axigluons.[88]

From the UA2 data events with a clear two-jet structure have been selected by requiring two jet clusters with transverse energies above 40 GeV in the pseudorapidity range $|\eta| < 1.8$ and with an angular separation in the transverse plane of at least 160° (Ref.[89]). Multi-jet configurations have been suppressed by rejecting events with a third reconstructed cluster with a transverse energy in excess of 10 GeV. After a boost to the two-jet centre of mass system the angle θ^* between the two-jet axis and the beam direction, defined according to the convention

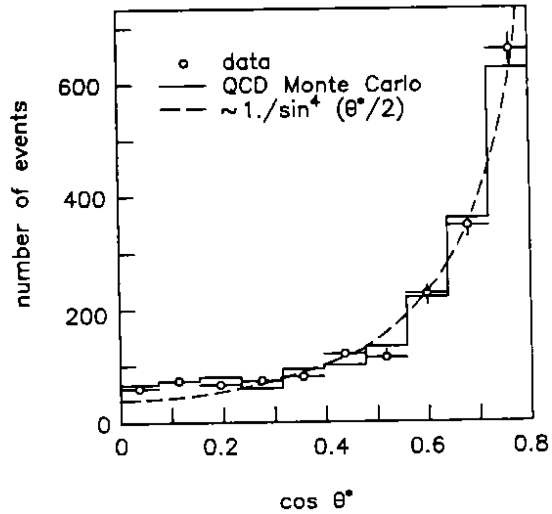

Figure 21. *Distribution of* $\cos\theta^*$ *for two-jet events. The data are compared to the leading order QCD calculation.*[80] *The dotted line represents the* $1/\sin^4(\theta^*/2)$ *behaviour expected for t-channel vector boson exchange.*

of Ref.[90], has been considered. The measured $\cos\theta^*$ distribution for events with a two-jet mass exceeding 200 GeV is shown in Fig. 21. The data are compared with a leading order QCD calculation,[80] where the QCD scale has been chosen to be $\mu^2 = (P^2_{T,1} + P^2_{T,2})$. Detector response effects have been taken into account in the calculation. Good agreement is found between the data and the QCD predictions. In particular, the measured angular distribution is found to be consistent with the form $dn/d\cos\theta^* \sim 1/\sin^4(\theta^*/2)$, represented by the dotted line in Fig. 21. This behaviour supports the prediction of the dominance of t-channel vector boson exchange. The deviations seen at small values of $\cos\theta^*$ are due to s-channel contributions which become important for $\theta^* \sim \pi/2$.[89] This analysis has already been used in the early phase of jet studies at the CERN Collider to rule out models with scalar gluons.[91]

In order to look for possible deviations from the QCD predictions, it is convenient to consider the variable

$$\chi = \frac{1+\cos\theta^*}{1-\cos\theta^*}, \tag{25}$$

which removes the $1/\sin^4(\theta^*/2)$ singularity. In Fig. 22 the data are compared to the leading order QCD calculation, labeled as $\Lambda_C = \infty$, and to the prediction where quarks are assumed to be composite, with preons bound inside the quarks at a characteristic energy scale Λ_C. Such a substructure would give rise to a four-quark contact interaction (see Sect. 6.3.) and would lead to an enhancement of the production of jet pairs in the central region. The UA2 data agree well with the leading order QCD calculation and are clearly in disagreement with composite models with an energy scale in the order of a few hundred GeV.

The sensitivity of the χ-distribution to the choice of the scale μ has also been

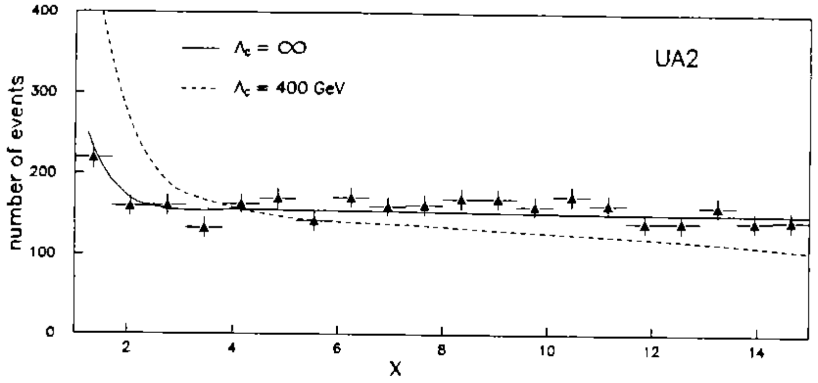

Figure 22. *χ-distribution for two-jet events with two-jet masses exceeding 200 GeV. Superimposed are the leading order QCD prediction[80] (full line) and the prediction where an additional contact interaction is assumed (dashed line, see text).*

studied.[89] Leading order calculations together with scale definitions which do not depend on the scattering angle θ^* do not lead to a satisfactory description of the data. However, good agreement is found for θ^*-dependent definitions like $\mu^2 \sim (E_{T,1}^2 + E_{T,2}^2)$. It should be kept in mind that this sensitivity should be largely reduced once higher order QCD corrections are taken into account.

To conclude, the leading order QCD predictions give a good description of the two-jet angular distribution lending support to the parton parton scattering picture with the dominance of t-channel gluon exchange. The present data give no evidence for deviations from QCD predictions. Similar results have been obtained by the UA1 and CDF Collaborations.[92,93]

5.3. *Study of Three-Jet Events*

Additional gluon radiation from the partons in the elementary parton parton scattering processes results in three-jet topologies in the final state. Leading order tree level calculations ($\mathcal{O}(\alpha_s^3)$) are available[94,95] and can be used for a qualitative comparison between the experimental data and QCD predictions. The soft and collinear divergences, which are inherent in the leading order tree level calculation, can be avoided by requiring a minimal transverse momentum for all outgoing partons and a minimal angular separation between pairs of outgoing partons.

For the comparison between data and theory the following variables have been chosen, some of which are particularly suited to demonstrate the bremsstrahlung nature of the radiated gluons:

- the polar angle Θ^* between the leading jet and the beam direction in the centre of mass system (CMS) of the three jets;

- the angle Ψ^*, which describes the internal configuration of the three-jet system, defined as the angle between the plane spanned by the leading jet and the beam and that of the three jets in their CMS (event plane). Initial state gluon radiation tends to produce a third jet close to the beam axis characterized by $\Psi^* \simeq 0$ and $\Psi^* \simeq \pi$;

- the Ellis-Karliner angle ζ, defined by the relation $\cos\zeta = (P_2^* - P_3^*)/P_1^*$, where P_i^* represents the momentum of jet i in the three-jet CMS. For final state radiation the $\cos\zeta$ distribution is expected to peak at $\cos\zeta = 1$;

- the angle $\omega_{2,3}$ between the second and third jet in the event plane. Also for this angle, final state radiation should lead to a peak at $\cos\omega_{2,3} = 1$.

Three-jet events have been selected from the data by requiring three reconstructed clusters in the calorimeter, the leading one with a transverse energy of at least 60 GeV in the pseudorapidity range $|\eta| < 2$, and the second and third with transverse energies of at least 10 GeV. Any additional clusters must have a transverse energy of less than 10 GeV. Cuts on the cluster radii and on the energy of the underlying event have been applied to eliminate luminosity dependent background.[89]

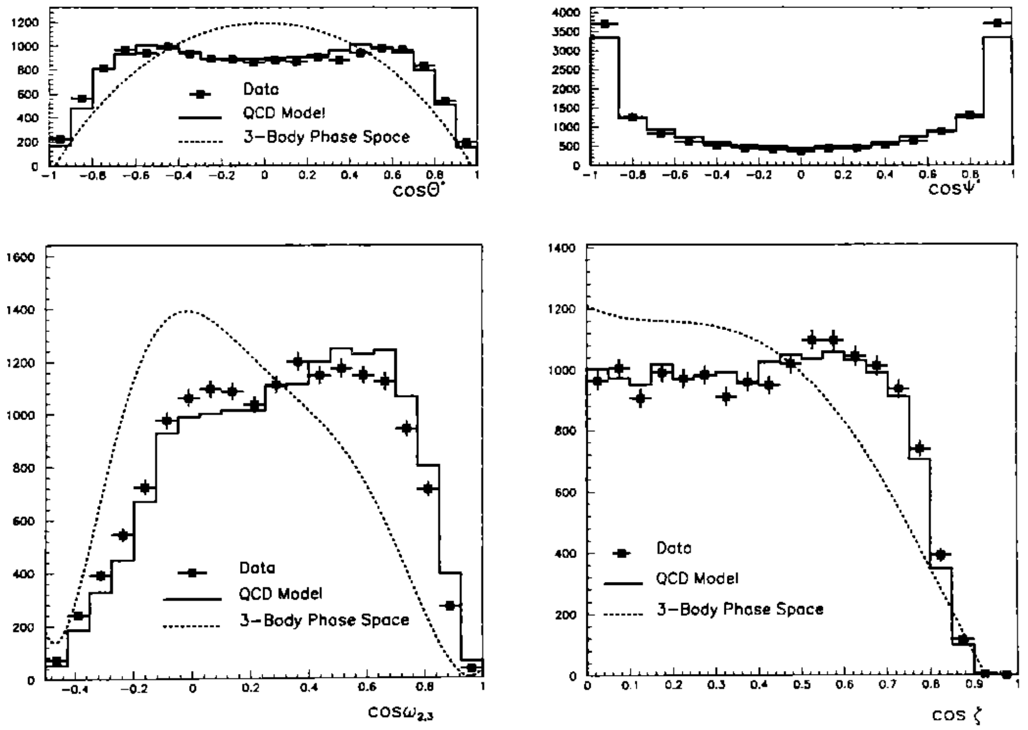

Figure 23. *The distributions of* $\cos\Theta^*$, $\cos\Psi$, $\cos\omega_{2,3}$, *and* $\cos\zeta$ *for three-jet events. The data are compared to the tree level QCD predictions (solid lines) and to the predictions of a three body phase space model (dotted line).*

The comparison between the data and the QCD prediction, which is based on a Monte Carlo calculation using the matrix element calculation of Ref.[95], is shown for the variables introduced above in Fig. 23. For illustration, the shapes of the distributions have also been calculated using a three-body phase space model with all matrix elements $|M|^2$ set to one. The data are found to be consistent with the bremsstrahlung behaviour as predicted by QCD and show clear disagreement with the simple phase space model. There are strong indications for both initial ($\cos\Psi^*$ distribution) and final state ($\cos\zeta$ and $\cos\omega_{2,3}$ distribution) gluon radiation. It should be noted that the expected peaking at $\cos\zeta = 1$ and $\cos\omega_{2,3} = 1$ from final state gluon radiation is suppressed due to the limited angular resolution between jets and due to the admixture of events resulting from inital state radiation.

5.4. Multi-Jet Final States

The tree level calculations have been extended to include the complete contributions up to order α_s^4 (Ref.[94]) and α_s^5 (Ref.[95]), so that also for multi-jet final states ($n \geq 4$) comparisons between the data and the tree level QCD predictions become possible.

From the available UA2 data sample events have been selected which contain at least four jets with high transverse momenta in the final state. Exclusive n-jet topologies have been defined by requiring that exactly n jets with a transverse energy above a threshold of 15 GeV and no additional jets above 10 GeV are reconstructed. All jets have been required to be contained in the pseudorapidity range $|\eta| < 2.0$. After applying additional, technical cuts[96] to suppress background events, 9947 four-jet, 281 five-jet and 7 six-jet events have been retained in the data sample.

These jet rates as well as the measured distributions of kinematical parameters can be compared to the leading order QCD calculations. For these calculations the parton distributions of Ref.[97] with $\Lambda = 200$ MeV have been used. The QCD scale μ has been defined as the maximum transverse energy of the final state partons. For these choices the leading order predictions of the jet rates are in good agreement with the observed cross sections. After acceptance corrections, the QCD model predicts cross sections of 1.28 nb for four-jet events and 0.040 nb for five-jet events, to be compared with the experimental measurements of 1.31 nb and 0.037 nb, respectively. However, given the large experimental and theoretical uncertainties this agreement is not very significant. Since the absolute QCD n-jet cross sections are proportional to α_s^n, variations of Λ and of the scale μ can easily result in a factor of two difference in the QCD predictions. Furthermore, higher order corrections (K-factors) are completely ignored and the predictions are affected by uncertainties in the jet fragmentation and in the simulation of the interaction of the spectator partons (underlying event).

The observed P_T spectra of four-, five- and six-jets are shown in Fig. 24 together with the leading order calculation of Ref.[95]. Each observed jet contributes one entry to these distributions. Over several orders of magnitude the shapes of these

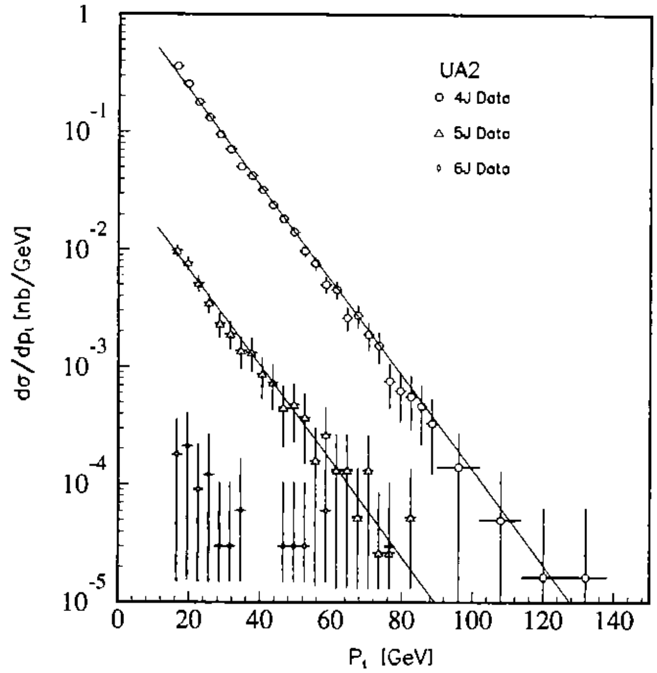

Figure 24. *Measured inclusive P_T spectra for four-, five-, and six-jet events. The overall P_T independent systematic error is not shown, whereas the P_T dependent systematic error has been added quadratically to the statistical error. The solid lines represent the prediction of the leading order QCD calculation of Ref.*[95] *for four- and five-jet events.*

P_T spectra are in impressive agreement with the QCD calculations. This good agreement was also found for the sphericity and invariant mass distributions as well as for the distributions of the space angles between the four jets in the centre of mass system.[96] Similar studies of three- and multi-jet final states have also been performed by the UA1 and CDF Collaborations.[98,99] Like UA2, they also find good agreement between the measurements and the tree level QCD predictions.

5.5. *Search for Multi-Parton Production*

Several authors have suggested an additional mechanism for multi-jet production in hadronic interactions,[100] in which multiple independent hard parton scatterings occur within the same $p\bar{p}$ collision (see Fig. 25). Given the dominance of the two-jet cross section, these multi-parton interactions should most easily be observable in four-jet final states. In a simple model of multi-parton interactions the cross section for double parton scattering (DPS) can be written as[101]

$$\sigma_{DPS} = \frac{1}{2} \cdot \frac{\sigma_2^2}{\sigma_{eff}}, \tag{26}$$

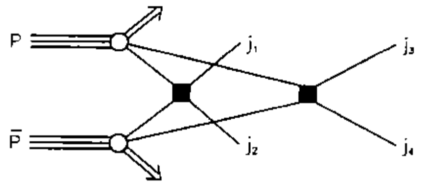

Figure 25. *Schematic representation of double parton scattering.*

where σ_2 is the two-jet cross section and σ_{eff} is interpreted as a scale parameter related to the distance among the partons inside the proton. Theoretical speculations suggest σ_{eff} to be smaller than the total inelastic hadronic cross section, measured to be ~ 40 mb at $\sqrt{s} = 630$ GeV.[102]

A search for an admixture of such a double parton scattering contribution in the four-jet sample has been carried out.[96] The good description of the four-jet data in terms of standard QCD processes, which are dominated by double bremsstrahlung, indicates that very little room is left for other multi-jet production mechanisms. Given the substantial similarities between DPS and QCD bremsstrahlung events, the search for a DPS contribution has been performed on a statistical basis. In contrast to QCD production, the events resulting from double parton scattering are expected to have jet pairs which are approximately balanced in transverse momentum and are produced at opposite azimuthal angles. The value of the variable

$$S^2 = \frac{1}{2}\, min \left(\frac{\left|\vec{P}_T^i + \vec{P}_T^j\right|^2}{\left|\vec{P}_T^i\right| + \left|\vec{P}_T^j\right|} + \frac{\left|\vec{P}_T^k + \vec{P}_T^l\right|^2}{\left|\vec{P}_T^k\right| + \left|\vec{P}_T^l\right|} \right), \qquad (27)$$

where the minimization is performed over the three possible permutations of the jet pairs, is expected to be close to zero for double parton scattering events. Gluon radiation, wrong jet assignment, and experimental resolution effects, however, result in an S-distribution that is smeared and slightly shifted with respect to the naive expectation. The log(S) distributions are shown in Fig. 26a for the data, for QCD double bremsstrahlung events, and for double parton scattering events, generated by a modified version of the Pythia Monte Carlo program.[96]

In order to determine the DPS contribution, the four-jet data sample is assumed to be an unknown mixture of the two event classes and a χ^2-minimization for the log(S) distribution is performed. The best fit (see Fig. 26b) is obtained for a DPS contribution corresponding to a cross section of $\sigma_{DPS} = 0.49 \pm 0.20$ nb, implying $\sigma_{DPS} < 0.82$ nb at the 95% confidence level. Given the absence of an unbambiguous signal, the UA2 Collaboration prefers to translate this result into a lower bound of the effective cross section,

$$\sigma_{eff} > 8.3\ mb \qquad\qquad at\ 95\%\ C.L.$$

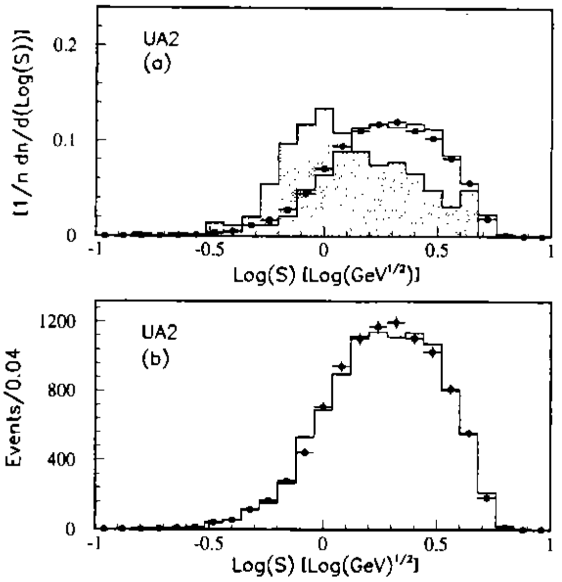

Figure 26. *a)* $\log(S)$ *distribution for the four-jet data (points), double parton scattering events (hatched histogram) and QCD double bremsstrahlung events (solid histogram). The contents of all histograms have been normalized to one. b) Comparison of the best fit (solid histogram) to the distribution measured for the data.*

This result can be compared to the results of other experiments. The AFS Collaboration reported evidence for double parton scattering from a study of multi-jet events at the CERN ISR with $\sigma_{eff} = 5$ mb.[103] This result is not necessarily in contradiction to the UA2 result, since the x-range probed by the multi-jet configurations at the two centre of mass energies of 63 and 630 GeV is very different. Recently, the CDF Collaboration reported a DPS signal with a significance of 2.5 standard deviations,[104] corresponding to $\sigma_{eff} = 12.1^{+10.7}_{-5.4}$ mb, which is consistent with the UA2 result.

5.6. Direct Photon Production

The direct production of isolated, high transverse momentum photons allows for a more quantitative test of perturbative QCD. Since the measurement of the photon transverse momentum is not affected by fragmentation effects, the experimental uncertainties are considerably smaller than those obtained in the measurements of jet cross sections. On the theoretical side, next to leading order calculations are available for both single and double direct photon production[105,106] and can be directly compared to the experimental results.

5.6.1. *Single Photon Cross Section*

The direct production of high P_T photons from hadron hadron collisions is described in Born approximation by $q\overline{q}$ annihilation ($q\overline{q} \rightarrow g\gamma$) and by the QCD Compton process $gq \rightarrow q\gamma$ (see Fig. 27). In addition, photons can be produced from final state radiation in any hard scattering process involving quarks in the final state. This contribution can, however, be experimentally suppressed by applying isolation criteria to the photon candidate. Such requirements suppress at the same time the overwhelming background from π^0 or η mesons produced in jets and decaying to unresolved photon pairs.

Figure 27. *Leading order contributions to direct photon production.*

The UA2 Collaboration has measured the inclusive direct photon production cross section in the central rapidity region, $|\eta| < 0.76$ (Ref.[107]). A photon candidate has been defined as an electromagnetic cluster satisfying the following criteria:[107]

- the lateral and longitudinal profiles of the cluster have to be consistent with those expected from a single isolated electron or photon;

- there must be no charged tracks pointing to the calorimeter cluster. This requirement is validated by the absence of any pad signals in either silicon counter contained within a window of $\Delta\eta < 0.2$ and $\Delta\phi < 15°$ about the cluster axis;

- there must be at most one preshower signal in a cone defined by $\sqrt{\Delta\phi^2 + \Delta\eta^2} < 0.265$ about the cluster axis.

The last requirement keeps both photons which undergo conversions in the converter plate of the preshower detector and unconverted photons. The preshower detector plays a key role in the estimate of the π^0 and η background in the photon sample. This background contamination has been determined on a statistical basis by considering the fraction of photons in the sample that initiate a shower in the converter and comparing this fraction to the expectations of the conversion probabilities for isolated photons and π^0's.[107]

The invariant inclusive cross section $Ed\sigma/d^3p$ is shown in Fig. 28 as a function of the photon transverse momentum P_T. The errors shown correspond to the combined statistical and P_T dependent systematic errors, which mainly result from uncertainties in the photon efficiency calculation and from uncertainties in the evaluation of the conversion probabilities by using the EGS Monte Carlo.[108] On top of the errors shown there is an additional P_T independent uncertainty of ±9%.

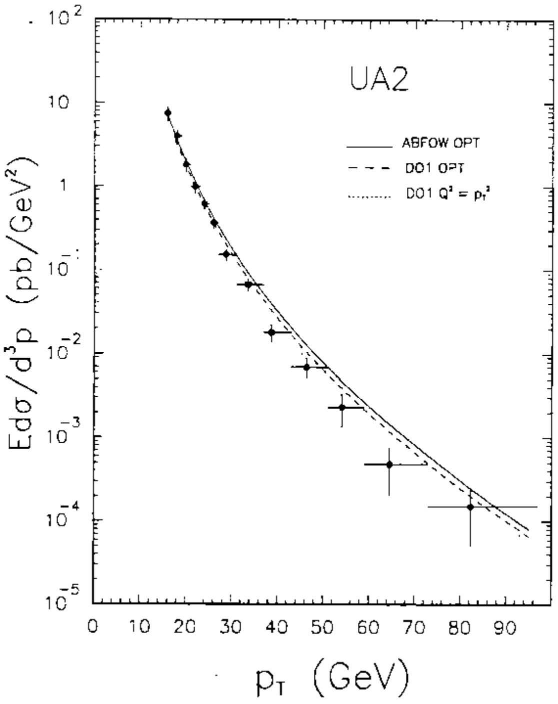

Figure 28. *The invariant differential cross section for direct photon production is compared with the next to leading order QCD calculation of Ref.*[105] *with different choices for the structure functions and QCD scales. For the structure functions the parametrizations of Ref.*[109] *(ABFOW) and of Ref.*[97] *(DO1) have been used. For the QCD scale either P_T or an optimized scale, as discussed in Ref.*[105], *have been chosen.*

The results are compared to next to leading order QCD calculations,[105] where different sets of structure functions and different choices of the renormalization scale have been used. The isolation cut, which suppresses the bremsstrahlung contribution from final state quarks, is taken into account in the QCD calculation (see Ref.[105] for a description of the correct procedure). Within the experimental and theoretical uncertainties the data are in agreement with the QCD predictions. However, in the low P_T region (P_T < 30 GeV) the measured P_T dependence is significantly steeper than the one predicted by QCD. Such an effect has also been observed recently by the CDF Collaboration at $\sqrt{s} = 1.8$ TeV.[110] It could result from the quark bremsstrahlung contribution, which is expected to be more important at low P_T. A more accurate theoretical estimate of this contribution is needed for a better quantitative comparison.

5.6.2. *Double Photon Production*

The production of events with two high P_T photons in the final state needs to be studied as a serious source of background to the detection of an intermediate mass Higgs boson at future hadron colliders.[111] The capability of QCD to properly predict the $\gamma\gamma$ production cross section is therefore an important fact to verify experimentally.

In leading order, two basic processes contribute to the production of photon pairs, the $q\bar{q}$ annihilation ($q\bar{q} \rightarrow \gamma\gamma$) and the gluon fusion via a quark box ($gg \rightarrow \gamma\gamma$), as shown in Fig. 29. In addition, various bremsstrahlung diagrams contribute to the production of two photons in the final state.

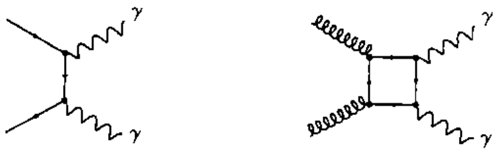

Figure 29. *Lowest order diagrams for double photon production.*

From the UA2 data events have been selected with two photons in the central calorimeter ($|\eta| < 0.76$) with transverse momenta $P_T(\gamma_1) > 10$ GeV and $P_T(\gamma_2) > 9$ GeV. The background from jet production and bremsstrahlung can be strongly reduced by applying the condition

$$\vec{P}_T(\gamma_1) \cdot \vec{P}_T(\gamma_2) < -0.7 \cdot \left| \vec{P}_T(\gamma_1)^2 \right| ,$$

by which events with a large imbalance between the transverse momenta of the two photon candidates are rejected.[107] After the subtraction of the background from two-jet events and single photon events, a signal of 58 ± 13.4 events has been found in the data. The inclusive cross section $d\sigma/dP_T$ is shown in Fig. 30 with statistical and P_T dependent systematic errors. In addition, there is a normalization uncertainty of $\pm 6.8\%$. Two independent next to leading order QCD predictions[106,112] are superimposed. In both calculations the structure function parametrizations of Ref.[24] and the scale $\mu = P_T$ are used. Both predictions agree well with the data, apart from deviations seen in the first P_T bin, where the data lie significantly above the theoretical prediction. Again, this discrepancy could be due to the theoretical uncertainties in the calculation of final state quark bremsstrahlung, which contributes mostly at low P_T.

Also the CDF Collaboration has performed a measurement of the double photon production cross section.[113] Although their measured values lie systematically above the QCD predictions, there is still agreement within the errors.

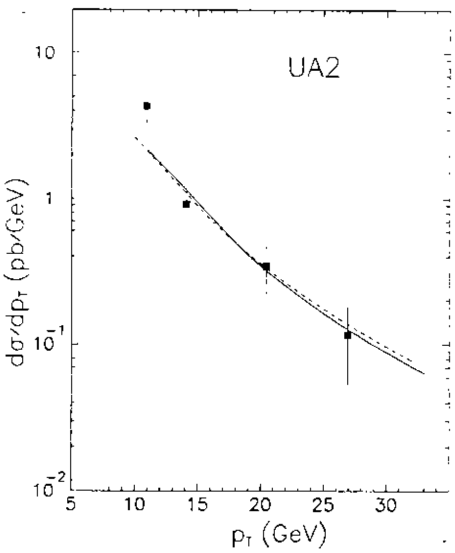

Figure 30. *Differential cross section $d\sigma/dP_T$ for double photon production. The superimposed curves are next to leading order QCD predictions of Ref.*[112] *(dashed line) and Ref.*[106] *(full line).*

5.7. Measurement of the W and Z Production Cross Sections

As discussed in Sect. 2.4., the QCD predictions for the W and Z production cross sections are known up to second order in α_s. Thus, the comparison between data and the theoretical predictions provides an important test beyond the next to leading order.

The vector boson production cross section times the branching ratio to electrons is given by

$$\sigma_V^e = \frac{N_V^e - N_{back}}{\epsilon\ \eta\ \mathcal{L}}(1 - f_{\gamma^*}), \tag{28}$$

where N_V^e is the number of vector boson candidates observed in the electron channel, N_{back} the estimated background, η the geometrical acceptance, ϵ the electron reconstruction efficiency, and $\mathcal{L}$ the integrated luminosity. The correction factor $(1 - f_{\gamma^*})$ is only relevant for $Z \to ee$ decays. The constant f_{γ^*} compensates for the contribution from single photon exchange and $\gamma^* Z$ interference and has been evaluated to be 1.65%. The radiative decays $W \to e\nu\gamma$ and $Z \to ee\gamma$ have been taken into account in the acceptance calculations.

In the UA2 analysis,[44] the event numbers, efficiencies and acceptance values have been determined in the three different acceptance regions of the UA2 detector. Cross section values have been determined separately in each detector region. Since the various cross section values have been found to be consistent among each other, they have been combined with weights proportional to the product of acceptance and efficiency. The final results are:

$$\begin{array}{rcrlrll}
\sigma_W^e & = & 682 \pm & 12\,(stat) \pm & 40\,(syst) & pb, \\
\sigma_Z^e & = & 65.6 \pm & 4.0\,(stat) \pm & 3.8\,(syst) & pb.
\end{array}$$

The experimental systematic errors are dominated by uncertainties on the integrated luminosity and uncertainties on the acceptance calculation resulting from uncertainties in the structure functions. The measured cross section values are slightly larger than those published previously,[114,115] but are consistent within the statistical and systematic errors.

In Fig. 31 the results are compared with the theoretical predictions of Ref.[23]. The theoretical values have been multiplied by the corresponding electronic branching ratios, which have been computed in the framework of the Standard Model as a function of the top quark mass. The measurements agree well with the QCD predictions including second order corrections and assuming a heavy top quark. The dependence of the theoretical predictions on the structure functions is represented by the shaded band at the right hand side of the figure.[116] The size of these uncertainties is comparable with the experimental errors and also with the size of the second order QCD corrections.

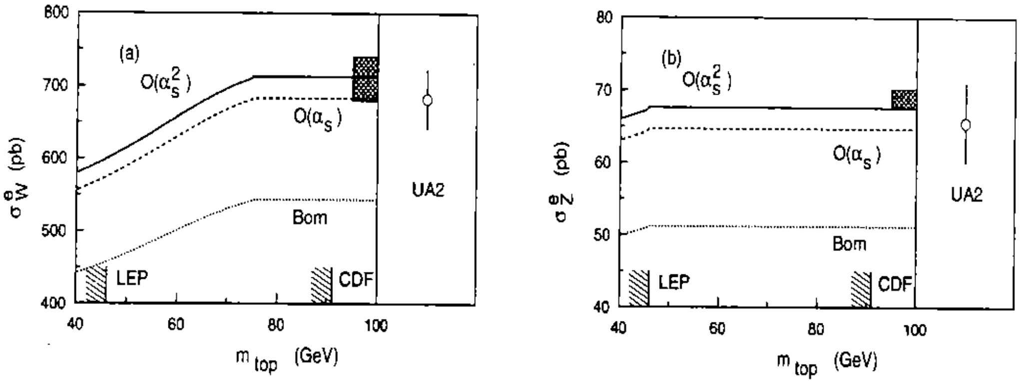

Figure 31. *Comparison between the measured cross section values σ_W^e (a) and σ_Z^e (b) and the QCD predictions[23] as a function of the top quark mass at the Born level and including $\mathcal{O}(\alpha_s)$ and $\mathcal{O}(\alpha_s^2)$ corrections. The shaded bands at the right show the variation with structure functions. The top mass limits from LEP and CDF (1990) are indicated on the abscissae.*

5.8. *Measurement of the Drell-Yan Production Cross Section*

The comparison between the second order QCD prediction and the experimental measurements can also be performed for electron pairs with masses below the Z mass (see Fig. 8). They result from Drell-Yan pair production via the exchange of a virtual photon or a virtual Z. The measured differential cross section $d\sigma/dm$, based on data corresponding to an integrated luminosity of 7.1 pb^{-1}, is shown in

Fig. 32 as a function of the electron pair mass in the range between 10 and 70 GeV. The theoretical predictions are shown for three perturbative orders. The data agree well with the $\mathcal{O}(\alpha_s^2)$ calculation, however, because of the statistical and systematic errors, this comparision is not sensitive to higher order corrections. The integrated electron pair production cross section in the mass range between 10 and 70 GeV has been measured to be $\sigma_{DY} = 405 \pm 51\ (stat) \pm 84\ (syst)$ pb.

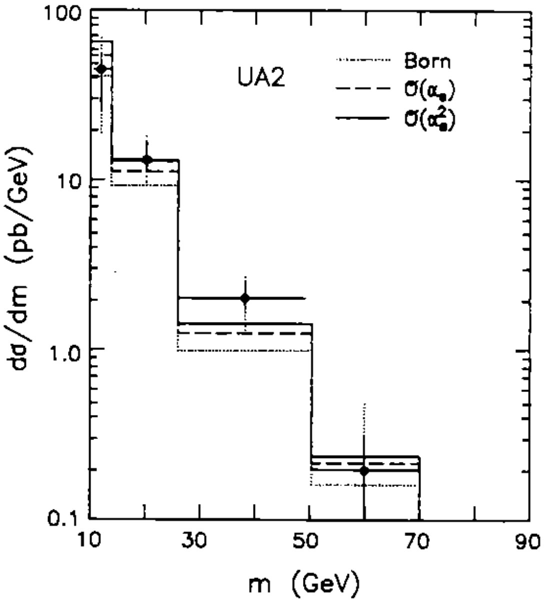

Figure 32. *Comparison between the measured differential cross section dσ/dm for electron pairs and the QCD predictions of Ref.*[23].

5.9. *Measurement of the Strong Coupling Constant α_s*

As discussed previously, strong interaction effects in W production lead to the associated production of W bosons and hadron jets. The dependence of the rate of W+jet events on the strong coupling constant α_s can be used to measure its value in hadronic collisions. For this measurement the UA2 Collaboration has considered the ratio R of the number of W+one-jet to W+zero-jet events. The value of α_s has been extracted from a comparision of the experimental value R_{EXP} to the value R_{MC} predicted by QCD calculations.

For the determination of R_{EXP} the standard UA2 $W \to e\nu$ selection criteria have been applied. Jets in W events have been identified by using the cone algorithm with a radius $R_{cone} = 0.7$. To reduce the systematic uncertainties in the jet energy measurement and to reduce the number of jets arising from the interaction of the spectator partons, only jets with transverse energies exceeding 20 GeV and within the pseudorapidity range $|\eta| < 1.6$ have been retained. Using these cuts, 114 events with one jet and 2845 events with no jets have been found in the data. After correcting for background the experimental ratio has been found to be $R_{EXP} =$

$3.91 \pm 0.40\%$.

The QCD prediction R_{MC} is based on the tree level calculation of W production up to order α_s^2, which is available in form of a Monte Carlo program.[120] The infrared and collinear divergences, which show up in the higher order tree diagrams, are regularized by applying cutoffs on the transverse momenta (P_T) and on the angular separation ω of the outgoing partons,

$$P_T > P_T^{min}, \qquad \omega > \omega^{min}. \tag{29}$$

The tree level simulation represents only a partial calculation of the total W production cross section, because loop diagrams and tree diagrams with outgoing partons, which do not fulfil the conditions defined in Eq. (29), are not taken into account. The size of these missing contributions is given by multiplicative corrections, called K-factors, so that the total cross section to second order in α_s can be written as

$$\sigma^{[2]} = \sigma_0 K_0 + \sigma_1 K_1 + \sigma_2, \tag{30}$$

where the σ_i's are the tree level cross sections. For a complete QCD prediction of the W + jet rates these K-factors must be known. Details on the calculation of these factors can be found in Ref.[121], only the main ideas will be given here.

The calculation of K_1 is based on the calculation of the P_T^W distribution to order α_s^2 from Ref.[25]. For P_T^W values above P_T^{min} a function $K_1(P_T^W)$ can be defined from the relation

$$\frac{d\sigma^{[2]}}{dP_T^W} \;=\; \frac{d\sigma_1}{dP_T^W} K_1(P_T^W) + \frac{d\sigma_2}{dP_T^W} \qquad for \quad P_T^W > P_T^{min}, \tag{31}$$

where the term on the left hand side corresponds to the total inclusive P_T^W spectrum and the differential cross sections on the right hand side are obtained from the tree level Monte Carlo calculations. The tree level cross sections and $d\sigma^{[2]}/dP_T^W$ have been computed in the $\overline{MS}$ renormalization scheme, using $\mu = M_W$ as the scale. To derive a value for the strong coupling constant used in the matrix element calculation, the four flavour value of the QCD scale parameter Λ as given by the structure function parametrization has been converted to the corresponding five flavour value. The functional form of α_s given in Eq. (13) has been used to relate α_s and $\Lambda_{\overline{MS}}$. The results of the K-factor calculation are shown in Fig. 33b for three different P_T^{min} values (6.0, 12.0 and 18.0 GeV). The angular cutoff ω^{min} has been fixed at 20°.

The calculation of K_0 is based on the calculation of the total K-factor to second order, $K_{tot}^{[2]}$, and uses in addition the results for K_1. From the definition of the total K-factor (see Sect. 2.4.) and Eq. (30) the relation

$$K_0 \;=\; K_{tot}^{[2]} - \frac{1}{\sigma_0} \int_{P_T^{min}}^{\infty} \left(\frac{d\sigma_1}{dP_T^W} K_1(P_T^W)\right) dP_T^W - \frac{\sigma_2}{\sigma_0} \tag{32}$$

can be deduced. The results of the calculation of K_0 are shown as a function of P_T^{min} in Fig. 33a.

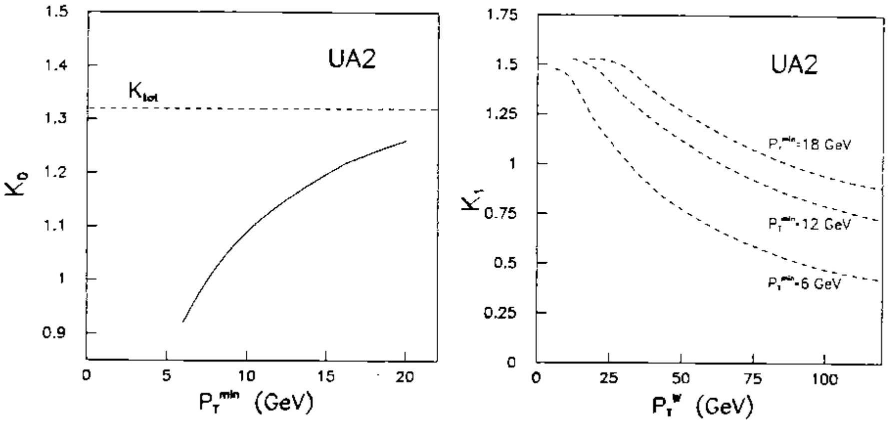

Figure 33. *(a)* K_0 *as a function of* P_T^{min}*; the value of the second order total K-factor is indicated by the dashed line. (b)* K_1 *as a function of* P_T^W *for different* P_T^{min} *values.*

By using these K-factors in conjunction with the tree level Monte Carlo calculations, a second order prediction of R_{MC} can be extracted. By choosing a specific parametrization of the structure functions, R_{MC} can be computed for one value of α_s, which corresponds to the Λ value used in the parametrization. However, for the determination of α_s from the data, the functional dependence of R_{MC} on α_s needs to be known in order to solve the equation $R_{MC}(\alpha_s) = R_{EXP}$. This dependence has been determined by using parametrizations which were obtained from the same deep inelastic scattering data but assuming different Λ values.[122] By using HMRSB-type[24] parametrizations with $\Lambda^{(4)}$ values of 100, 190 and 300 MeV, the R_{MC} values were found to be 3.39%, 3.61% and 3.81%, respectively. The dependence of R_{MC} on α_s is well approximated by a linear function, leading by extrapolation to the result

$$\alpha_s(M_W^2) \;=\; 0.123 \pm 0.018\ (stat.) \pm 0.017\ (syst.).$$

The dominant contributions to the systematic error result from uncertainties in the jet fragmentation and in the simulation of the underlying event.

The present result is in agreement with recent determinations of α_s in e^+e^- and deep inelastic scattering experiments.[123] Although the precision obtained at these experiments cannot be reached, the present analysis provides an independent measurement of the strong coupling constant in a hadronic collision experiment from a process in which α_s is determined from gluon radiation in the initial state. Another measurement of α_s in $p\bar{p}$ collisions has recently been presented by the UA1 Collaboration.[124] They measure α_s from b-quark production and obtain the result $\alpha_s(M_Z^2) = 0.108^{+0.015}_{-0.014}$, which is consistent with the present measurement.

6. Search for New Particles

6.1. Search for Supersymmetric Particles

Some basic problems of the Standard Model can be solved in an elegant way by introducing supersymmetry.[125] This theory, associating to each particle in the Standard Model a so called 'superpartner' (sparticle), predicts a rich spectrum of new particles. To each superpartner a multiplicative quantum number, the R-parity, is assigned, which is absolutely conserved. This implies that sparticles should all decay to the lightest supersymmetric particle, assumed to be electrically neutral, which should in turn escape detection.

6.1.1. Squarks and Gluinos

The supersymmetric partners of quarks and gluons, squarks ($\tilde{q}$) and gluinos ($\tilde{g}$), are expected to be abundantly produced in $p\bar{p}$ collisions via standard QCD processes leading to the pair production of $\tilde{q}\bar{\tilde{q}}$, $\tilde{q}\tilde{g}$ and $\tilde{g}\tilde{g}$.[126] In many models it is assumed that the $\tilde{g}$ decays mainly into $q\bar{q}\tilde{\gamma}$ and the $\tilde{q}$ decays dominantly into $q\tilde{g}$ (if $m_{\tilde{q}} > m_{\tilde{g}}$) or $q\tilde{\gamma}$ (if $m_{\tilde{q}} < m_{\tilde{g}}$), with the photino ($\tilde{\gamma}$) being the lightest supersymmetric particle (LSP).[127] In this case, the hadronic production of squarks and gluinos results in final states containing two to six jets and missing transverse momentum ($\not{p}_T$) due to the undetected photinos.

The UA2 data collected in the years 1988 and 1989 have been searched for an excess of events of this type above the expectations from conventional processes. Events have been selected by requiring at least two hadronic jets ($E_T^1 > 25$ GeV, $E_T^2 > 15$ GeV, $|\eta| < 0.85$) and missing transverse momentum above 20 GeV. The background resulting from two- or multi-jet events for which $\not{p}_T$ is generated by a bad measurement of the transverse energy of one of the jets has been suppressed by cuts on the azimuthal separation between the missing transverse momentum vector and each jet in the event ($\not{p}_T$ isolation).[43] The remaining event sample is mainly composed of events where $\not{p}_T$ results from a neutrino from $W \rightarrow e\nu$ decays, where the W is produced in association with jets. The bulk of these events can be rejected by requiring the events to contain no 'electron-like' calorimeter clusters. These cuts are satisfied by 154 events for which the $\not{p}_T$-distribution is shown in Fig. 34a (shaded histogram). For comparison, the data are also shown before the $\not{p}_T$ isolation and the electron rejection requirements were applied. In the final sample no events with $\not{p}_T > 40$ GeV are found, in agreement with the expectations of less than one event from conventional processes. The observation of no event with $\not{p}_T > 40$ GeV corresponds to an upper limit of 0.35 pb (90% C.L.) on the observed cross section.

The data have been compared to a supersymmetric model implemented in the form of a Monte Carlo generator based on the cross sections given in Ref.[126]. Five squark flavours degenerate in mass have been assumed, with each squark decaying with 100% branching ratio into $q\tilde{\gamma}$ or into $q\tilde{g}$. The gluinos again have been assumed to decay to 100% into $q\bar{q}\tilde{\gamma}$. The comparison of the measured cross section limit with the expected cross sections as a function of $m_{\tilde{q}}$ and $m_{\tilde{g}}$ excludes a region in

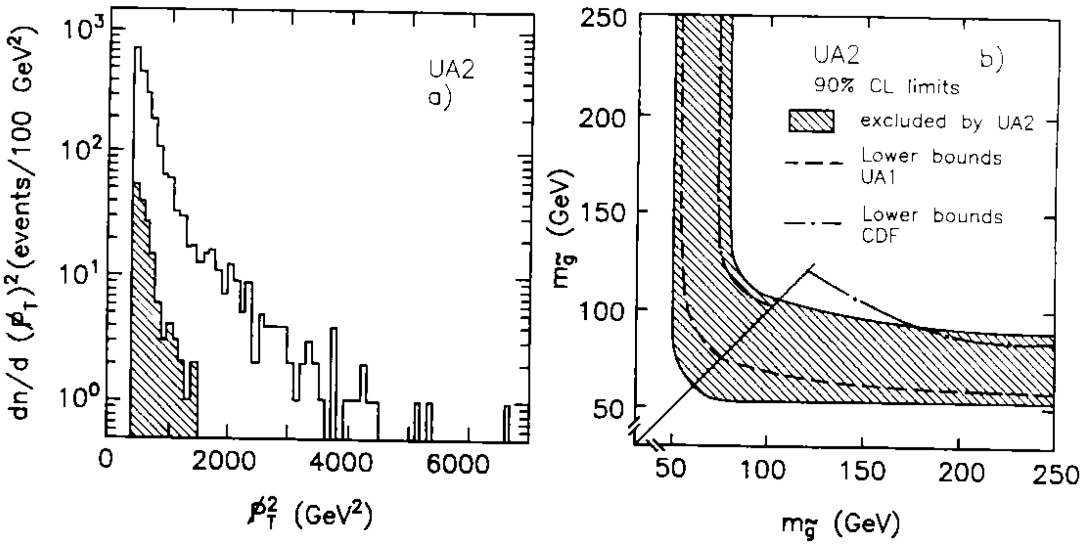

Figure 34. *(a) Distribution of* p_T^2 *for the multi-jet data before and after (shaded histogram)* p_T*-isolation is applied. (b) Excluded mass regions in the* $m_{\tilde q} - m_{\tilde g}$ *plane. The dashed curves indicate the previous mass limits from UA1*[128] *and the dash-dotted curve the one from CDF.*[129]

the $m_{\tilde q} - m_{\tilde g}$ plane, as shown in Fig. 34b. To take into account the systematic uncertainties in the calculation of the expected cross sections, their values have been reduced by their systematic errors. Also shown in the figure are previous results from the UA1[128] and CDF[129] Collaborations. The mass limits obtained are independent of the LSP mass up to 20 GeV, whereas they strongly depend on the assumption of squarks and gluinos decaying directly to the LSP with 100% branching ratio. More complex decay scenarios, as the ones discussed in Ref.[127], would give a softer p_T spectrum resulting in lower mass limits. An analysis based on these models has recently been published by the CDF Collaboration.[130]

In conclusion, under the assumptions stated above, the following mass limits have been obtained at the 90% confidence level:

$$\begin{array}{lll} m_{\tilde q} & > 74\ GeV & \quad independent\ of\ m_{\tilde g}, \\ m_{\tilde g} & > 79\ GeV & \quad independent\ of\ m_{\tilde q}, \\ m_{\tilde q,\tilde g} & > 106\ GeV & \quad for\ m_{\tilde q} = m_{\tilde g}. \end{array}$$

Masses below about 50 GeV are not excluded by this analysis. Under the same assumptions, the CDF experiment excludes at the 90% confidence level the existence of squarks and gluinos with masses less than 126 GeV and 141 GeV, respectively.[130] Squark masses below 45 GeV are excluded by data from LEP.[131]

6.1.2. *Selectrons and Winos*

Scalar electrons ($\tilde{e}$) and winos ($\tilde{W}$), partners of electrons and W bosons in supersymmetric models,[125] can be produced in hadron colliders through the decays of intermediate vector bosons. In the UA2 data a search for exotic decays of the Z boson into final states containing electron pairs has been carried out to look for a possible signal of

$$\begin{aligned} Z &\rightarrow \tilde{e}\tilde{e} \rightarrow ee\tilde{\gamma}\tilde{\gamma} \qquad\qquad \textit{and} \\ Z &\rightarrow \tilde{W}\tilde{W} \rightarrow ee\tilde{\nu}\tilde{\nu}. \end{aligned}$$

Decays of the selectrons into electrons and photinos ($\tilde{e} \rightarrow e + \tilde{\gamma}$) and of the winos into electrons and the supersymmetric partners of the neutrino ($\tilde{\nu}$) have been assumed. The supersymmetric partners of the left-handed and right-handed electron are assumed to be degenerate in mass. For both processes, the final state contains an electron pair in association with missing transverse momentum. The Standard Model background results from the Drell-Yan production of electron pairs and from QCD jet production, where jets are misidentified as electrons.

In order to derive limits on the $\tilde{e}$ and $\tilde{W}$ mass values, the sample of electron pairs with invariant masses above 20 GeV has been compared to the predictions of a model, where contributions from either process $Z \rightarrow \tilde{e}\tilde{e}$ or $Z \rightarrow \tilde{W}\tilde{W}$ have been considered. In addition, the expected background contributions have been included.[132] A maximum likelihood analysis has been performed using as input the electron pair masses and transverse momenta as well as the missing transverse momenta.[132]

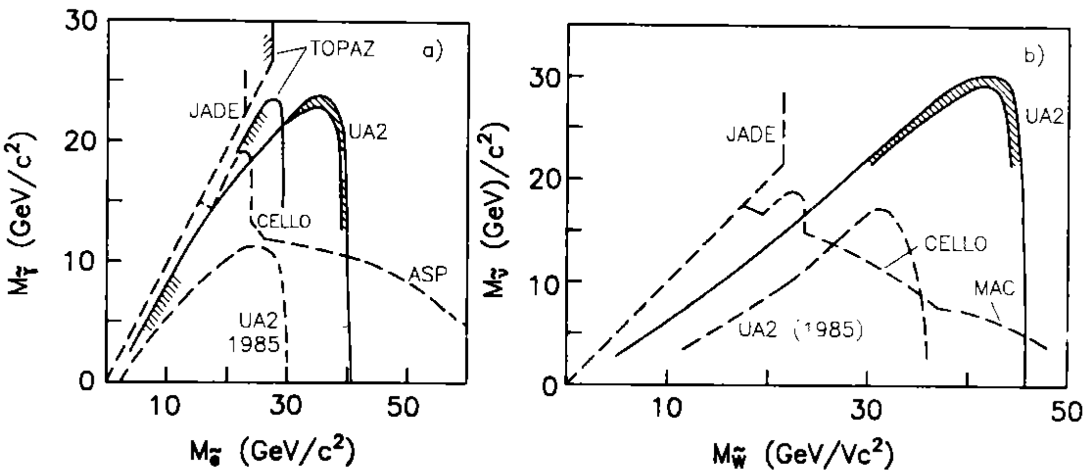

Figure 35. *a) Excluded regions at 90% confidence level in the $m_{\tilde{e}} - m_{\tilde{\gamma}}$ plane. The dashed area indicates the effect of systematic uncertainties. b) same as a) in the $m_{\tilde{W}} - m_{\tilde{\nu}}$ plane.*

No evidence for a signal from supersymmetric particles has been found. The regions in the ($m_{\tilde{e}}$, $m_{\tilde{\gamma}}$) and ($m_{\tilde{W}}$, $m_{\tilde{\nu}}$) planes excluded at the 90% confidence level are shown in Fig. 35. Scalar electrons with masses up to 40 GeV are excluded in the case of a light photino. Similarly, within the assumptions given above, winos lighter than 45 GeV are excluded in the case of a light scalar neutrino.

Searches for these particles have also been performed by the LEP experiments.[133] From the Z invisible width measurement, a lower limit of 41 GeV has been set on the mass of scalar neutrinos. If the mass of the LSP is below 40 GeV, the masses of the supersymmetric partners of the charged leptons must exceed 45 GeV.

6.2. Search for the Charged Higgs

The Higgs sector in the Standard Model consists of a single doublet of complex scalar fields. The simplest extensions beyond this minimal version are models with two doublets of complex scalar fields, which imply the existence of charged Higgs bosons $H^{\pm}$.[134] In such models, the couplings of the Higgs bosons are fully specified by their mass, m_{H^+}, and by the ratio of the vacuum expectation values of the neutral members of the two scalar fields, $\tan\beta = v_2/v_1$.

As already mentioned, the existence of $H^{\pm}$ bosons could have important implications for the search of the top quark. In the case $m_t > m_{H^+} + m_b$ the decay $t \rightarrow H^+ b$ competes with the standard decay $t \rightarrow W^+ b$, with branching ratios depending on m_{H^+} and $\tan\beta$.[15] The charged Higgs itself decays predominatly into $\tau^+\nu$ and $c\overline{s}$ pairs, with branchings depending on $\tan\beta$.[135] Hence the semileptonic decay $t \rightarrow be\nu$ is largely suppressed compared to the Standard Model expectations. In particular, for the mass range accessible at the CERN $p\overline{p}$ Collider, $m_W > m_t + m_b$, the decay $t \rightarrow H^+ b$ dominates, regardless of the value of $\tan\beta$.[136]

Using the total data sample, the UA2 Collaboration has searched for the decay chain[137]

$$t \rightarrow H^+ b, \qquad H^+ \rightarrow \tau^+ \nu_\tau, \qquad \tau^+ \rightarrow hadrons + \overline{\nu}_\tau.$$

The analysis method is based upon that used in the measurement of $e-\tau$ universality (see Sect. 4.4.). First, the numbers of electrons and τ's accompanied by large missing transverse momentum have been determined. The number of electrons has then been used together with the assumption of $e-\tau$ universality to determine the number of τ's expected from W decays. This Standard Model prediction has been compared to the data. A statistically significant excess of events would indicate new physics, while the agreement between data and expectation would make it possible to exclude the H^+ production in some regions of the noted parameter space.

Table 8. Number of observed and expected $\tau\nu$ events without and with an accompanying jet.

	observed	expected, assuming $e-\tau$ universality	excess
τ + 0 jet	$754 \pm 68 \pm 54$	$760 \pm 31 \pm 25$	$-6 \pm 75 \pm 60$
τ + 1 jet	$73 \pm 24 \pm 5$	$68 \pm 8 \pm 3$	$+5 \pm 25 \pm 6$

The result on $e-\tau$ universality as presented in Sect. 4.4. does not leave much room for an excess of τ events. Table 8 contains the number of expected τ events,

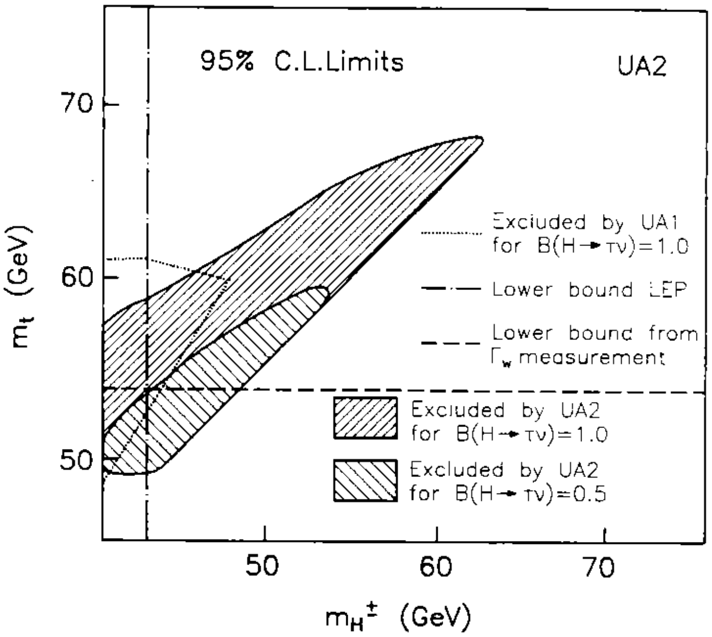

Figure 36. *Regions of the $m_{H^\pm} - m_t$ plane excluded at 95% confidence level.*

based on the assumption of $e - \tau$ universality, in comparison with the number of observed τ events. Since no significant excess of τ-events is found, the data have been used to exclude regions in the parameter space for the H^+ hypothesis.

Charged Higgs events have been generated with the Monte Carlo program of Ref.[80] for 16 different choices of m_{H^+} and m_t values in the ranges $44 < m_{H^+} < 66$ GeV and $50 < m_t < 71.5$ GeV, respectively. The number of events expected for each case has been determined by performing a complete detector simulation and applying the analysis cuts. Systematic uncertainties result from theoretical, Monte Carlo and experimental sources such as luminosity (±6%), top production cross sections, simulation of the underlying event (±20%) and b-quark fragmentation.[137] Levels of confidence for the exclusion of H^+ production have been calculated for two choices of $\tan\beta$ corresponding to branching ratios, $\mathrm{Br}(H^+ \to \tau\nu)$, of 0.5 and 1.0. The regions in the $m_{H^\pm} - m_t$ plane, which can be excluded at the 95% C.L. are shown in Fig. 36.

For comparison, the regions excluded in a previous analysis by the UA1 Collaboration[138] are shown together with model independent lower bounds for m_t from hadron collider measurements of Γ_W (see Sect. 4.3.) and for m_{H^+} from a direct search at LEP.[139]

6.3. *Quark Compositeness*

The proliferation of quark and lepton flavours or the massive nature of the W and Z boson give rise to speculations about a possible composite structure of these particles. In analogy to QCD the fundamental constituents (preons) are assumed to be bound by a new strong (metacolour) interaction, which can be described by a non-abelian and asymptotically free theory. One possible manifestation of quark or lepton compositeness is the existence of a four-fermion contact interaction, having the new strong interaction scale Λ_C. A general framework for decribing such four-fermion contact interactions has been set up in Ref.[140]. Assuming helicity conservation and gauge invariance the Lagrangian for left-handed fermion doublets χ can be written as

$$L_{eff} = \eta \frac{4\pi}{2\Lambda_C^2} (\bar{\chi}\gamma^\mu \chi)(\bar{\chi}\gamma_\mu \chi)$$

with $\eta = \pm 1$ for constructive or destructive interference with the QCD term. Due to such interference effects the existence of quark substructure is already apparent well below the energy scale Λ_C.

The $p\bar{p}$ collider experiments are sensitive to four-quark contact interactions. Their effects may be probed by looking for deviations from the QCD behaviour either in the inclusive jet cross section $d\sigma/dP_T$ or in the two-jet angular distributions (see Sect. 5.2.). Finite values of Λ_C would produce an excess of events at large P_T in the inclusive jet cross section and at $\theta^* \cong \pi/2$ in the two-jet angular distribution. Assuming that the main uncertainties, resulting from experimental systematics and higher order corrections, are P_T independent, the predictions can be normalized in the low P_T region and deviations in the high P_T region can be investigated.

The ratio between the theoretical predictions for various values of Λ_C and the pure QCD calculation to leading order ($\Lambda_C = \infty$) are shown as solid lines in Fig. 37, using $\mu = (P_T/2)$ and the structure function parametrization of Ref.[84]. In the same figure the ratio between the UA2 inclusive jet data and the QCD prediction is represented by the black dots. For each Λ_C value the theoretical calculation has been normalized to the experimental data in the range 69 GeV $< P_T <$ 79 GeV, where the pure QCD prediction is expected to dominate.

From a comparison between the experimental data and the various predictions a limit of $\Lambda_C >$ 825 GeV (95% C.L.) can be extracted for pessimistic assumptions on the experimental systematic uncertainties.[82] In particular, systematic effects which could distort the shape of the cross section, like variations of the scale μ and of the structure functions have been taken into account. This measurement represents a significant improvement over previous limits from the CERN Collider.[83,141] It is also significantly higher than the limit which can be extracted from a study of the angular distribution of two-jet events, $\Lambda_C >$ 415 GeV (95% C.L.).[89] Meanwhile the limit has been superseded by a limit extracted in a similar analysis by the CDF experiment. Their data, corresponding to an integrated luminosity of 4.2 pb^{-1} at $\sqrt{s} = 1.8$ TeV, have allowed limits to be placed of $\Lambda_C >$ 1.4 TeV using the inclusive jet data,[142] and of $\Lambda_C >$ 1.0 TeV using the two-jet angular distribution.[143]

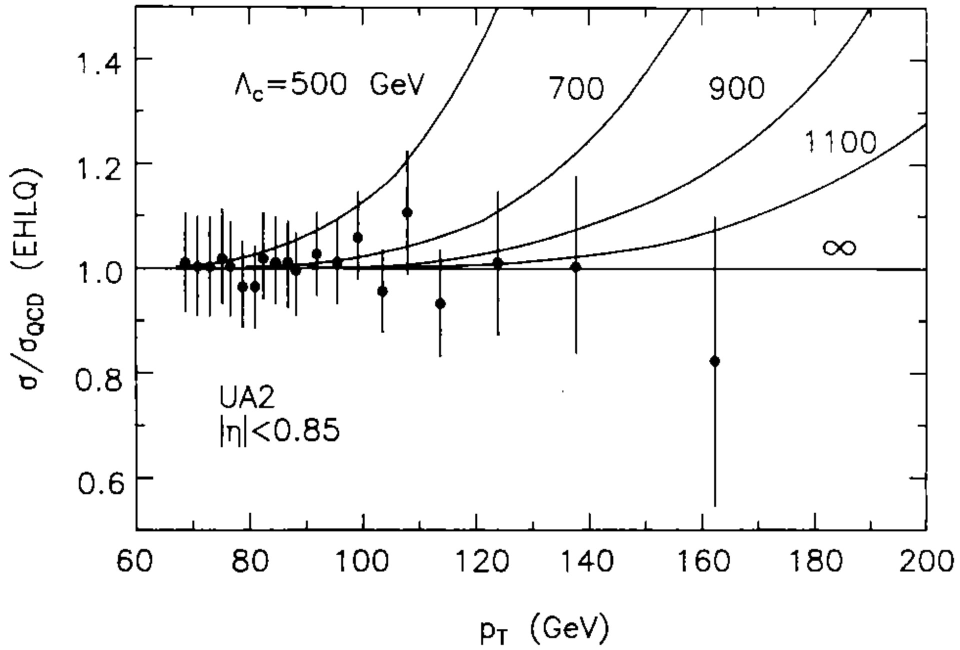

Figure 37. *The ratio between data (black dots) and the QCD calculation. The behaviours predicted for finite values of* Λ_C *are shown as solid curves, again relative to the QCD prediction.*

6.4. Search for Leptoquarks

The symmetry between lepton and quark generations in the Standard Model inspires the hypothesis about the existence of leptoquarks (LQ), strongly interacting particles which couple to lepton-quark combinations. They appear in several theoretical frameworks extending beyond the Standard Model,[144] notably in superstring inspired models, grand unifying models and in some scenarios for compositeness of quarks, leptons, and W and Z bosons. In several of these models,[145] leptoquarks are scalar particles which can have masses m_{LQ} lower than 100 GeV and could therefore be accessible at the CERN $p\bar{p}$ Collider.

In $p\bar{p}$ collisions, the production of single leptoquarks associated with a lepton (l), qg $\longrightarrow$ lLQ, as well as pair production through gg fusion and $q\bar{q}$ annihilation is expected. Single production is proportional to the model-dependent ql-LQ coupling, while in pair production only the contribution from the t-channel $q\bar{q}$ annihilation is affected by this dependence. Pair production is expected to dominate over single production at the CERN $p\bar{p}$ Collider.[146] Since the t-channel contribution in pair production is small, in practice no model dependent assumptions need to be made about the $ql - LQ$ coupling, nor about the leptoquark charge.

The UA2 Collaboration has searched in the total data sample for the pair production of first generation scalar leptoquarks.[148] It has been assumed that each generation has its own leptoquarks and couplings occur only within a given generation in order to satisfy the experimental constraints on flavour changing neutral currents.[147] The first generation of leptoquarks is therefore expected to manifest itself with decays into a light quark (u,d) and an electron with a branching ratio b, or into a light quark and an electron neutrino with a branching ratio $(1 - b)$. The pair production of leptoquarks can therefore lead to three different final states, containing two jets with either an e^+e^--pair, one electron and one neutrino, or two neutrinos. The first two channels have been considered in the UA2 analysis.

The data have been searched for events with two leptons (ee or $e\nu$) accompanied by two jets in the pseudorapidity range $|\eta| < 2.0$. In order to suppress background from multi-jet production, the transverse momenta of the leptons and the jets have been required to exceed the following values: $E_T(e_1) > 18$ GeV, $E_T(e_2) > 9$ GeV and E_T(jet)>10 GeV in the case of two electrons, and $E_T(e) > 20$ GeV, $\not{p}_T > 20$ GeV and $E_T(\text{jet}) > 20$ GeV in the electron neutrino case. In the framework of the Standard Model such events could result from the associated production of vector bosons with two jets. In the total data sample 15 events with the configuration described above have been found, nine electron pair events and six electron neutrino events. The absolute rates and the topology of these events are consistent with the expectations from the QCD calculations of the associated production of W and Z bosons with jets.[148] All electron pair events have invariant electron pair masses in the range $80 < m_{ee} < 100$ GeV as expected for $Z \to ee$ decays. The $e\nu$ events have transverse masses of the electron neutrino system in the range $60 < m_T < 90$ GeV consistent with the W $\to e\nu$ hypothesis. After excluding events with mass values in these regions no candidate leptoquark events remain.

The production and the decay of leptoquarks have been calculated according to the formulae of Ref.[147]. Only the leading order contributions are included in the calculation and higher order QCD contributions, which would lead to an increase of the production cross sections,[149] have been ignored.

Using the estimated cross sections,[150] the number of the observed events and the detector acceptance, lower limits on the leptoquark mass have been evaluated as a function of the branching ratio b. They are shown for both channels separately and for the combination of the two in Fig. 38. If the branching ratio b is assumed to be 0.5, first generation leptoquarks with masses below 67 GeV can be excluded at the 95% confidence level. For branching ratios $b > 0.12$ this analysis improves the limits from LEP experiments,[151] reaching a limit of 74 GeV for $b = 1.0$.

The results on searches for leptoquarks by other $p\bar{p}$ experiments are summarized in Table 9. Mass limits are given for two values of the branching ration b.

Table 9. Mass limits for scalar leptoquarks from $p\bar{p}$ experiments.

Experiment		int. luminosity	lower mass limits (95% C.L.)	
			b = 1.0	b = 0.5
UA2	Ref.[148]	13.0 pb^{-1} (1988-1990)	76 GeV	67 GeV
CDF	Ref.[152]	4.1 pb^{-1} (1988-1989)	113 GeV	80 GeV
D0	Ref.[153]	15.0 pb^{-1} (1992-1993)	133 GeV	120 GeV

The most stringent limit from $p\bar{p}$ experiments comes from a recent analysis of the

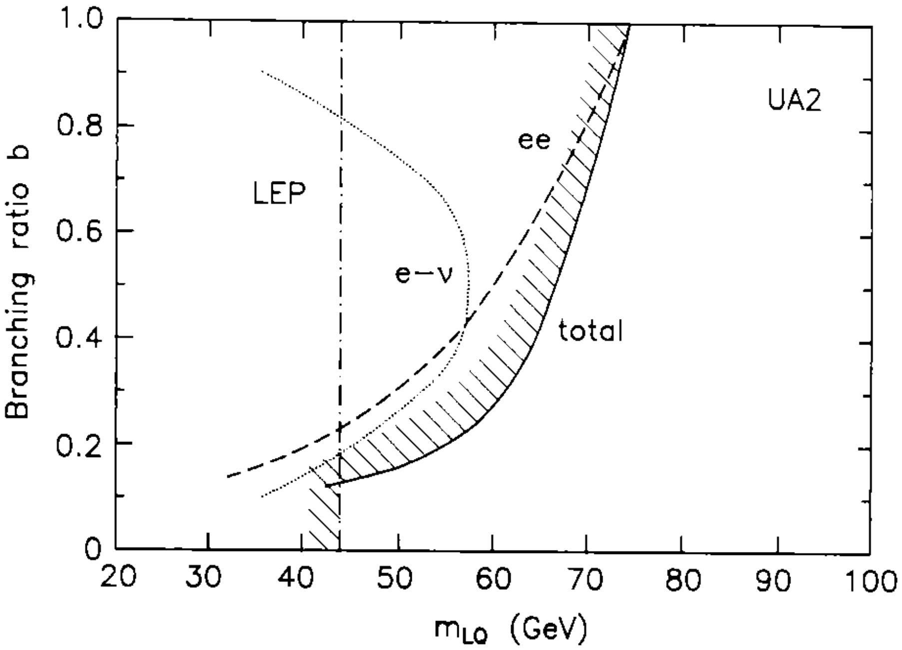

Figure 38. *Leptoquark mass limits at 95% C.L. as a function of the branching ratio b (LQ → eq) for the two electron channel, the electron neutrino channel, and for the combination of both. Also indicated is the limit obtained by the LEP experiments.*[151]

D0 experiment at Fermilab, excluding scalar leptoquarks up to masses of 133 GeV for $b = 1$ and up to 120 GeV for $b = 0.5$. After the successful start of the HERA collider at DESY, leptoquarks have also been searched for in electron proton collisions, where they should show up as a narrow resonance in the s-channel. Here the production depends directly on the coupling λ between the lepton-quark pair and the leptoquark. Assuming this coupling to be the same as the electroweak coupling, i.e. $\lambda = \sqrt{4\pi\alpha}$, the existence of leptoquarks between 145 and 190 GeV, depending on the type of the leptoquark, can be excluded with a confidence level of 95%.[154,155]

6.5. Search for Additional Vector Bosons and Exited Quarks

Additional vector bosons arise naturally in the framework of many extensions of the minimal $SU(2)$ x $U(1)$ Standard Model of electroweak interactions, being it through right-handed currents,[156] composite models,[157] or various models derived from superstring theories.[158]

In the UA2 data, additional vector bosons have been searched for in their electronic decay modes as well as in their decay mode into quark pairs.

6.5.1. Electron Decay Modes

The cross section for the production of a vector boson times the branching ratio to electrons has been computed as a function of the boson mass, their couplings

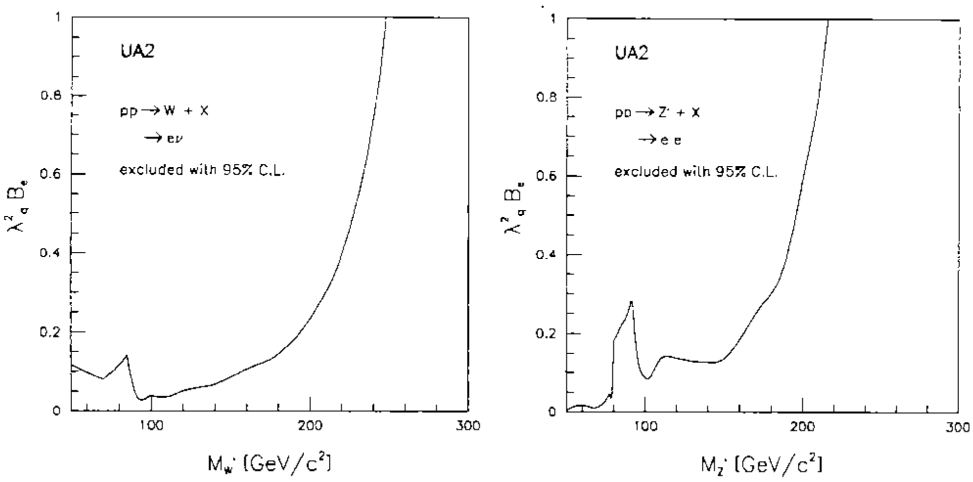

Figure 39. *(a) Limits for an additional charged vector boson W', shown as 95% confidence level contours in the $(M_{W'}, \lambda_q^2 B_e)$ plane (see text). (b) Same as (a) for an additional vector boson Z' decaying into electron pairs.*

to quarks, λ_q, and their branching ratio to electrons, B_e. The values for λ_q and B_e have been normalized to the Standard Model values, so that the cross section is obtained by multiplying the Standard Model value by the factor $\lambda_q^2 B_e$. It has been assumed that the total width of the new boson is given by the width of the standard vector bosons scaled by the mass ratio

$$\Gamma_{V'} = \Gamma_V \frac{m_{V'}}{m_V} \qquad (V = W, Z). \tag{33}$$

Limits for W' and Z' production have been extracted from a comparison of the observed electron neutrino transverse mass spectrum and the electron pair mass spectrum with spectra predicted in the case new vector bosons are present, by using maximum likelihood techniques.[159]

The results are shown in Fig. 39(a) and (b) for W' and Z' respectively, as 95% confidence level contours in the $(M_{V'}, \lambda_q^2 B_e)$-plane. In the regions of degenerate masses with the standard vector bosons the observed rates for the $W \to e\nu$ and $Z \to ee$, compared to the second order QCD prediction, have been used to extract the mass limits. Assuming standard model couplings, the following limits can be placed at the 95% confidence level:

$$\begin{aligned} m_{W'} &> 247\ GeV \qquad (95\%\ C.L.), \\ m_{Z'} &> 216\ GeV \qquad (95\%\ C.L.). \end{aligned}$$

Due to the higher centre of mass energy at the Fermilab Collider, even higher mass limits have been extracted by the CDF experiment.[160] From their data W' and Z'

bosons with masses below 520 GeV and 412 GeV, respectively, can be excluded with a confidence level of 95%.

6.5.2. *Quark Decay Modes*

In some of the proposed extensions of the Standard Model new right handed heavy vector bosons appear. If leptonic decays of a right handed W, W_R, are suppressed because of a heavy or non-existent right handed neutrino, the limits quoted above do not apply. In this case, hadronic decay modes are the only direct way for the experimental observation of the decays of a hypothetical right handed W. At the same time, this search is also sensitive to the existence of additional vector bosons Z' or excited quarks, provided they decay into jet pairs.

Based on data corresponding to an integrated luminosity of 10.9 pb^{-1}, the UA2 Collaboration has searched the invariant two-jet mass spectrum for decays $W_R \rightarrow q\bar{q}'$, $Z' \rightarrow q\bar{q}$ and $q^* \rightarrow qg$.[161] The same analysis method as presented in Sect. 4.5. has been applied to the high mass region of the two-jet spectrum. As for the leptonic decay modes, limits have been determined as a function of the vector boson masses, respectively excited quark masses, and as a function of the branching ratio to quark pairs (Fig. 40).

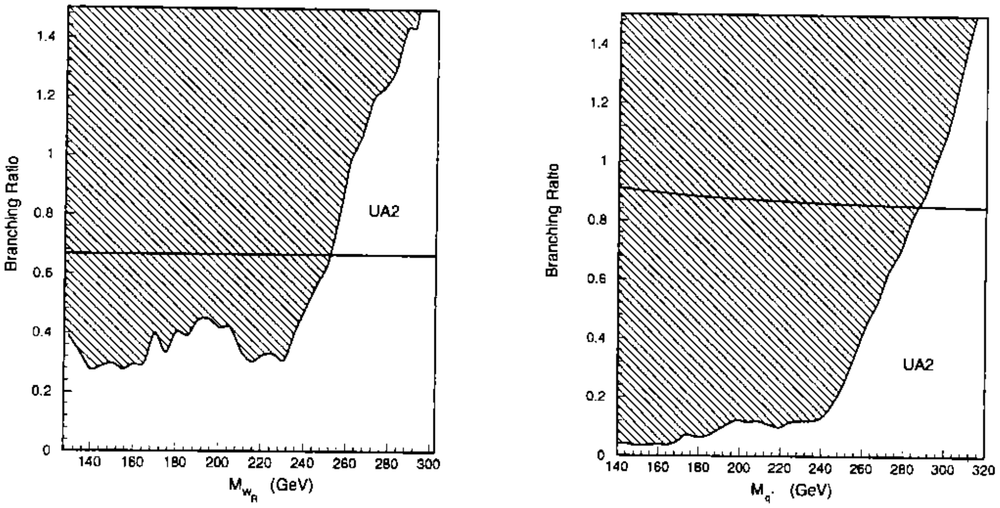

Figure 40. (a) Excluded regions (hatched) with 90% confidence level for right handed W's. The branching ratio is given as a fraction of the Standard Model branching ratio.
(b) Excluded regions (hatched) with 90% confidence level for excited quarks ($u^*, d^* \rightarrow qg$). The solid line shows the branching ratio for u^* and d^* decays to two jets.

Assuming standard couplings, the following mass limits have been obtained for heavy vector bosons at the 90% confidence level:[161]

$$m_{W_R} \quad > \quad 251 \ GeV \qquad\qquad (90\% \ C.L.),$$

$$m_{Z'} \quad > \quad 252 \ GeV \qquad\qquad (90\% \ C.L.).$$

In the case of excited quarks, a mixture of u^* and d^*-quarks has been assumed with decays according to the model described in Ref.[162]. Mass limits have been determined for three different cases depending on the relation between the u^* and d^* masses. With a confidence level of 90% the following limits have been obtained:[161]

$$\begin{array}{lll} m_{u^*} = m_{d^*} : & m_{q^*} > 288 \ GeV & (90\% \ C.L.), \\ m_{d^*} >> m_{u^*} : & m_{u^*} > 277 \ GeV & (90\% \ C.L.), \\ m_{u^*} >> m_{d^*} : & m_{d^*} > 247 \ GeV & (90\% \ C.L.). \end{array}$$

The reason for the lower mass limit for d^* compared to u^* quarks is that the fraction of up quarks in the proton is approximately twice that of down quarks and hence the d^* production cross section is smaller. It must also be noted that no K-factors have been included in the calculation of the cross sections, and hence the limits quoted can be considered as conservative.

7. Conclusions and Outlook

During the last decade, the CERN $p\bar{p}$ Collider and the associated experiments have proved to be remarkably successful at testing and enlarging our knowledge and understanding of the Standard Model of particle physics.

The data collected by the UA2 experiment in the second experimental phase from 1988 to 1990 allowed for detailed tests of many aspects of the Standard Model. Important electroweak parameters could be measured, which are complementary to the parameters measured with high precision at e^+e^- colliders. The most important ones being clearly the mass and the width of the W boson. Furthermore, it has been established that Quantum Chromodynamics is capable of predicting in a reliable way all measured production processes at hadron colliders, ranging from vector boson production to the production of multi-jet final states. In the search for new particles a new mass range, well above the reach of existing e^+e^- colliders, could be explored and the existence of many new particles with masses below ~100 GeV could be excluded.

Another important observation at the CERN Collider was that despite the complexity of hadronic collisions the hard scattering processes could be clearly identified and separated from the rest of the interaction. This feature, essential for the capability to discover new particles at hadron colliders, stimulated the construction of future machines with higher energies.

At present, the measurements of W properties and the continuation of the search for the not yet discovered top quark remain the principle goals of the existing experiments at the Fermilab Collider. It is expected that until 1998-1999 the experiments will collect data corresponding to an integrated luminosity of $\sim 100 \ pb^{-1}$. One can reasonably hope to achieve a W mass measurement to better than ~100 MeV and to discover the top quark if its mass is below ~ 200 GeV.

The goal for the long term future is to exploit further the large discovery potential of hadron colliders and to study hadron collisions at even higher energies. The only practical way to obtain such collisions at a useful rate is to build proton proton colliders with centre of mass energies above 10 TeV and very high luminosities, above 10^{33} cm^{-2} sec^{-1}, as planned for the Large Hadron Collider (LHC) at CERN. Most likely very exciting physics results will be obtained, ranging from the solution to the problem of electroweak symmetry breaking to the possible discovery of entirely new physics phenomena.

Acknowledgements

Finally, I would like to express my thanks and appreciation to all my colleagues from the UA2 experiment, who made it possible to obtain these results during many years of work. It was a pleasure to work together with them in the stimulating atmosphere of the UA2 Collaboration. Special thanks goes to L. DiLella, P. Jenni, G. Pollesello and E. Tsesmelis for carefully reading the manuscript. I am also indebted to A. Dell'Acqua, P. Lubrano and D. Wood for recovering some important figures from their archives.

References

1. UA1 Collaboration, G.Arnison et al., Phys. Lett. B122 (1983) 103;
   UA2 Collaboration, M.Banner et al., Phys. Lett. B122 (1983) 476;
   UA1 Collaboration, G.Arnison et al., Phys. Lett. B126 (1983) 398;
   UA2 Collaboration, M.Banner et al., Phys. Lett. B129 (1983) 130.
2. S.L.Glashow, Nucl. Phys. 22 (1961) 579;
   S. Weinberg, Phys. Rev. Lett. 19 (1967) 1264;
   A. Salam, Proc. 8th Nobel Symposium (1968) 367.
3. see for example:
   G.Altarelli, Phys. Rep. 81 (1982) 1;
   F.Yndurain, 'Quantum Chromodynamics', Springer-Verlag (1983).
4. UA2 Collaboration, M.Banner et al., Phys. Lett. B118 (1982) 203;
   UA1 Collaboration, G.Arnison et al., Phys. Lett. B123 (1983) 115.
5. see for example:
   J.Ellis, M.K.Gaillard, G.Girardi and P.Sorba, Ann. Rev. Nucl. Part. Sci. 32 (1982) 48;
   C.Quigg, Gauge Theories of Strong, Weak and Electroweak interactions, Benjamin/Cummings (1983);
   G.Altarelli and L.DiLella, Advanced Series on Directions in High Energy Physics, Vol.4 (1989) 1 (World Scientific);
   W.Hollik, Advanced Series on Directions in High Energy Physics, Vol.10 (1992) 1 (World Scientific).
6. N.Cabibbo, Phys. Rev. Lett. 10 (1963) 531;

M.Kobayashi and M.Maskawa, Progr. Theor. Phys. 49 (1973) 652.

7. P.Higgs, Phys. Lett. 12 (1964) 132; Phys. Rev. Lett. 13 (1964) 508; T.W.Kibble, Phys. Rev. 155 (1967) 1554.
8. E.Fermi, Nuovo Cimento 11 (1934) 1; Z. Phys. 88 (1934) 161.
9. Particle Data Group, Phys. Lett B239 (1990) 1.
10. A.Sirlin, Phys. Rev. D22 (1980) 971; W. Marciano and A.Sirlin, Phys. Rev. D22 (1980) 2695.
11. M.Veltman, Nucl. Phys. B123 (1977) 89; M.S.Chanowitz, M.A.Furman, I.Hinchliffe, Phys. Lett. B78 (1978) 225.
12. see for example: W.Hollik, Advanced Series on Directions in High Energy Physics, Vol.10 (1992) 1 (World Scientific).
13. W.J.Marciano, Phys. Rev. Lett. D20 (1979) 274; F.Antonelli et al. Phys. Lett. B91 (1980) 90; M.Veltman, Phys. Lett. B91 (1980) 95.
14. F. Jegerlehner, Z. Phys. C32 (1986) 425; Y.D.Bardin, S.Riemann and T.Riemann, Z. Phys. C32 (1986) 121; M.Consoli, S.LoPresti and L.Maiani, Nucl. Phys. B223 (1983) 474.
15. S.L.Glashow and E.Jenkins, Phys. Lett. B196 (1987) 233.
16. see for example: J.Ellis, M.K.Gaillard, G.Girardi and P.Sorba, Annu. Rev. Nucl. Part. Sci. 32 (1982) 48.
17. L.J.Reinders et al., Phys. Rep. 127 (1985) 1; T.Alvarez et al., Nucl. Phys. B301 (1988) 1.
18. D.W.Duke and R.G.Roberts, Phys. Rep. 120 (1985) 275, and references given therein.
19. B.L.Combridge, J.Kripfganz and J.Ranft, Phys. Lett. B70 (1977) 234.
20. R.K.Ellis and J.Sexton, Nucl. Phys. B269 (1986) 269.
21. F.Aversa et al., Phys. Lett. B210 (1988) 225; S.Ellis, Z.Kunszt and D.Soper, Phys. Rev. Lett. 62 (1989) 2188; Phys. Rev. Lett. 64 (1990) 2121.
22. S.D.Drell and T.M.Yan, Phys. Rev. Lett. 24 (1970) 181.
23. R.Hamberg, T.Matsuura and W.L.van Neerven, Nucl. Phys. B359 (1991) 343.
24. P.N.Harriman, A.D. Martin, R.G. Roberts, W.J.Stirling, Phys. Rev. D42 (1990); P.N.Harriman, A.D. Martin, R.G. Roberts, W.J.Stirling, Phys. Lett. B243 (1990) 421.
25. P.B.Arnold and M.H.Reno, Nucl. Phys. B319 (1989) 37.
26. R.J.Gonsalves, J.Palowski and C.F.Wai, Phys. Rev. D40 (1989) 2245.
27. R.K.Ellis and W.J.Stirling, CERN-report 91-01 (1991).
28. G.Altarelli et al., Nucl. Phys. B246 (1984) 12.
29. P.B.Arnold and R.P.Kaufmann, Nucl. Phys. B349 (1991) 381.
30. Y.Dokshitzer, D.L.Dyakonov and S.Troyan, Phys. Lett. B78 (1978) 290; G.Parisi and R.Petronzio, Nucl Phys. B154 (1979) 427; J.Kodaira and L.Trentadue, Phys. Lett. B112 (1982) 66.
31. L.Evans, E.Jones and H.Koziol, Advanced Series on Directions in High Energy Physics, Vol.4 (1989) 1 (World Scientific).
32. M.Banner et al., CERN/SPSC/78-8 (1978).
33. UA2 Collaboration, C.Booth, Proc. 6th Topical Workshop on Proton Antiproton Collider Physics, Aachen 1986.
34. A.Beer et al., Nucl. Instr. Meth. A224 (1984) 360.
35. R. Ansari et al., Nucl. Instr. Meth. A279 (1989) 388.
36. F.Bosi et al., Nucl. Instr. Meth. A283 (1989) 532.

37. R.Ansari et al., Nucl. Instr. Meth. A263 (1988) 51.
38. R.E.Ansorge et al., Nucl. Instr. Meth. A265 (1988) 33;
    J.Alitti et al., Nucl. Instr. Meth. A279 (1989) 364.
39. K.Borer et al., Nucl. Instr. Meth. A286 (1990) 128.
40. T.Koch, Aufbau und Test eines Flugzeitsystems, Thesis, Heidelberg University, HD-IHEP 89-05 (1989).
41. UA2 Collaboration, J. Alitti et al., Phys. Lett. B241 (1990) 151.
42. UA2 Collaboration, J. Alitti et al., Z. Phys. C47 (1990) 11.
43. UA2 Collaboration, Phys. Lett. B235 (1990) 363.
44. UA2 Collaboration, J. Alitti et al., Phys. Lett. B276 (1992) 365.
45. UA2 Collaboration, J. Alitti et al., Phys. Lett. B275 (1992) 202.
46. UA2 Collaboration, J. Alitti et al., Phys. Lett. B276 (1992) 354.
47. LEP Collaborations: ALEPH, DELPHI, L3 and OPAL, Phys. Lett. B276 (1992) 247.
48. CDF Collaboration, F. Abe et al., Phys. Rev. Lett. 65 (1990) 2243;
    CDF Collaboration, F. Abe et al., Phys. Rev. D43 (1991) 2070.
49. UA2 Collaboration, T.Åkesson et al., Z. Phys. C46 (1990) 179.
50. CDF Collaboration, F.Abe et al., Phys. Rev. Lett. 68 (1992) 447.
51. NMC Collaboration, D.Allasia et al., Phys. Lett. B249 (1990) 366.
52. UA1 Collaboration, C. Albajar et al., Phys. Lett. B253 (1991) 503.
53. CDF Collaboration, F. Abe et al., Phys. Rev. Lett, 64 (1990) 152.
54. H. Aihara, talk at the XIII. Int. Conf. on Physics in Collision, Heidelberg, June 1993; LBL-preprint 34572.
55. ALEPH Collaboration, D.Decamp et al., Phys. Lett. B236 (1990) 511;
    DELPHI Collaboration, P.Abreu et al., Phys. Lett. B242 (1990) 536;
    OPAL Collaboration, M.Z.Akrawy et al., Phys. Lett. B236 (1990) 364.
56. ALEPH Collaboration, D.Decamp et al., Phys. Lett. B235 (1990) 399;
    DELPHI Collaboration, P.Aarnio et al., Phys. Lett. B241 (1990) 425;
    L3 Collaboration, B.Adeva et al., Phys. Lett. B250 (1990) 183;
    OPAL Collaboration, M.Z.Akrawy et al., Phys. Lett. B240 (1990) 497.
57. UA2 Collaboration, J.Alitti et al., Z. Phys. C52 (1991) 209.
58. UA1 Collaboration, C.Albajar et al., Phys. Lett. B185 (1987) 233.
59. CDF Collaboration, F.Abe et al., Phys. Rev. Lett. 68 (1992) 3398.
60. UA2 Collaboration, J. Alitti et al., Z. Phys. C49 (1991) 17.
61. K.J.Gaemers and G.J.Gounaris, Z. Phys. C1 (1979) 259.
62. for a review see:
    B.Schrempp, Proc. XXIII. Int. Conf. on High Energy Physics, Berkeley, 1986.
63. J.Cortes, K.Hagiwara and F. Herzog, Nucl. Phys. B278 (1986) 26.
64. U.Baur and D. Zeppenfeld, Nucl. Phys. B308 (1988) 127.
65. U.Baur and D.Zeppenfeld, Nucl. Phys. B325 (1989) 253;
    K.Hagiwara, R.D.Peccei, D.Zeppenfeld and K.Hikasa, Nucl. Phys. B282 (1987) 253;
    D.Zeppenfeld, Phys. Lett. B183 (1987) 380.
66. UA2 Collaboration, J.Alitti et al., Phys. Lett. B 277 (1992) 194.
67. E.N.Argyres, O.Korakianitis, C.G.Papadopoulos and W.J.Stirling, Phys. Lett. B259 (1991) 195.
68. H.Grotch and R.W.Robinett, Phys. Rev. D35 (1987) 2153.
69. CDF Collaboration, T.Müller, talk at the Int. Europhysics Conf., Marseille, July 1993.
70. W. Bartel et al., Phys. Lett. B146 (1984) 437.
71. A. Bean et al., Phys. Rev. D35 (1987) 3533.
72. P. Nason, S.Dawson, R.K.Ellis, Nucl.Phys. B303 (1988) 607.
73. G.Altarelli et al., Nucl.Phys. B308 (1988) 724.
74. A.Ali, B.van Eijk, Proc. 5th Topical topkshop on Proton-Antiproton Collider Physics,

St.Vincent, (1985);
A.Ali et al., Nucl.Phys. B292 (1987) 1.
75. UA1 Collaboration, C.Albajar et al., Z. Phys. C48 (1990) 1.
76. CDF Collaboration, F.Abe et al., Phys. Rev. Lett. 64 (1990) 142.
77. CDF Collaboration, F.Abe et al., Phys. Rev. Lett. 64 (1990) 147.
78. CDF Collaboration, M.Cobal, FERMILAB-Conf-93/320-E;
CDF Collaboration, J.Benlloch, FERMILAB-Conf-93/329-E.
79. D0 Collaboration, M.Narain, talk at the XIII. Int. Conf. on Physics in Collision, Heidelberg, June 1993.
80. H.U.Bengtsson and T.Sjöstrand, PYTHIA, Comput. Phys. Comm. 46 (1987) 43.
81. T.Sjöstrand and M.Bengtsson, JETSET, Comput. Phys. Comm. 43 (1987) 367.
82. UA2 Collaboration, J.Alitti et al., Phys. Lett. B257 (1991) 232.
83. UA2 Collaboration, J.Appel et al., Phys. Lett. B160 (1985) 349.
84. E.Eichten et al., Phys. Rev. Lett. 62 (1984) 579;
erratum Rev.Mod.Phys. 58 (1986) 1065.
85. UA1 Collaboration, G. Arnison et al., Phys. Lett. B172 (1986) 461.
86. CDF Collaboration, F.Abe et al., Phys. Rev. Lett. 68 (1992) 1104.
87. K.Lane and M.Ramana, Phys. Rev. D44 (1991) 2678.
88. P.Frampton and S.Glashow, Phys. Lett. B190 (1987) 157.
89. H.Hufnagel, Analyse von Zwei- und Drei-Jet Ereignissen bei Proton-Antiproton Wechselwirkungen, Thesis, Dortmund University (1991).
90. J.Collins and D.Soper, Phys. Rev. D16 (1977) 2219.
91. L.DiLella, Ann. Rev. Nucl. Part. Sci. 35 (1985) 107.
92. UA1 Collaboration, G.Arnison et al., Phys. Lett. B158 (1985) 494;
G.Arnison et al., Phys. Lett. B177 (1986) 244.
93. CDF Collaboration, F. Abe et al., Phys. Rev. Lett. 69 (1992) 2896;
CDF Collaboration, F. Abe et al., Phys. Rev. Lett.D48 (1993) 998.
94. Z.Kunszt, W.J.Stirling, Phys. Lett. B171 (1986) 307.
95. F.Berends, W.Giele, H.Kuijf, Nucl. Phys. B333 (1990) 120; Phys. Lett. B232 (1990) 266.
96. UA2 Collaboration, J.Alitti et al., Phys. Lett. B268 (1991) 145.
97. D.W.Duke, J.F.Owens, Phys. Rev. D30 (1984) 49.
98. UA1 Collaboration, G.Arnison et al., Phys. Lett. B158 (1985) 494.
99. CDF Collaboration, F.Abe et al., Phys. Rev. D45 (1992) 1448.
100. N.Paver, D.Treleani, Nuovo Cimento 70A (1982) 215;
B.Humpert, Phys. Lett. B131 (1983) 461;
N.Paver, D. Treleani, Phys. Lett. B146 (1984) 252;
B.Humpert, R.Odorico, Phys. Lett. B154 (1985) 211.
101. T.Sjöstrand and M.Zijl, Phys. Rev. D36 (1987) 2019.
102. UA4 Collaboration, M.Bozzo et al., Phys. Lett. B147 (1984) 392.
103. AFS Collaboration, T.Åkesson et al., Z. Phys., C34 (1987) 163.
104. CDF Collaboration, F.Abe et al., Fermilab-Pub-93/003-E (1993).
105. P.Aurenche et al., Phys. Lett. B 140 (1984) 87;
P.Aurenche et al., Nucl. Phys. B 297 (1988) 661;
P.Aurenche et al., Phys. Rev. D 42 (1990)1440.
106. B.Bailey, J.Ohnemus, and J.F.Owens, FSUHEP-920320 and DTP/92/18.
107. UA2 Collaboration, J.Alitti et al., Phys. Lett. B288 (1992) 386.
108. R.Ford and W.Nelson, EGS Shower simulation program, SLAC-210 (1978).
109. P.Aurenche et al., Phys. Rev. D39 (1989) 3275.
110. CDF Collaboration, F.Abe et al., Phys. Rev. Lett. 68 (1992) 2734.
111. see for example:

ECFA Large Hadron Collider Workshop, Aachen (1990), CERN-90-10.
112. P.Aurenche et al., Z. Phys. C29 (1985) 459.
113. CDF Collaboration, F.Abe et al., Phys. Rev. Lett. 70 (1993) 2232.
114. UA1 Collaboration, C.Albajar et al., Z. Phys. C44 (1989) 15.
115. UA2 Collaboration, R. Ansari et al., Phys. Lett. B194 (1987) 158.
116. the following structure function parametrizations have been considered:
HMRSB (central value) and HMRSE (Ref.[24]), KMRSB0 (Ref.[117]), GRV (Ref.[118]), and MTE1, MTS1 and MTB1 (Ref.[119]).
117. J.Kwiecinski, A.D.Martin, R.G.Roberts, and W.J.Stirling, Phys. Rev. D42 (1990) 3645.
118. M.Glück, E.Reya, and A.Vogt, Z. Phys. C48 (1990) 471.
119. J.G.Morfin and W.K.Tung, Z. Phys. C52 (1991) 13.
120. S.D.Ellis, R.Kleiss, W.J.Stirling, Phys. Lett. B154 (1985) 435;
F.A.Berends et al., Phys.Lett. B224 (1989) 530.
121. UA2 Collaboration, J.Alitti et al., Phys. Lett. B263 (1991) 563.
122. R.G.Roberts and W.J.Stirling, private communication, (June 1990).
123. see for example:
S.Bethke and S.Catani, CERN-TH-6484-92; Proc. XXVII Rencontre de Moriond (1992);
G.Altarelli, CERN-TH-6623-92; Proc. QCD -20 Years later-, Aachen (1992).
124. UA1 Collaboration, A.Geiser, Proc. XXVII Rencontre de Moriond (1992).
125. see for example:
P.Fayet and S.Ferrara, Phys. Rep. 32 (1977) 249;
H.Haber and G.Kane, Phys. Rep. 117 (1985) 75.
126. S.Dawson, E.Eichten and C.Quigg, Phys. Rev. D31 (1985) 1581.
127. H.Baer et al., Phys. Lett. B161 (1985) 175;
Phys. Rev. Lett 63 (1989) 352.
128. UA1 Collaboration, C.Albajar et al., Phys. Lett. B198 (1987) 261.
129. CDF Collaboration, F.Abe et al., Phys. Rev. Lett. 62 (1989) 1825.
130. CDF Collaboration, F. Abe et al., Phys. Rev. Lett. 69 (1992) 3439.
131. DELPHI Collaboration, P.Abreu et al., Phys. Lett. B247 (1990) 148.
132. UA2 Collaboration, T.Åkesson et al., Phys. Lett. B238 (1990) 442.
133. ALEPH Collaboration, D.Decamp et al., Phys. Rep. 216 (1992) 253;
DELPHI Collaboration, P.Abreu et al., Phys. Lett. B247 (1990) 157;
L3 Collaboration, B.Adeva et al., Phys. Lett. B233 (1989) 530;
OPAL Collaboration, M.Akrawy et al., Phys. Lett. B240 (1990) 261;
OPAL Collaboration, M.Akrawy et al., Phys. Lett. B248 (1990) 211.
134. J.F.Gunion et al., The Higgs hunter guide, (Addison-Wesley, New York 1990).
135. M.Drees and D.P.Roy, CERN-TH 6080/91 (1991).
136. V.Barger and R.J.N.Phillips, Phys. Rev. D41 (1990) 884.
137. UA2 Collaboration, J.Alitti et al., Phys. Lett. B280 (1992) 137.
138. UA1 Collaboration, C.Albajar et al., Phys. Lett. B253 (1991) 503.
139. ALEPH Collaboration, D.Decamp et al., Phys. Lett. B241 (1990) 623;
DELPHI Collaboration, P.Abrew et al., Phys. Lett. B241 (1990) 449;
L3 Collaboration, B.Adeva et al.; Phys. Lett. B252 (1990) 511;
OPAL Collaboration, M.Z.Akrawy et al., Phys. Lett. B242 (1990) 299.
140. E.Eichten, K.D.Lane, and M.E.Peskin, Phys. Rev. Lett. 50 (1983) 811.
141. UA1 Collaboration, G.Arnison et al., Phys. Lett. B177 (1986) 244.
142. CDF Collaboration, F.Abe et al., Phys. Rev. Lett. 68 (1992) 1104.
143. CDF Collaboration, F.Abe et al., Phys. Rev. Lett. 69 (1992) 2896.
144. see for example:

J.C.Pati and A.Salam, Phys. Rev. D10 (1974) 275;
L.F.Abbott and E.Fahri, Phys. Lett. B101 (1981) 69;
M.Dine et al., Nucl. Phys. B259 (1985) 549.

145. W.Buchmueller and D.Wyler, Phys. Lett. B177 (1986) 377;
V.D.Angelopulos et al., Nucl. Phys. B292 (1987) 59.
146. J.L.Hewett and T.G. Rizzo, Phys. Rev. D36 (1987) 3367.
147. J.L.Hewett and S.Pakvasa, Phys. Rev. D37 (1988) 3165.
148. UA2 Collaboration, J.Alitti et al., Phys. Lett. B274 (1992) 507.
149. M.Montigny and L.Marleau, Phys. Rev. D40 (1989) 3616.
150. calculation based on formula of Ref.[147], structure functions of Ref.[84] with $\Lambda_{QCD} =$ 200 MeV and $\mu^2 = m_{LQ}^2 + P_T^2$.
151. ALEPH Collaboration, D.Decamp et al., Phys. Rep. 216 (1992) 253;
DELPHI Collaboration, P.Abreu et al., Phys. Lett. B275, (1992) 222;
L3 Collaboration, B.Adeva et al., Phys. Lett. B261, (1991) 169;
OPAL Collaboration, M.Akrawy et al., Phys. Lett. B263 (1991) 123.
152. CDF Collaboration, F.Abe et al., Fermilab-PUB-93/070-E, (1993).
153. D0 Collaboration, S.Abachi et al., Fermilab-PUB-93/340-E, (1993).
154. H1 Collaboration, I.Abt et al., Nucl. Phys. B396 (1993) 3.
155. ZEUS Collaboration, M.Derrick et al., Phys. Lett. B306 (1993) 173.
156. P.Langacker et al., Phys. Rev. D30 (1984) 1470.
157. U.Baur, MPI-PAE PTH 86-19; Proc. Prog. in Electroweak Interaction, Moriond (1986).
158. E. Cohen et al., Phys. Lett. B 165 (1985) 76;
F.del Aguila et al., Nucl. Phys. B287 (1987) 419;
D.London and J.L.Rosner, Phys. Rev. D34 (1986) 436.
159. S.Grünendahl, PhD. Thesis, Heidelberg University, HD-IHEP-91-04 (1991).
160. CDF Collaboration, F.Abe et al., Phys. Rev. Lett. 67 (1991) 2609;
CDF Collaboration, F.Abe et al., Phys. Rev. Lett. 68 (1992) 1463.
161. UA2 Collaboration, J.Alitti et al., Nucl. Phys. B400 (1993) 3.
162. U.Baur, M.Spira and P.M.Zerwas, Phys. Rev. D42 (1990) 815.

Contents

Druck: Dokumentationsstelle des Max-Planck-Instituts für extraterrestrische Physik, 85740 Garching